November 2015

Morphology Evolution Mechanisms of Low Band Gap Polymer-Based Photovoltaics

Sunzida Ferdous
University of Massachusetts Amherst

MORPHOLOGY EVOLUTION MECHANISMS OF LOW BAND GAP POLYMER-BASED PHOTOVOLTAICS

A Dissertation Presented

by

SUNZIDA FERDOUS

Submitted to the Graduate School of the
University of Massachusetts Amherst in partial fulfillment
of the requirements for the degree of

DOCTOR OF PHILOSOPHY

September 2015

Polymer Science and Engineering

MORPHOLOGY EVOLUTION MECHANISMS OF LOW BAND GAP POLYMER-BASED PHOTOVOLTAICS

A Dissertation Presented

by

SUNZIDA FERDOUS

Approved as to style and content by:

_____
Thomas P. Russell, Chair

_____
Kenneth Carter, Member

_____
Dhandapani Venkataraman, Member

_____
David A. Hoagland, Department Head
Polymer Science and Engineering

DEDICATION

To the loving memory of my wonderful Dad.
&
To the strongest and the most selfless woman I have ever known, my Mom.

ACKNOWLEDGMENTS

This dissertation could not have been completed without the encouragement and support that I have received from many individuals. First and foremost, my sincere gratitude goes to my advisor, Professor Thomas P. Russell. I have been privileged by the freedom he gave me while experimenting with various materials and techniques, as well as the opportunities he provided for being able to conduct experiments in the national labs and presenting my work at national conferences. His continued support, guidance, and insights over the past few years have been extremely vital that helped me to expand my knowledge and grow as a scientist. I am also indebted to the other members of my committee, Professor Kenneth Carter and Professor Dhandapani Venkataraman, for their valuable feedbacks and suggestions throughout all levels of my research.

This work would not have been possible without the generous support of U. S. Department of Energy through the Energy Frontier Research Center on Polymer-Based Materials for Harvesting Solar Energy, and National Science Foundation through the Materials Research Science and Engineering Center at the University of Massachusetts. I would like to thank my collaborators and co-authors: Feng Liu, Monojit Bag, Yao Liu, and Dong Wang for many thoughtful discussions, as well as assistance with different experiments. I further extend my gratitude to Eric Schaible, Alexander Hexemer, and Cheng Wang for their excellent support and assistance during many scattering measurements at the Advanced Light Source, Lawrence Berkeley National Laboratory.

All Russell group members, past and present, have made my grad school experience very enjoyable - I thank them all for their help, cooperation, and advice

throughout the past few years. I would also like to thank all PSE friends, especially, Packy (Sirinya), Yu, Weiyin, Hsin-wei, Gajin, Jooyoung, Caroline, and Jimmy who have made this journey a fun and memorable one for me. I am additionally grateful to the entire PSE faculty and staff members who have taught classes, offered various trainings, and helped me in many direct and indirect ways. My sincere appreciation goes to Volodimyr Duzhko for his numerous assistance with device characterization and his efforts to keep the photovoltaic facility up and running. My gratitude also extends to Sekar Thirunavukkarasu, Jacob Hirsch, Alexander Ribbe, Louis Raboin, John Nicholson, David Waldman, Weiguo Hu, Laurie Banas, Lisa Groth, Sandi Graves, Maria Farrington, Andre Mel'cuk, Jessica Skrocki, and Alyssa Kristek for many technical and administrative assistance that made my life at PSE much easier and enjoyable.

I thank all my friends from undergrad and high school who have been the source of countless laughter every time I have met or spoken to one of them. I also thank Tammy for being an amazing roommate throughout my entire grad school career. A very special thanks goes to Emon who has been by far my biggest cheerleader and has always been there for me through this entire process, both in the good times and the rough times.

Finally, I would like to thank all my family members (parents, brothers, cousins, sister-in-law, uncles, aunts, grandparents) for their constant support and encouragement throughout my life. I am especially grateful to my parents for their endless love and their continued belief in me, which have always pushed me to move forward in life.

ABSTRACT

MORPHOLOGY EVOLUTION MECHANISMS OF LOW BAND GAP POLYMER-BASED PHOTOVOLTAICS

SEPTEMBER 2015

SUNZIDA FERDOUS, B.S., WINONA STATE UNIVERSITY

M.S., UNIVERSITY OF MASSACHUSETTS AMHERST

Ph.D., UNIVERSITY OF MASSACHUSETTS AMHERST

Directed by: Professor Thomas P. Russell

An optimal nanoscale phase separation between the donor (generally, a conjugated polymer) and the acceptor (generally, a fullerene derivative) materials is one of the major requirements for obtaining high efficiency organic photovoltaic (OPV) device. Recent methods of controlling such nanostructure morphology in a bulkheterojunction (BHJ) OPV device involve addition of a small amount of solvent additive to the donor and acceptor solutions. The idea is to retain the acceptor materials into the solution for a longer period of time during the film solidification process, thus allowing the donor material to crystallize earlier. The ultimate morphology resulting from the solvent casting process of such multicomponent active layers involves a complex interplay of interactions between polymer/solvent, polymer/additive, fullerene/solvent, fullerene/additive, polymer/fullerene, and solvent/additive. In addition, multiple kinetic processes occur including solvent evaporation, phase separation, as well as polymer crystallization that lead to the final morphology of the active layer. Disentangling these different

contributions is the key for optimization of the active layer morphology, and has been a primary emphasis of this dissertation. Accordingly, the major focus of this dissertation is twofold: to understand the parameters and interactions of solvent additives that govern the morphology evolution process of different low band-gap polymer/fullerene systems, as well as developing a laboratory-scale slot-die coating methodology, which not only mimics the large area roll-to-roll device fabrication process, but also plays an integral part on investigating the morphology evolution process of the polymer/fullerene blends. Two different low band-gap polymers (PDPPBT and PTB7) are investigated. Detail descriptions of the mechanisms leading to the final morphology are also provided.

TABLE OF CONTENTS

Page

LIST OF TABLES

LIST OF FIGURES

Figure Page

CHAPTER 1

INTRODUCTION

1.1 Overview

The global interest of reducing CO_2 emissions and the foreseeable shortage of fossil fuels have been a great motivation for the widespread development of renewable energy sources, of which photovoltaic (PV) technology is a promising one. The use of organic molecules as light absorbing materials in PV cells dates as far back as 1959 reporting a photo-conversion efficiency of only $2 \times 10^{-6}\%$, while Bell Laboratories reported an efficiency of 6% from a silicon based inorganic cell in 1954.[1,2] Inorganic materials still dominate the PV market, however, their widespread usage is limited by the high material and manufacturing costs. Organic photovoltaic (OPV) technology, on the other hand, offers numerous advantages including ultra-lightweight and semi-transparent properties, mechanical flexibility, low-cost manufacturing, as well as short energy payback times. Furthermore, OPV is compatible with high volume, roll-to-toll printing methods due to the solution processability of organic semiconductors.[3–5] These attributes make it a promising candidate for use as an energy source in the next generation low-powered flexible electronic devices.

One of the first studies demonstrating a good understanding of the physics and chemistry behind polymer-based OPVs involved a bilayer structure between a soluble polymer, 2-methoxy-5-(2-ethylhexyloxy)-polyphenylenevinylene (MEHPPV) and the insoluble buckminsterfullerene (C_{60}) that gave an efficiency of only 0.04%.[6,7]

Subsequently, an interpenetrating structure between the MEHPPV and a soluble fullerene derivative was shown to significantly improve efficiency up to 2.5%.[8,9] Further advances in the field resulted in efficiency as high as 5% based on poly(3-hexylthiophene) (P3HT) and fullerene devices, which have served as a model system for elucidating various parameters that dictate the optimal photocurrent generation in an OPV device. Different processing conditions such as solvent annealing, thermal annealing, as well as incorporation of processing additives have been applied to control the bulk morphology of this system for enhanced efficiencies.[4,3] However, further improvement in efficiency of this system is limited by the intrinsic absorption of P3HT. Theoretical calculation using the standard AM1.5G solar spectrum, showed that a P3HT:PCBM layer can absorb only 27% of the available photons and 44.3% of the available power.[3] The need to obtain higher efficiency has recently led to the development of new donor-acceptor type polymers with lower band-gap and consequently, enhanced photon absorption. Tremendous amount of research efforts, both academic and industrial, has now led to the recent achievements of 10-12% efficient OPV devices.[10–12] To turn this into a viable technology, current research efforts are now focused on further improving the device efficiency by new materials design, morphology control, incorporation of electrode modification layers for long term stability, as well as large area roll-to-roll processability of all layers involved.

1.2 Device Architectures and Operating Principles

The active layer of an OPV device is generally consisted of a conjugated polymer as the donor material, and a fullerene derivative as the acceptor material. A typical device architecture includes a multilayer structure: indium tin oxide (ITO) coated with a hole transporting interfacial layer as the anode/ the active layer blend/ an electron transporting interfacial layer/ a cathode layer (typically Al or Ag). This is generally referred as the normal or standard geometry. An inverted geometry is achieved by switching the hole and electron transporting layers, thus changing the device polarity.[13] These are schematically shown in **Figure 1.1**, along with a tandem cell structure.

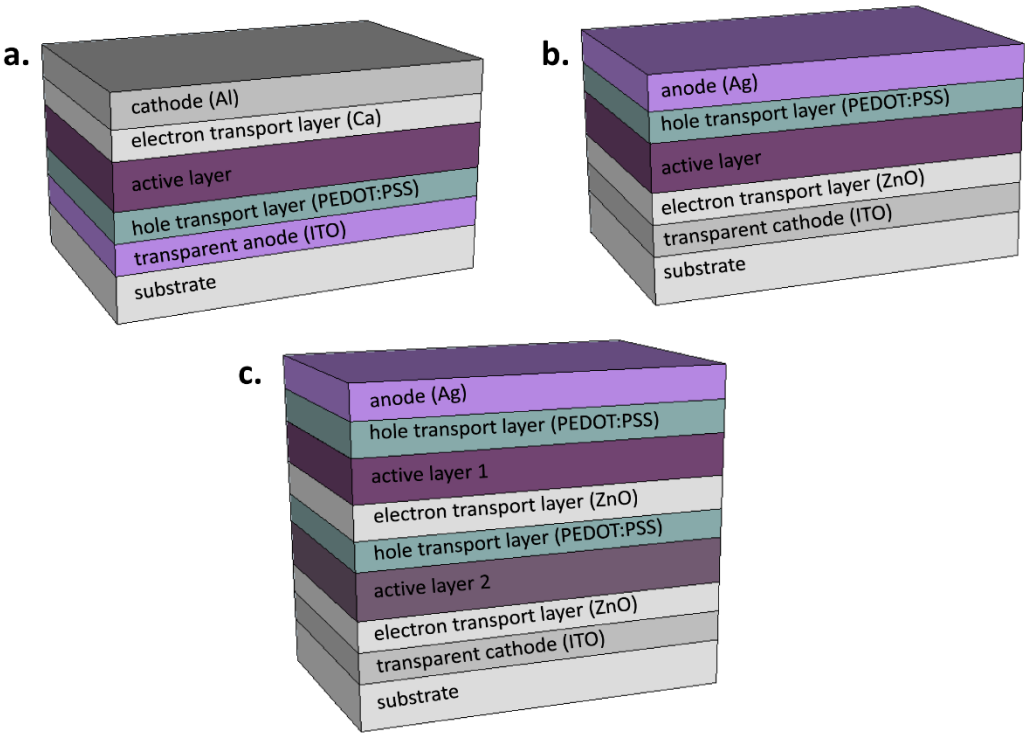

Figure 1.1 Schematics of typical OPV device architectures: a) normal geometry, b) inverted geometry, and c) tandem geometry.

Similar to inorganic semiconductors, photoabsorption in organic semiconductors also results in the formation of a bound electron-hole pair quasiparticle (generally referred as an exciton). However, the binding energy of this exciton is quite low for the inorganic semiconductors (few meV) such that the dissociation of excitons into free charge carriers can occur at room temperature. On the other hand, due to the large exciton binding energy in organic semiconductors (~0.4 eV or higher), the thermal energy at room temperature (25 meV) is not sufficient to dissociate the photo-generated excitons into free carriers.[14] This fundamental difference has generated an enormous research efforts in the OPV field to effectively dissociate the photogenerated excitions into free charge carriers. It was found that an OPV active layer structure require a formation of donor/acceptor heterojunctions with large interfacial areas that can provide an internal electrochemical driving force to effectively dissociate excitons into free carriers. Such heterojunctions with large donor/acceptor interfacial areas (**Figure 1.2**) are generally referred as the bulk hetero-junction (BHJ) structure[15], and has been proven to be the most successful active layer morphology.[4,13,16,17] Due to this internal electrochemical driving force at the BHJ interfaces, the photogenerated excitons at the donor phase can then dissociate into free charge carriers as a result of electron flow from the lowest unoccupied molecular orbital (LUMO) of the donor to the LUMO of the acceptor. The free charges subsequently transport to the respective electrodes by a drift built by internal electric fields, thus creating a photocurrent. These processes are schematically described in **Figure 1.2**. It should be also noted that, the exciton diffusion length, defined by the distance they can travel in the respective BHJ phase before

undergoing any recombination processes, is estimated to be approximately 10–20 nm. Therefore, a BHJ structure with phase separated length-scale that is commensurate with the exciton diffusion length is necessary for a high performance device.

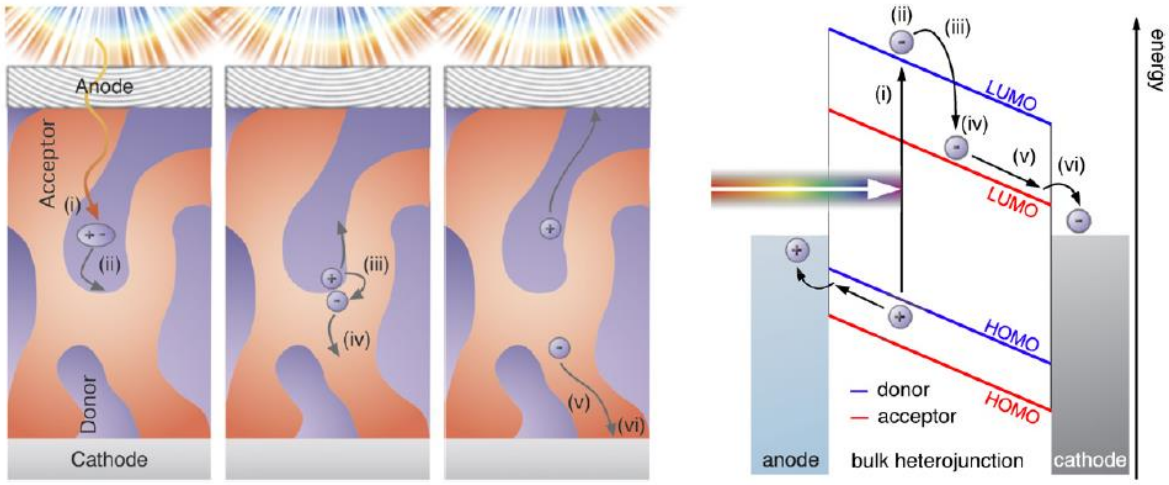

Figure 1.2 The steps to generate photocurrent after light absorption in a BHJ OPV is schematically demonstrated (left), with the corresponding simplified energy diagram (right).[5] (i) Exciton generation after photon absorption in the donor material. (ii) Exciton migration to the donor/acceptor interface. (iii) Exciton dissociation by electron transfer to the electronegative acceptor molecules. (iv) Separation of the still Coulomb-bound electron–hole pair due to electric field and material disorder. (v) Charge transport of electron and hole by hopping between localized states. (vi) Extraction of the charges leading to the photocurrent.

The figures of merits that describe the performance of an organic solar cell are: short circuit current density (J_{sc}), open circuit voltage (V_{oc}), fill factor (FF), and most importantly the power conversion efficiency (PCE). A typical current-voltage plot under dark and illumination is shown in **Figure 1.3**. When the OPV cell is measured in absence of light, it acts as a diode (dashed trace in **Figure 1.3**). The working regime of an OPV cell is in the bias range of 0 to V_{oc}, where power is generated. The maximum power (P_m) is generated at a certain point under the J-V curve. At this point (M_{pp}), the current density

and voltage are marked as J_m and V_m. The PCE is then given by the following expression where P_{in} is the incident power.

$$PCE = \frac{P_m}{P_{in}} = \frac{J_m \times V_m}{P_{in}} = \frac{J_{sc} \times V_{oc} \times FF}{P_{in}}$$

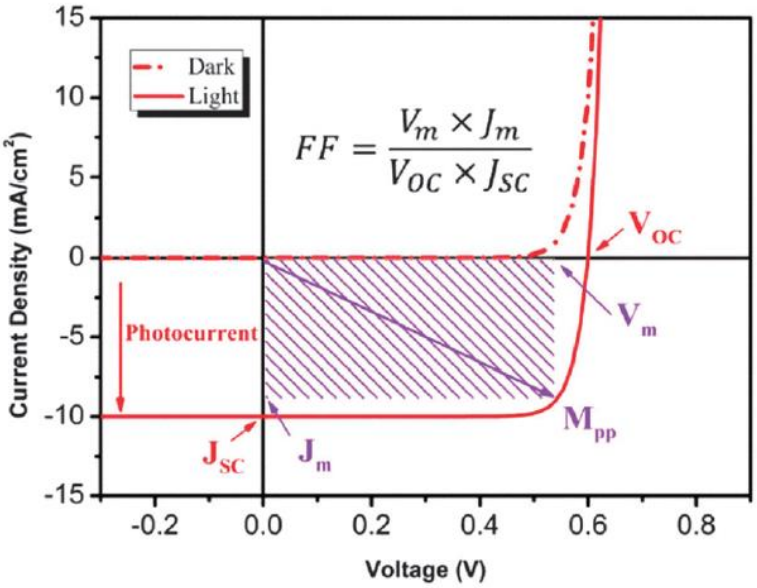

Figure 1.3 Current-voltage characteristics of a BHJ solar cells.[18]

1.3 Motivation

The large amount of research efforts on optimizing the optoelectronic properties of the absorbing materials (*i.e.* HOMO/LUMO energy levels), so as to maximize the photon absorption, does not always translate into the expected device performance. Recent use of extensive characterization studies to probe the structural features inside the BHJ thin films revealed that an increased crystallinity and optimized phase separation between the donor/acceptor moieties are the major morphological requirements for achieving high performance.[16,4,22] Therefore, it is of critical importance to be able to control the

molecular ordering, as well as the nanoscale morphology in order to fabricate a high efficiency device.

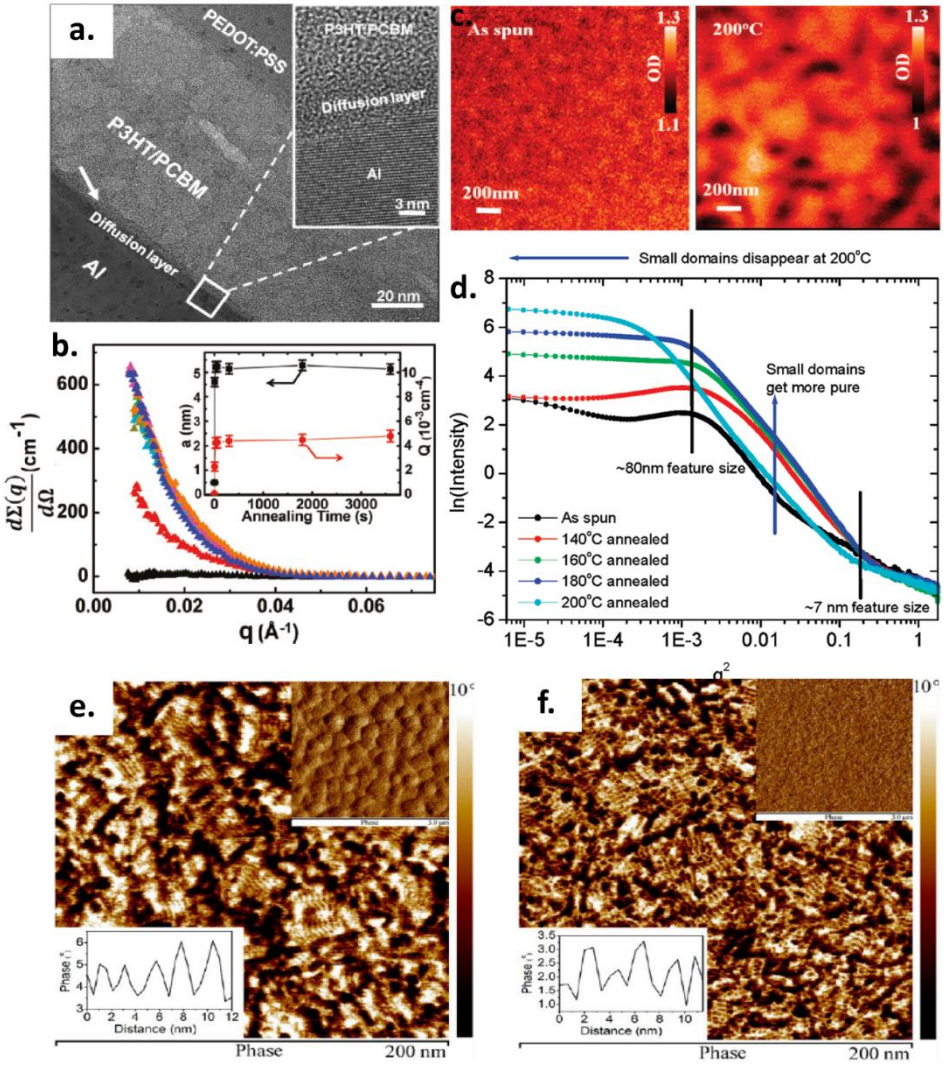

Figure 1.4 a) high resolution cross sectional TEM of annealed P3HT/PCBM device, b) small angle neutron scattering profiles showing the extent of phase separation from as spun (black triangle); preannealed 30 min (blue triangle); postannealed 5 s (red triangle); postannealed 30 s (green triangle); postannealed 1 min (brown triangle); postannealed 5 min (aqua triangle); postannealed 30 min (purple triangle); and postannealed 1 h (orange triangle) of P3HT/PCBM blend films. c) scanning transmission X-ray microscopy images of PFB/F8BT blends with d) corresponding scattering profiles. e, f) high resolution AFM images showing the presence of PTB7 face-on crystals along with differences in phase images (insets) for PTB7/PCBM blends processed without and with solvent additive.[19–21]

Molecular miscibility, intrinsic crystallinity, processing additives, rate of solvent removal, as well as other post processing conditions such as thermal or solvent annealing, and post deposition treatments such as BHJ surface treatment with polar solvent, insertion of polymer interlayers between the active layer and electrode - all have been shown to strongly influence the BHJ nanostructure in a wide range of length-scale.[23–25] A few examples demonstrating such morphological differences from the widely studied P3HT/PCBM, and PFB/F8BT system, as well as the recently developed PTB7/PCBM blend system are given in **Figure 1.4**.[19–21] However, post-processing techniques such as thermal annealing, which has been extremely beneficial for the archetypical P3HT/PCBM system, is quite detrimental for the recently developed many low band gap (LBG) polymer/fullerene blends.[26] Instead, optimized nanoscale morphology can be obtained from these systems by using a small amount (1-10%) of solvent additive, giving efficiency in the range of 7-10%. Additionally, the effect of the same additive on morphologies based on different donor/acceptor materials can be drastically different. For example, the addition of 1,8-diiodooctane or 1,8-octanedithiol into the P3HT/PCBM[27–29] or the PCPDTBT/PCBM[30,31] systems has shown to increase both polymer crystallinity and phase separation sizes, while in the PDPPTPT/PCBM[32] and PTB7/PCBM[33] systems, addition of 1,8-diiodooctane has shown to drastically reduce the phase separation size. These differences are attributed to the varied interactions of the solvent additives with the different active materials. However, morphology optimization process based on the solvent additive approach largely remains as a skill rather than being based on the mechanistic understanding of these additives on the morphology evolution processes. It

is, therefore, crucial to gain insight on the interactions of such solvent additives with the different polymer/fullerene systems.

1.4 Thesis Overview

The focus of this dissertation is twofold: to understand the parameters of solvent additives that govern the morphology evolution process of LBG polymer/fullerene systems, as well as developing a laboratory-scale slot-die coating methodologies, which not only mimics the large area roll-to-roll device fabrication process, but also played an integral part on investigating the morphology evolution process of the polymer/ fullerene blends. Results from this work can enable researchers to apply the parameters for further development of OPV materials and their fabrications.

Chapter 2 describes the effects of various solvent mixtures on the morphology of diketopyrrolopyrrole (DPP)-based low band gap polymer (PDPPBT) and phenyl-C71-butyric acid methyl ester ($PC_{71}BM$) blends. The quality of the solvent mixtures was varied systematically using a combination of a non-aromatic polar primary solvent with high boiling point solvent additive of increasing polarities. An unfavorable solvent-$PC_{71}BM$ interaction affects the growth process of polymer crystallites inside the blend. When non-aromatic polar solvent was used, large $PC_{71}BM$ aggregates were formed that increased in size with the addition of non-polar secondary solvents. When polar solvents were instead used as the secondary solvents, the size scales of the aggregates decrease markedly, creating a percolated fibrillar type network. Power conversion efficiencies ranging from 0.03% to 5% were obtained, depending on the solvent system used.

Chapter 3 describes the development of a mini slot-die coater, which will be used for all subsequent coating experiments, unless otherwise specified. Using the best solvent additive from Chapter 2, PDPPBT/$PC_{71}BM$ BHJ devices were fabricated using the slot-die coating method. The optimized solvent additive concentration was found to be different for the slot-die coated devices compared to the devices prepared by spin-coating method in Chapter 2. This also underscores the importance of using a technologically relevant coating method for prescreening and optimizing materials in a research lab set up. The slot-die was further integrated with synchrotron facility to monitor the morphology evolution process by *in-situ* grazing incidence wide and small angle x-ray scattering methods as a function of solvent additive concentrations in the PDPPBT/$PC_{71}BM$.

Chapter 4 utilizes the slot-die coating methodology to understand the role of solvent additive on controlling the morphology evolution process of PTB7, the current state of the art low band gap polymer, when blended with $PC_{71}BM$. Although, the solvent additive is a poor solvent for PTB7, the results indicate a presence of strong interaction between the additive and the PTB7 polymer chains, even at supersaturated conditions. Furthermore, PCE as high as 8% was achieved, which, to the best of our knowledge, is the highest reported PCE from a continuous coating technique method.

Chapter 5 summarizes the work of this dissertation, and provides preliminary experimental results on temperature dependent crystallization of PTB7/$PC_{71}BM$ active layer, as well as describes ways to overcome the challenges regarding continuous coating process of highly crystalline small molecule based OPV, thus opening possibilities for new routes to further enhance the device performance.

1.5 References

[1] H. Kallmann, M. Pope, *J. Chem. Phys.* **1959**, *30*, 585.

[2] D. M. Chapin, C. S. Fuller, G. L. Pearson, *J. Appl. Phys.* **1954**, *25*, 676.

[3] G. Dennler, M. C. Scharber, C. J. Brabec, *Adv. Mater.* **2009**, *21*, 1323.

[4] F. Liu, Y. Gu, X. Shen, S. Ferdous, H. W. Wang, T. P. Russell, *Prog. Polym. Sci.* **2013**, *38*, 1990.

[5] C. Deibel, V. Dyakonov, *Reports Prog. Phys.* **2010**, *73*, 096401.

[6] N. S. Sariciftci, L. Smilowitz, a J. Heeger, F. Wudl, *Science* **1992**, *258*, 1474.

[7] N. S. Sariciftci, D. Braun, C. Zhang, V. I. Srdanov, a. J. Heeger, G. Stucky, F. Wudl, *Appl. Phys. Lett.* **1993**, *62*, 585.

[8] J. C. Hummelen, B. W. Knight, F. Lepeq, F. Wudl, J. Yao, C. L. Wilkins, **1995**, 532.

[9] A. J. H. G. Yu, J. Gao, J. C. Hummelen, F. Wudl, *Science (80-.).* **1995**, *270*, 1789.

[10] Y. Liu, J. Zhao, Z. Li, C. Mu, W. Ma, H. Hu, K. Jiang, H. Lin, H. Ade, H. Yan, *Nat. Commun.* **2014**, *5*, 5293.

[11] Heliatek News, **2013**, www.heliatek.com/newscenter.

[12] Z. He, B. Xiao, F. Liu, H. Wu, Y. Yang, S. Xiao, C. Wang, T. P. Russell, Y. Cao, *Nat. Photonics* **2015**, *9*, DOI 10.1038/nphoton.2015.6.

[13] S. B. Darling, F. You, *RSC Adv.* **2013**, *3*, 17633.

[14] P. W. M. Blom, V. D. Mihailetchi, L. J. A. Koster, D. E. Markov, *Adv. Mater.* **2007**, *19*, 1551.

[15] G. Yu, J. Gao, J. C. Hummelen, F. Wudl, A. J. Heeger, *Science (80-.).* **1995**, *270*, 1789.

[16] Y. Huang, E. J. Kramer, A. J. Heeger, G. C. Bazan, *Chem. Rev.* **2014**, *114*, 7006.

[17] T. S. Gehan, M. Bag, L. a Renna, X. Shen, D. D. Algaier, P. M. Lahti, T. P. Russell, D. Venkataraman, *Nano Lett.* **2014**, *14*, 5238.

[18] B. Qi, J. Wang, *Phys. Chem. Chem. Phys.* **2013**, *15*, 8972.

[19] D. Chen, A. Nakahara, D. Wei, D. Nordlund, T. P. Russell, *Nano Lett.* **2011**, *11*, 561.

[20] S. Swaraj, C. Wang, H. Yan, B. Watts, J. Lüning, C. R. McNeill, H. Ade, *Nano Lett.* **2010**, *10*, 2863.

[21] D. Wang, F. Liu, N. Yagihashi, M. Nakaya, S. Ferdous, X. Liang, A. Muramatsu, K. Nakajima, T. P. Russell, *Nano Lett.* **2014**, *14*, 5727.

[22] N. D. Treat, M. L. Chabinyc, *Annu. Rev. Phys. Chem.* **2014**, *65*, 59.

[23] B. a Collins, J. R. Tumbleston, H. Ade, *J. Phys. Chem.Lett.* **2011**, *2*, 3135.

[24] W. Chen, M. P. Nikiforov, S. B. Darling, *Energy Environ. Sci.* **2012**, *5*, 8045.

[25] J. Rivnay, S. C. B. Mannsfeld, C. E. Miller, A. Salleo, M. F. Toney, *Chem. Rev.* **2012**, *112*, 5488.

[26] H. Chen, Y.-C. Hsiao, B. Hu, M. Dadmun, *Adv. Funct. Mater.* **2014**, *24*, 5129.

[27] H. Y. Chen, H. Yang, G. Yang, N. S. Sista, R. Zadoyan, G. Li, Y. Yang, *J. Phys. Chem. C* **2009**, *113*, 7946.

[28] T. Salim, L. H. Wong, B. Brauer, R. Kukreja, Y. L. Foo, Z. Bao, eng M. Lam, *J. Mater. Chem.* **2011**, *21*, 242.

[29] Y. Yao, J. Hou, Z. Xu, G. Li, Y. Yang, *Adv. Funct. Mater.* **2008**, *18*, 1783.

[30] J. Peet, J. Y. Kim, N. E. Coates, W. L. Ma, D. Moses, a J. Heeger, G. C. Bazan, *Nat. Mater.* **2007**, *6*, 497.

[31] J. K. Lee, W. L. Ma, C. J. Brabec, J. Yuen, J. S. Moon, J. Y. Kim, K. Lee, G. C. Bazan, A. J. Heeger, *J. Am. Chem. Soc.* **2008**, *130*, 3619.

[32] J. C. Bijleveld, V. S. Gevaerts, D. Di Nuzzo, M. Turbiez, S. C. J. Mathijssen, D. M. De Leeuw, M. M. Wienk, R. A. J. Janssen, *Adv. Mater.* **2010**, *22*, 242.

[33] Y. Liang, Z. Xu, J. Xia, S. T. Tsai, Y. Wu, G. Li, C. Ray, L. Yu, *Adv. Energy Mater.* **2010**, *22*, 135.

CHAPTER 2

IMPACT OF SOLVENT QUALITIES ON THE ACTIVE LAYER MORPHOLOGY OF DPP-BASED LOW BAND GAP POLYMER PHOTOVOLTAICS

2.1 Introduction

Solution processing of polymer semiconductors is one of the key advantages of organic photovoltaic (OPV) devices. Typically, in an OPV device, a donor polymer and an acceptor molecule form a bi-continuous network, with domains ~10-20 nm in size, for efficient charge separation and transport. Choice of casting solvents is a critical step towards better device performance.[1–4] To control the morphology during the film cast step, one needs to understand the effect of solvent as it evaporates and the final thin film morphology is formed. Once the films have dried, morphologies developed both in the in-plane and out-of-plane directions with respect to the sample surface play significant roles in device performance.[5,6] Recently, mixed solvent systems or additive-based systems have proven to be beneficial for obtaining high performance devices with optimal multi-length scale morphologies.[7–13] Optimum morphologies formed by these mixed solvent systems are attractive, since they can eliminate additional post processing steps, such as thermal annealing. In general, two criteria are followed when choosing an additive/secondary solvent: i) it should have relatively higher solubility toward the phenyl-C71-butyric acid methyl ester ($PC_{71}BM$) and should be a bad solvent for the polymers, and ii) the boiling point must be significantly higher than that of the primary solvent.[14] Thus the kinetics of phase separation and crystallization can be modulated.

In this chapter, we used a diketopyrrolopyrrole (DPP)-based low band gap polymer[9,15,16] (PDPPBT) and phenyl-C71-butyric acid methyl ester ($PC_{71}BM$) (**Figure 2.1a**) blends as a model system in a series of mixed solvents, consisting of a good solvent for both of the active material components, as well as secondary solvents that are poor solvents for the polymer while having varied interactions with $PC_{71}BM$. As a control experiment, devices were also fabricated using a single processing solvent, chloroform (CF), that is the primary good solvent for both of the active materials. The solvent additives: p-xylene (pXY), toluene (TLN), chlorobenzene (CB), anisole (Ani), and dichlorobenzene (DCB) were chosen based on their different polarities and vapor pressures. **Table 2.1** summarizes the different solvent properties.[17,18] In our experiments, 80% (v/v) good solvent and 20% (v/v) bad solvent were used in the mixed solvent systems. A significant enhancement in PCE was observed when the secondary solvents were relatively polar. In addition, as the polarity of these secondary solvent increases, PCEs also increase. Boiling points or vapor pressures of the secondary solvents also affect the final morphology. The morphologies of these blend films were investigated by real space imaging techniques such as transmission electron microscopy (TEM), scanning force microscopy (SFM), conductive atomic force microscopy (cAFM), as well as reciprocal space methods, such as grazing incidence wide angle x-ray diffraction (GIWAXD), grazing incidence small angle x-ray scattering (GISAXS), and resonance soft x-ray scattering (RSoXS). It was found that: i) Characteristic length scales describing the morphologies become more important in device performance than polymer crystallinity. The best device performance was obtained from the morphology containing the shortest

fibril-to-fibril distance. The performance decreased as this inter-fibrillar distance increased. ii) Unfavorable interactions between non-polar secondary solvents and $PC_{71}BM$, due to polarity mismatch, as well as relatively poor surface wettability, caused large scale phase separation with poor device performance.

Table 2.1 Solvent properties: boiling points, relative polarities and Hansen solubility parameters.

Solvent	b. p. (°C)	Relative Polarity[17]	Hansen Solubility Parameter[18]		
			δ_D $(MPa)^{1/2}$	δ_p $(MPa)^{1/2}$	δ_H $(MPa)^{1/2}$
CF	61	0.259	17.8	3.1	5.7
pXY	138	0.074	17.6	1.0	3.1
TLN	111	0.099	18.0	1.4	2.0
CB	131	0.188	19.0	4.3	2.0
Ani	154	0.198	17.8	4.1	6.7
DCB	181	0.225	19.2	6.3	3.3

2.2 Experimental

2.2.1 Materials and Methods

PDPPBT was synthesized in our lab by Dr. Feng Liu and $PC_{71}BM$ was purchased from American Dye Source. All the solvents were purchased from Sigma-Aldrich and used without further purifications. Blend solutions were prepared from a 1:1 weight ratio of PDPPBT:$PC_{71}BM$ with total concentration of 1.2% (w/v) and stirred overnight at 55 ℃ for complete dissolution. Indium tin oxide (ITO) coated glass substrates (15 mm x 15 mm) were purchased from Thin Film Devices Inc. The thickness and the resistivity of the ITO was 145 ± 10 nm and 20 ± 2 ohms/sq, respectively. Poly(3,4-ethylenedioxythiophene): polystyrene sulphonate (PEDOT: PSS) was purchased from CLEVIOS™.

2.2.2 Device Preparation and Characterization

All devices were fabricated in a conventional geometry with the structure: ITO/PEDOT:PSS/BHJ/LiF/Al. Active layer solution was spin coated at 1700 rpm for 60 s on ~35 nm PEDOT:PSS-coated pre-cleaned ITO substrates, giving a thickness of ~120-130 nm in CF/CB, CF/Ani, and CF/DCB processed films. 1.5 nm LiF and 100 nm Al were thermally deposited as cathode creating an active area of 0.06 cm^2. Solar cells were characterized under simulated 100 mW/cm^2 AM1.5G. Device fabrication and measurements were performed inside a nitrogen filled glove box. Photo mask was used during measurements.

2.2.3 Morphology and Structure Characterizations

Active layer morphology characterizations using scattering methods such as grazing incidence wide angle x-ray diffraction (GIWAXD), grazing incidence small angle x-ray scattering (GISAXS), and resonant soft x-ray scattering (RSoXS) were performed in Advanced Light Source, Lawrence Berkeley National Lab at beamlines 7.3.3 (GIWAXD and GISAXS) and 11.0.1.2 (RSoXS). For static GIWAXD and GISAXS measurements, blend films were prepared by spin coating solution on PEDOT:PSS covered Si wafers. For *in-situ* GIWAXD measurements, blend solutions (50 µL) were drop-cast onto clean UV-O_3 treated (1 h) Si wafer. Bright-field transmission electron microscopy (TEM) experiments were performed with a JEOL 2000 FX TEM operating at an accelerating voltage of 200 kV. Atomic force microscopy (AFM) was conducted using a Digital Instruments Dimension 3100 AFM, operating in tapping mode. Conductive AFM (cAFM) was performed with an Asylum Research MFP-3D AFM in contact mode. Si tips with Pt conductive coating (force

constant 0.2 N/m and resonant frequency 13 kHz) were purchased from Budget Sensors for cAFM measurements.

2.3 Results and Discussions

2.3.1 Device Characteristics

Current density-voltage (J-V) characteristics for the PDPPBT:$PC_{71}BM$ based BHJ devices are shown in **Figure 2.1b** and device parameters are summarized in **Table 2.2**. We find that the use of only non-aromatic but polar solvent, chloroform (CF), gives low efficiency (0.56%) devices. Device efficiencies were even lower when aromatic non-polar solvents were mixed with CF. On the other hand, when aromatic solvents that are relatively polar were added to CF, device performances were improved. The best PCE was obtained when DCB (5.0% PCE) was used as the secondary solvent that was the most polar (**Table 2.1**) solvent with the lowest vapor pressure, followed by Ani (4.9%), CB (4%), TLN (0.05%) and pXY (0.03%). Device performance was enhanced mainly due to higher short-circuit current density (J_{sc}) values. J_{sc} values were increased as the polarity and the boiling points of the secondary solvents increased. These devices were characterized to correlate their morphologies with the device performances. The significantly lower fill factors (FF) of the devices processed from the non-polar secondary solvents are attributed to poor morphologies obtained from these conditions.

Table 2.2 Device performance of PDPPBT:$PC_{71}BM$ based solar cells from different solvent systems. Average values of the device parameters with their standard deviations are shown.

	V_{oc} (V)	J_{sc} (mA/cm^2)	FF (%)	PCE (%)
CF	0.61 ± 0.01	1.50 ± 0.01	61.5 ± 4.6	0.56 ± 0.06
CF/pXY	0.61 ± 0.01	0.24 ± 0.02	24.1 ± 0.9	0.03 ± 0.004
CF/TLN	0.58 ± 0.04	0.34 ± 0.06	25.0 ± 1.0	0.05 ± 0.01
CF/CB	0.63 ± 0.004	11.5 ± 0.12	55.9 ± 1.2	4.0 ± 0.11
CF/Ani	0.60 ± 0.02	14.3 ± 0.15	57.7 ± 1.9	4.9 ± 0.1
CF/DCB	0.61 ± 0.02	15.5 ± 0.7	52.1 ± 1.4	5.0 ± 0.1

2.3.2 Impact of Polymer Crystallinity on Device Performance

Ultraviolet-visible (UV-Vis) absorbance spectra (**Figure 2.1c**) were measured for each of the blend thin films with different processing solvents. Two main peaks were observed at ~790 nm and ~720 nm. Peaks observed around 350 nm are due to $PC_{71}BM$. All the spectra were normalized at the highest absorption peak at ~790 nm. CF/TLN and CF/pXY processing conditions gave slightly blue shifted peaks in comparison to the other solvent systems. It is clear from the intensity of the 720 nm vibronic peak that addition of the secondary solvents increased the polymer crystallinity in the thin films. Among the polar secondary solvents, the intensity of the vibronic peak at ~720 nm is slightly higher for films processed from CF/DCB system than CF/Ani and CF/CB systems. Surprisingly, the 720 nm peak intensity is largest when the secondary solvents were non-polar (pXY and TLN) even though device performances were the lowest from films processed from these solvents. This may be due to the larger crystallite sizes observed in these systems from GIWAXD and *in-situ* GIWAXD measurements as discussed in the subsequent sections.

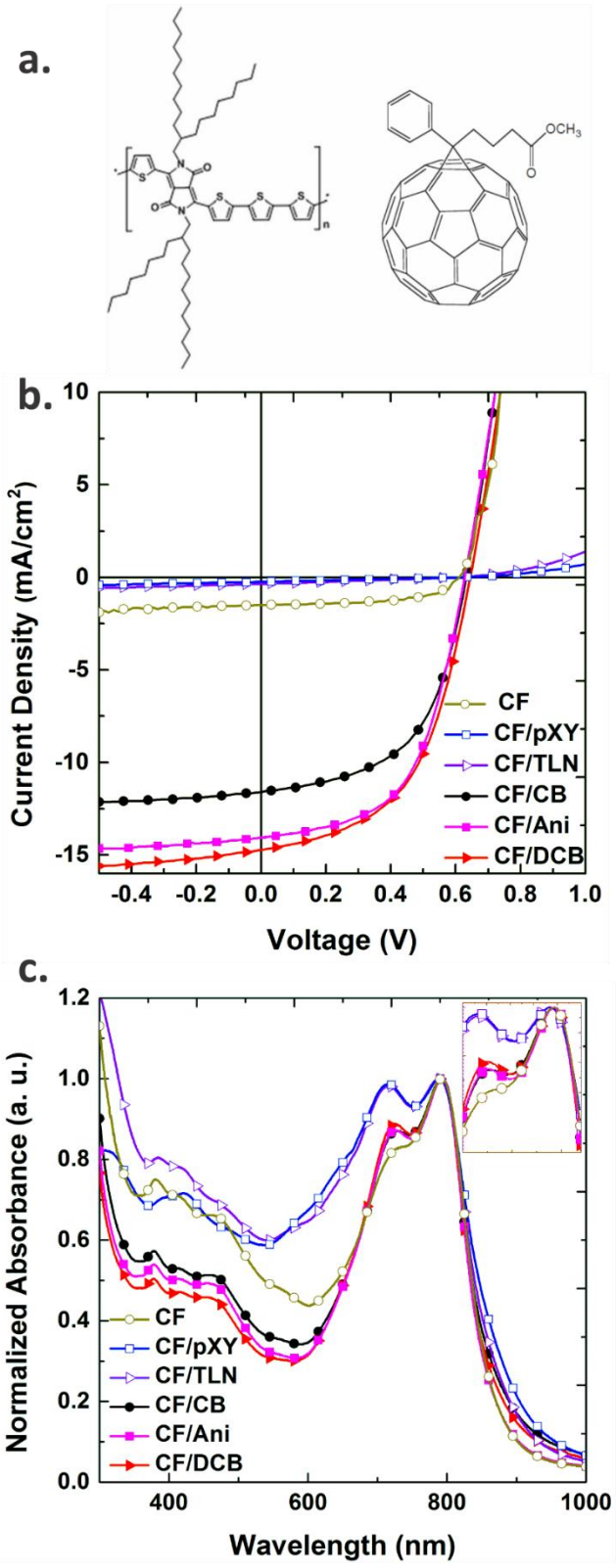

Figure 2.1 a) Chemical structures of PDPPBT (left) and $PC_{71}BM$ (right), b) Current density-voltage plots for the BHJ devices, and c) UV-Vis absorption spectra of PDPPBT: $PC_{71}BM$

blended thin films processed from different solvent systems. A magnified area is shown on the inset for vibronic peaks at 700-820 nm range.

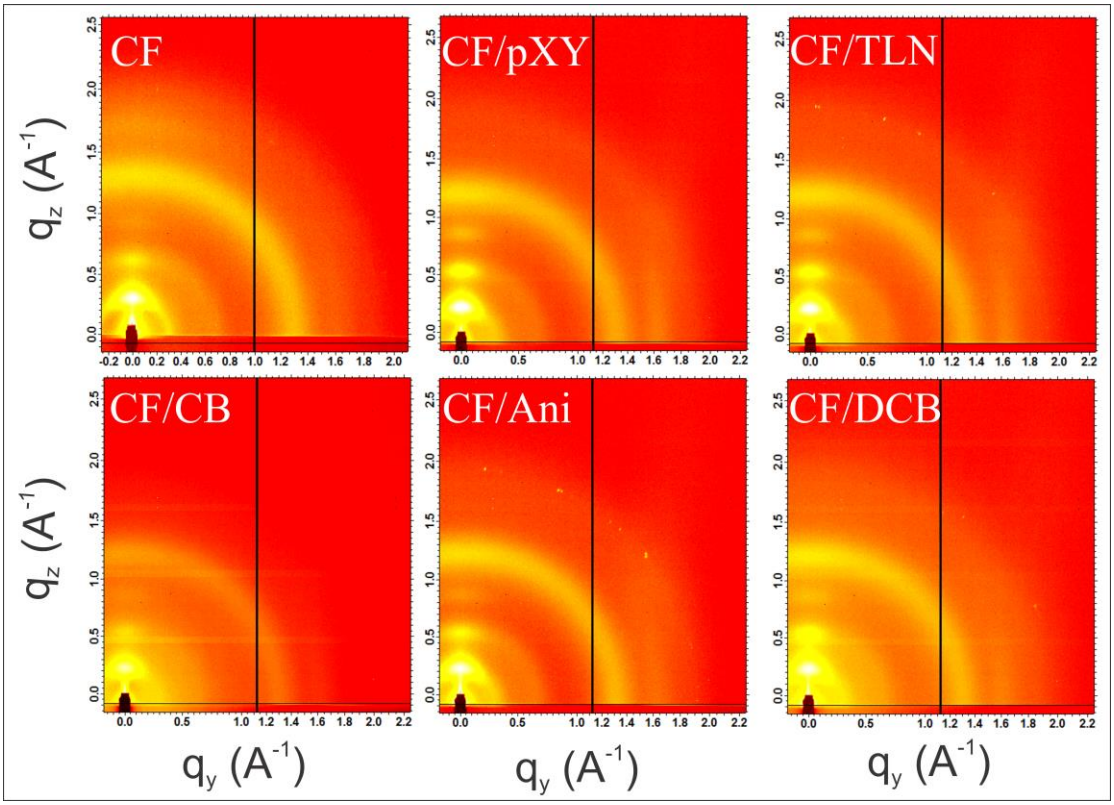

Figure 2.2 2D GIWAXD patterns obtained from blend films processed with CF, CF/pXY, CF/TLN, CF/CB, CF/Ani, and CF/DCB solvent systems.

GIWAXD measurements on the blend films show that the polymer chains orient in an edge-on manner. The 2D scattering patterns and the out of plane (OOP) 1D line profiles are shown in **Figure 2.2** and **Figure 2.3**, respectively. OOP (100) diffraction peaks were observed at ~0.3 $Å^{-1}$, corresponding to the separation distance between the main chain, separated by the alkyl side chains. OOP (100) peak areas were significantly larger when non-polar secondary solvents (pXY and TLN) were used as shown in **Table 2.3**. This indicates that degree of polymer chain ordering or crystallinity is highest for the CF/pXY

and CF/TLN systems, followed by films processed from polar secondary solvents. This correlates well with the UV-Vis data. Furthermore, when the blend film was processed from CF only, some face-on structure was present as evidenced by the broad peak at ~1.6 $Å^{-1}$ in **Figure 2.3** and the corresponding 2D pattern **Figure 2.2**. However, this processing condition did not give high device performance. On the other hand, no face-on structure was observed for any of the mixed solvent systems. **Table 2.3** summarizes the peak position (q_{100}), d-spacing (d_{100}), crystallite size (D_{100}), and peak area values for the OOP (100) peaks. $d_{100\ and}$ D_{100} values were calculated from the $d = \frac{2\pi}{q}$ relationship and the Scherrer equation ($D = \frac{2\pi}{FWHM}$), respectively.[19] d_{100}-spacing values were quite similar for all cases. However, crystallite sizes (D_{100}) were the largest (Table 2.3), yet device performances were the poorest, when non-polar secondary solvents were used (pXY and TLN). It is important to note that these large crystallite sizes (~18 nm) obtained from CF/pXY and CF/TLN systems are still within the range of exciton diffusion length of ~10s of nm. This indicates that crystallinity is not limiting the device efficiencies in these systems, rather the phase separation is more critical as observed in the later sections. The reason for larger crystallites in pXY and TLN systems is qualitatively explained in later sections of this chapter. The broad peak at ~ 1.3 $Å^{-1}$ arises from $PC_{71}BM$. An in-plane (IP) peak at ~1.6 $Å^{-1}$ corresponds to the inter-chain π-π stacking (**Figure 2.2**). Besides crystallinity, there are other factors involved, since both CF/CB and CF/DCB have very similar d_{100} and D_{100} values, yet, their device performances are significantly different (4% and 5% PCE). Given that a certain amount of polymer ordering/crystallinity exists, the

characteristic length scales describing the morphologies become more important in device performance than crystallinity, as will be discussed in the next section.

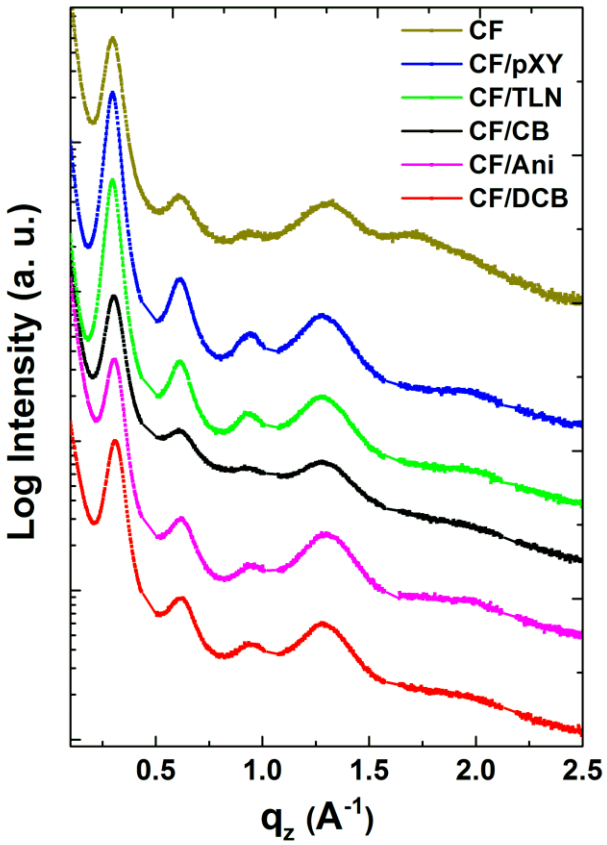

Figure 2.3 Out of plane 1D GIWAXD line profiles obtained from blend films processed with CF, CF/pXY, CF/TLN, CF/CB, CF/Ani, and CF/DCB solvent systems.

Table 2.3 Summary of peak positions (q), d-spacing (d) and crystallite sizes (D) for the out of plane (100) peaks.

	q_{100}($Å^{-1}$)	d_{100} (nm)	D_{100} (nm)	(100) Peak Area
CF	0.299	2.10	15.2	584
CF/pXY	0.298	2.11	18.3	1108
CF/TLN	0.297	2.11	18.2	912
CF/CB	0.305	2.06	14.8	545
CF/Ani	0.307	2.05	16.2	580
CF/DCB	0.311	2.02	15.1	665

2.3.3 Impact of Bulk and Surface Morphology on Device Performance

The use of the different secondary solvents in addition to the primary good solvent (CF) changed the bulk morphologies of these thin films. Grazing incidence small angle x-ray scattering (GISAXS) was used to investigate the in-plane electron density correlation[19–21] in the blend films for evaluating the bulk phase separation. Approximate estimates of the domain sizes (d) were obtained to be ~44, ~36, and ~32 nm for CF/CB, CF/Ani, and CF/DCB processed films, respectively, using the q positions of diffuse shoulders ($q = \frac{2\pi}{d}$) in the GISAXS profiles (**Figure 2.4a** and **Table 2.4**). We note that the larger scale domains in the CF, CF/pXY, and CF/TLN processed films are not seen in the GISAXS profiles due to q-range limitation. Resonant soft x-ray scattering (RSoXS) method offers better contrast between the active layer materials at x-ray energies near the absorption edge,[22–24] and was used to obtain a better spatial resolution with a smaller q-range. Here, soft x-ray energy, 284.2 eV at the carbon K-edge was used to generate the scattering contrast between the constituent moieties of PDPPBT polymer and the $PC_{71}BM$ in transmission mode. Scattering profiles are shown in **Figure 2.4b**. Scattering profiles are observed to be similar for CF/CB, CF/Ani, and CF/DCB films in RSoXS and GISAXS. A relatively sharp peak was observed at around q = 0.002 $Å^{-1}$, corresponding to a domain spacing of ~300 nm for the CF processed film. This spacing correlates well with the TEM image in **Figure 2.4d** for CF processed film, and is obviously disadvantageous for charge transport, even though polymer crystallinity is reasonable, as seen from UV-Vis and GIWAXD data. Even larger aggregation was observed when non-polar secondary solvents were used, with the biggest size-scale observed when the secondary solvent was the least

polar (pXY) (**Figure 2.4d**). This length scale was out of range to observe any scattering peaks in RSoXS. Interestingly, fibrillar structures from the polymer were observed in the uniform areas where no aggregates were present, as shown in the insets of CF/pXY and CF/TLN images. This indicates that the polymer ordering still exists, as also verified by GIWAXD measurements in **Figure 2.3**, regardless of the presence of large aggregates.

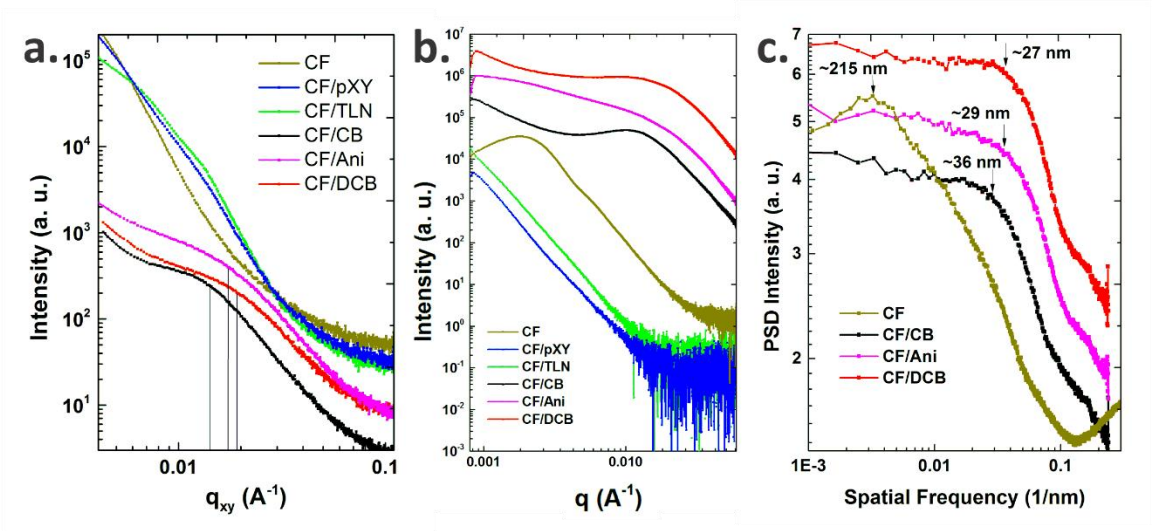

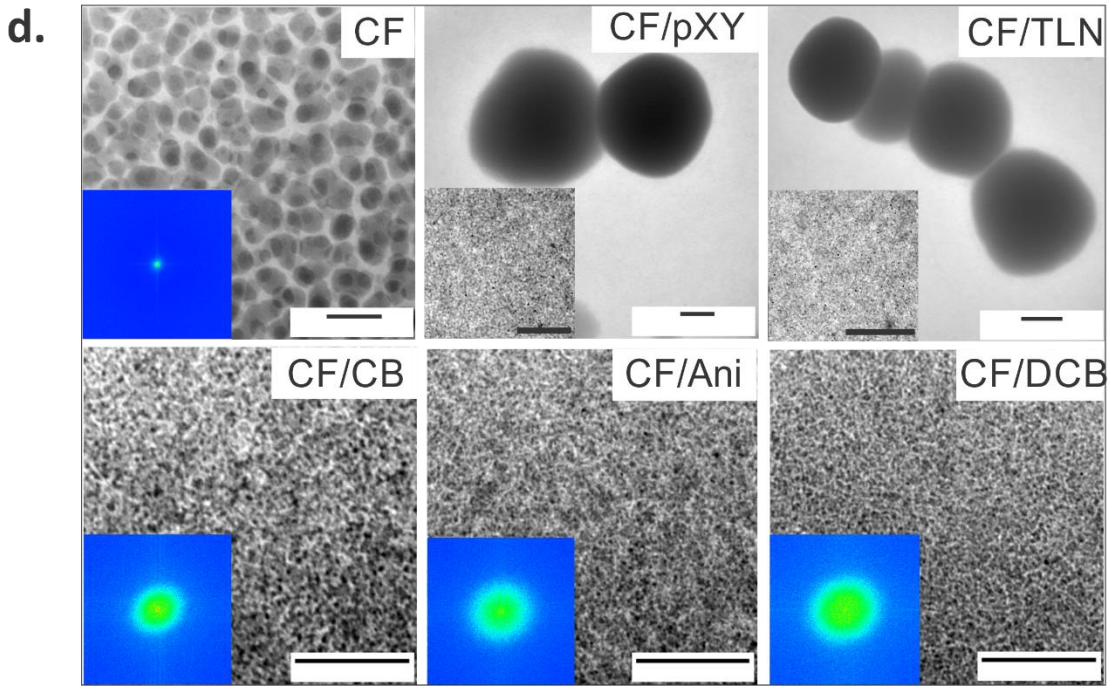

Figure 2.4 a) GISAXS 1D line profiles. Vertical lines indicate the positions where q-values were analyzed for CF/CB, CF/Ani, and CF/DCB processed films. b) Circularly averaged RSoXS profiles. c) Power Spectral Density (PSD) profiles for CF, CF/CB, CF/Ani, and CF/DCB. d) Bright field TEM images. Magnified areas on the non-aggregated regions are shown in the insets of CF/pXY and CF/TLN showing the presence of fibrillar type structures in these regions. All scale bars are 500 nm. Fourier Transforms of the images for CF, CF/CB, CF/Ani, and CF/DCB solvent systems are shown in respective insets.

Blend films processed from CF/CB, CF/Ani and CF/DCB solvent systems, on the other hand, show fibrillar structures everywhere with a much finer overall morphology (**Figure 2.4d**). Fourier transforms of these images are shown in the insets, along with their power spectral density (PSD) profiles in **Figure 2.4c**. The domain sizes obtained from the PSD profiles for CF/CB, CF/Ani, and CF/DCB systems are ~36, ~29, and ~27 nm, respectively, which are attributed to the fibril-to-fibril distances in these films. These agree exceptionally well with the spacings obtained from GISAXS and RSoXS measurements (**Table 2.4**) for the respective films. Consequently, the smaller fibril-to-fibril distances in CF/Ani and CF/DCB appear to be the origin for higher J_{sc} values, leading to the enhanced device performance. This resulted in a ~27% increase in J_{sc} in CF/DCB film compared to CF/CB film, giving a 25% increase in PCE. J_{sc} and PCE values are plotted as a function of fibril-to-fibril distances (**Figure 2.5**) obtained from the PSD analysis of TEM images. A clear correlation between feature size and OPV performance is observed. Smaller fibril-to-fibril distance would mean that there are more fibrillar structures formed. This may be due to the fact that processing with lower vapor pressure secondary solvents requires longer drying time, resulting in the formation of a larger population of nuclei in the films.

Table 2.4 Summary of domain spacings (d) obtained from GISAXS, RSoXS, and PSD analysis.

	From GISAXS		From RSoXS		From PSD
	q ($Å^{-1}$)	d (nm)	q ($Å^{-1}$)	d (nm)	d(nm)
CF	-	-	0.002	~300	~215
CF/CB	~0.0142	~44	0.0135	~46	~36
CF/Ani	~0.0173	~36	0.0189	~33	~29
CF/DCB	~0.0194	~32	0.0210	~31	~27

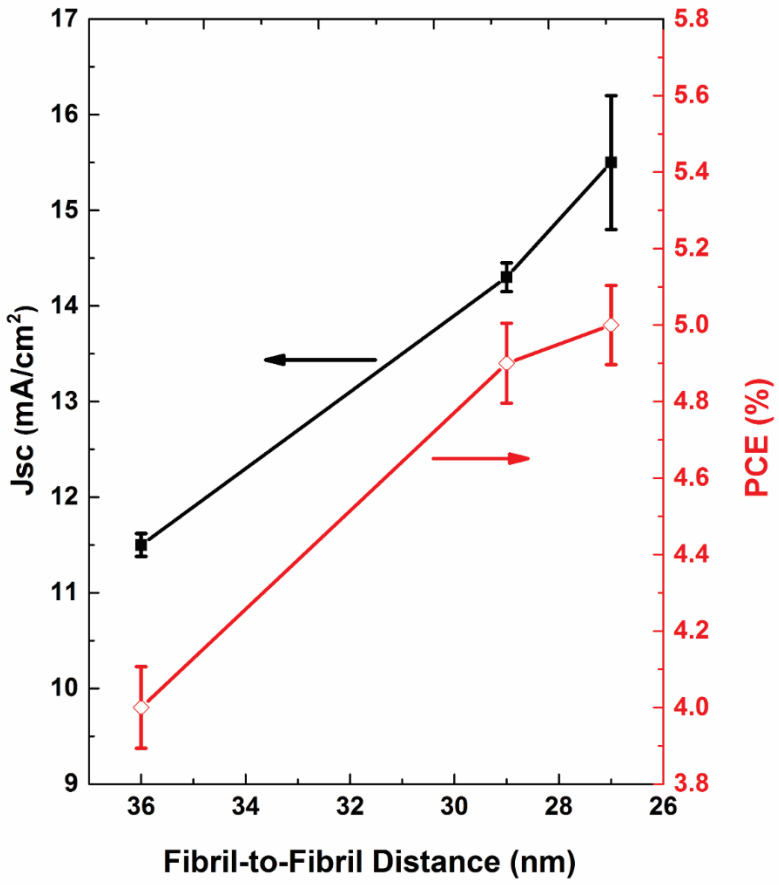

Figure 2.5 Device performance as a function of fibril-to-fibril distances (~36 nm for CF/CB, ~29 nm for CF/Ani, and ~27 nm for CF/DCB solvent systems) obtained from PSD analysis of TEM images.

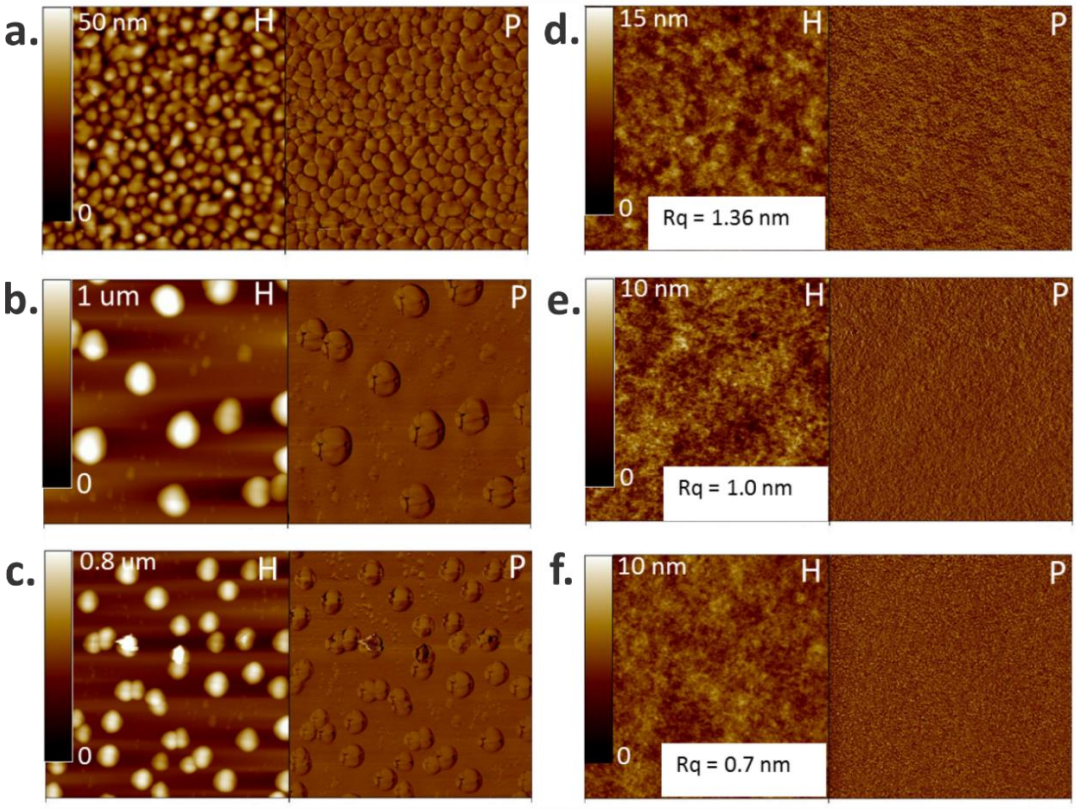

Figure 2.6 Surface topography of blend films by AFM. a) CF, b) CF/pXY, c) CF/TLN, d) CF/CB, e) CF/Ani, and f) CF/DCB processed blend films. H and P stand for height and phase images respectively. RMS roughness values are shown in the insets for the later three samples. Image sizes are 5 µm x 5 µm for a), d), e), f), and 20 µm x 20 µm for b), c), respectively.

Atomic force microscopy (AFM) was used to investigate the surface topography of the blend films (**Figure 2.6**). CF, CF/pXY, and CF/TLN surfaces were shown to have large aggregates as expected from the TEM images. These systems showed three-dimensional dewetting-type structures. Two length-scales of the dewetted structures were observed in the AFM images of CF/pXY and CF/TLN. These large scale aggregates are the source of poor device performance, regardless of sufficient polymer crystallinity. The reasons for these aggregates formation are discussed in the next section. The CF/CB, CF/Ani, and

CF/DCB systems, on the other hand, show more homogeneous fibrillar-type structures with CF/DCB having the least surface roughness followed by CF/Ani and CF/CB.

Conductive AFM (cAFM) was used to monitor the nanoscale charge transport in these blend films under dark condition. A platinum coated cAFM tip was used as the top electrode and PEDOT:PSS-coated ITO served as the bottom electrode to record current images. **Figure 2.7** shows the cAFM current images with different applied biases for CF, CF/CB, CF/Ani and CF/DCB processed BHJ films. Applying a positive bias generates positive current, corresponding to hole transport through the blend morphology. In **Figure 2.7a**, clear, bright and dark regions are observed when a positive bias was applied. This indicates that the bright regions correspond to polymer rich phases, showing the hole transport and dark regions correspond to the $PC_{71}BM$ aggregations. For CF/CB, CF/Ani, and CF/DCB processed films, on the other hand, percolated pathways for hole transport were observed on a much finer length scale, as expected. Hole transport increases with increased applied bias. Hole transport is also higher for CF/Ani and CF/DCB systems, compared to CF/CB system. This agrees well with smaller fibril-to-fibril distances in CF/Ani and CF/DCB systems as observed in the TEM images, which significantly facilitate hole transport through the blend morphology, resulting in enhanced J_{sc} toward a better device performance.

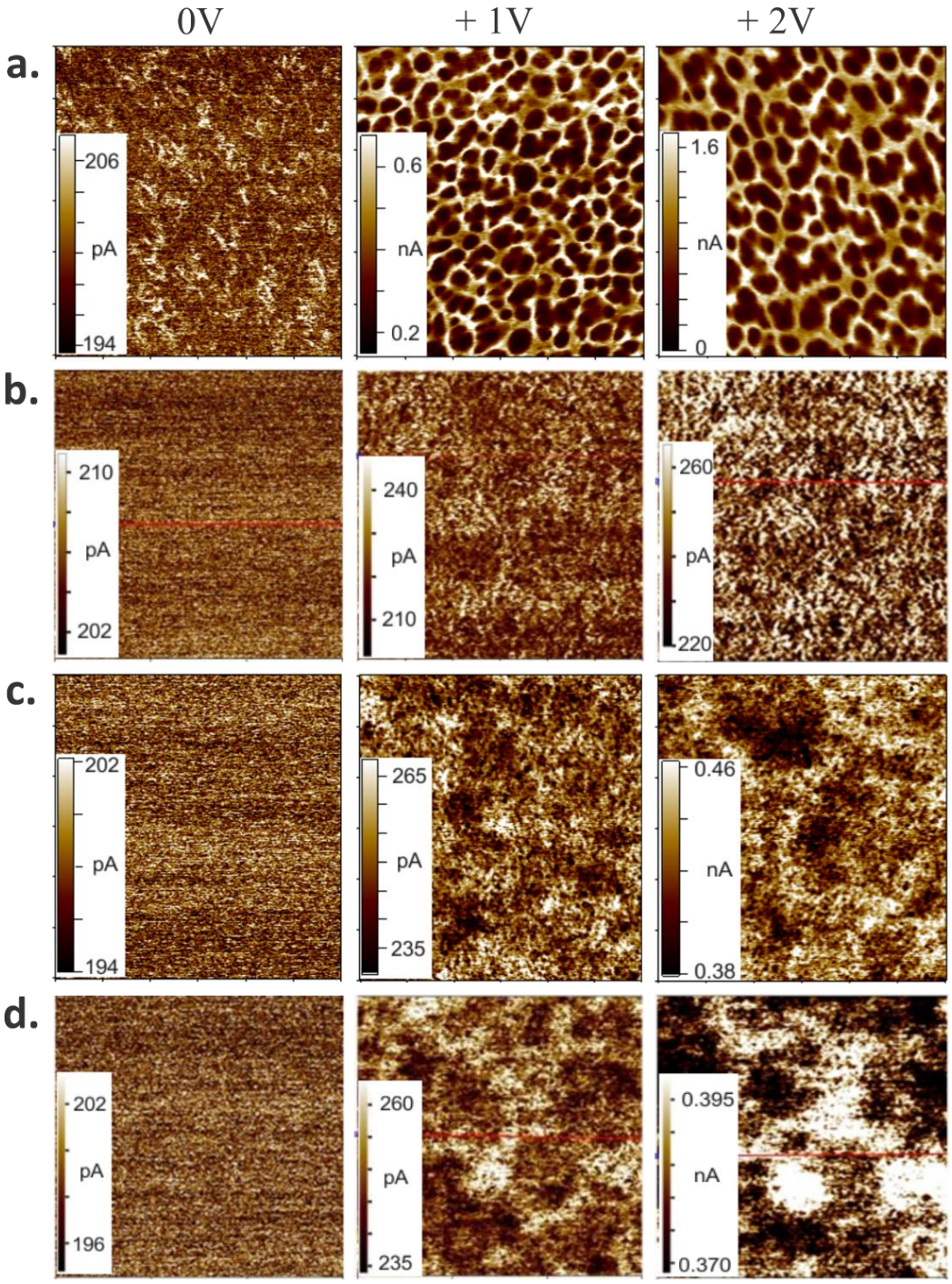

Figure 2.7 c-AFM current images at different applied biases for a) CF, b) CF/CB, c) CF/Ani, and d) CF/DCB processed blend films. All images are 3 x 3 µm in size.

2.3.4 Solubility and Wettability Effects on Morphology

Since PDPPBT crystallinity has been observed from both single and mixed solvent systems, including polar and non-polar secondary solvents (**Figure 2.3**), here we discuss only the effect of $PC_{71}BM$ interaction with these solvents. When pure PDPPBT were spin-coated from solvent systems consisting of non-polar secondary solvents (CF/pXY and CF/TLN), no large aggregates were observed from the PDPPBT film. However, dewetted large aggregates were seen when film was cast from solutions containing only $PC_{71}BM$ (**Figure 2.8**). Interestingly, when pure $PC_{71}BM$ was spin-coated from only CF, no aggregation was observed (AFM image not shown). A series of optical microscopy images was obtained from a drop cast solution of $PC_{71}BM$ on PEDOT:PSS surface to monitor the formation of aggregates as solvent (CF/pXY) evaporates (**Figure 2.9**). It can be seen that smaller aggregates are formed first in the presence of solvent. As solvent evaporates and eventually dewets the surface, smaller aggregates move closer to the neighboring aggregates, creating the large agglomerates. This drying process should be essentially similar for the case of spin coated films, where the sizes of these agglomerates would be reduced due to quick removal of solvents. Consequently, this indicates that the aggregates observed in the PDPPBT:$PC_{71}BM$ blend films in **Figure 2.6a, 2.6b, 2.6c** are mainly composed of $PC_{71}BM$. The coalescence of aggregates is also visible in the AFM images, especially in the phase images.

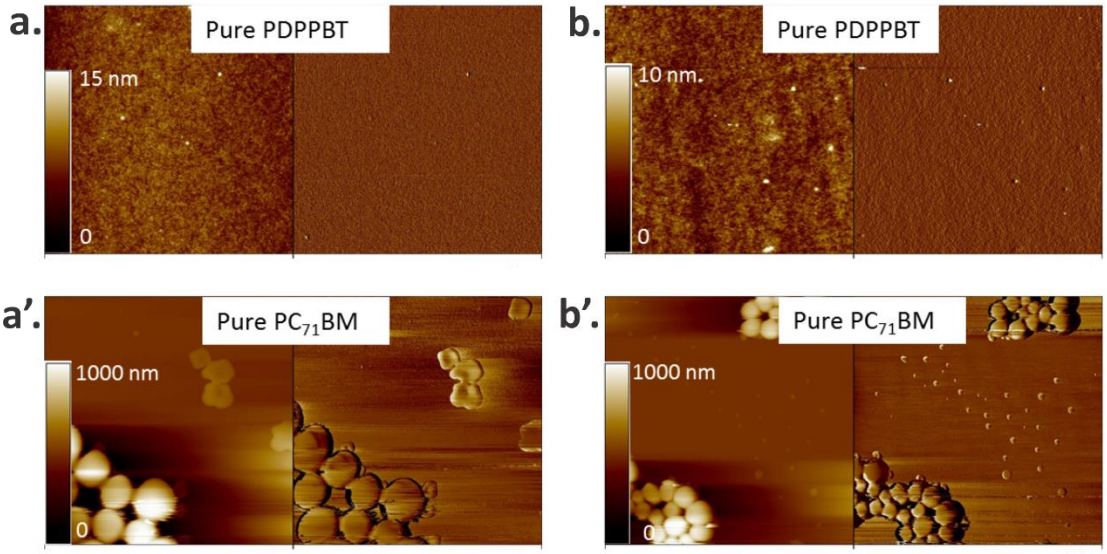

Figure 2.8 AFM of pure $PC_{71}BM$ and pure PDPPBT spin-coated films. a) only PDPPBT and a') only $PC_{71}BM$ from CF/pXY solvent system. b) only PDPPBT and b') only $PC_{71}BM$ from CF/TLN system. Height image is on the left and phase image is on the right. All images are 20 µm x 20 µm.

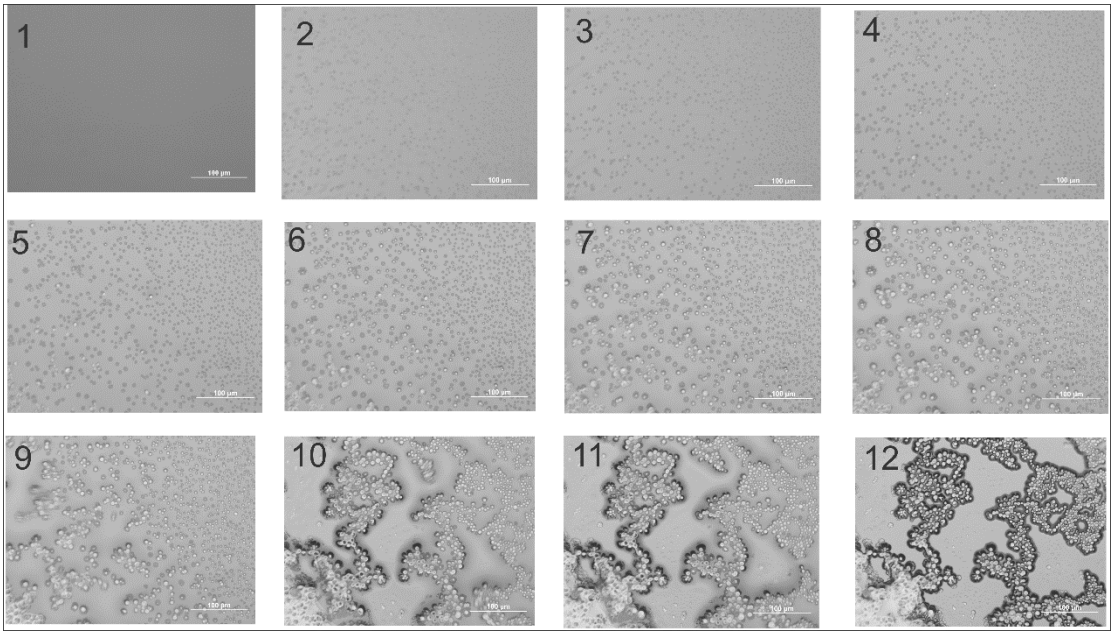

Figure 2.9 Selected micrographs from a series of optical microscope images of drop-cast $PC_{71}BM$ solution from CF/pXY onto PEDOT:PSS coated ITO substrate. Image 1 is right after drop casting the solution onto the substrate and image 12 is when most solvent is evaporated. All scale bars are 100 µm.

We believe that the reason behind this is the unfavorable interaction of $PC_{71}BM$ with the non-polar secondary solvents, as well as the interaction of blend solutions with the substrate surface. $PC_{71}BM$ interaction with different solvents can be explained by comparing the Hansen solubility parameters (HSP) of the solvents. HSPs are expansion of the Hildebrand solubility parameter that is defined as the square root of the total cohesion energy divided by the molar volume ($\delta_T = \sqrt{E/V}$) of the material. Later, this single term solubility parameter (δ_T) was separated into three terms by Hansen: dispersion cohesion parameter (δ_D), polar cohesion parameter (δ_P) and hydrogen bonding cohesion parameter (δ_H).[18] Although solubility parameters may not provide all the contributions from different intermolecular forces, it provides a useful measure of solvation quality for a wide range of organic materials.[18,25] The degree of similarity in HSPs between two solvents will indicate their degree of miscibility. Likewise, the similarity of HSPs between a solvent and a solute will indicate the degree to which the material will be soluble in that solvent. Recently, solubility parameters of processing solvents, small molecule additives, and active material components have been used to investigate their effects on BHJ morphology.[26–28] HSP values are listed in **Table 2.1** for the solvents used in our study. δ_D, δ_P, and δ_H for $PC_{71}BM$ are recently reported to be approximately 20.2, 5.4, and 4.5 $MPa^{1/2}$, respectively.[26] It is clear that HSPs for $PC_{71}BM$ are more similar to CF, CB, Ani, and DCB, than to pXY and TLN, particularly in terms of the polar component (δ_P). This suggests that $PC_{71}BM$ will have unfavorable interactions with the non-polar solvents, leading to a higher thermodynamic driving force for phase separation, as observed in the AFM and TEM images. As mentioned earlier, no aggregates were

observed from pure $PC_{71}BM$ film when processed with only CF, even though 200-300 nm sized aggregates were seen when it was blended with PDPPBT and processed from CF. Such large-scale aggregates are generally thought to occur due to the intrinsic immiscibility between the polymer and the $PC_{71}BM$. Similar structures have also been previously observed for other BHJ systems with different processing solvents.[3,8,29] δ_P of $PC_{71}BM$ is relatively closer to CF than pXY and TLN. Besides the immiscibility issue, one of the reasons for this smaller scale aggregation from CF processed PDPPBT:$PC_{71}BM$ blend film could be due to the interaction between the hydrophilic anode surface (PEDOT:PSS) and the blend solutions of various polarities. Hence, contact angle (CA) measurements, also related to surface energy, were performed with the PDPPBT:$PC_{71}BM$ blend solutions from each solvent system on the PEDOT:PSS surface. The results are summarized in **Table 2.5**. Addition of the aromatic non-polar solvents with CF, increased CA, while addition of the aromatic polar solvents with CF decreased CA. A larger contact angle indicates poorer wettability of the substrate surface, indicating that the blend solution is more hydrophobic than the hydrophilic PEDOT:PSS surface. The results indicate that PDPPBT:$PC_{71}BM$ blend solutions processed with CF/CB, CF/Ani, and CF/DCB have good wettability on PEDOT:PSS, in comparison with the blend solutions processed from CF/pXY and CF/TLN. Blend solution with CF has an intermediate wettability.

Thus, comparability of HSPs, together with wettability of the blend solutions, can provide a clue as to why the PDPPBT:$PC_{71}BM$ blend films show dramatic differences in morphologies, ranging from micron scale aggregates to nanometer scale homogeneously phase separated morphology.

Table 2.5 Contact angle measurements of PDPPBT:$PC_{71}BM$ blend solutions.

Solvent	CF	CF/pXY	CF/TLN	CF/CB	CF/Ani	CF/DCB
Contact Angle (°)	17	20	21	15	11	11

2.3.5 Morphology Evolution During Solvent Evaporation Process

The drying process is a critical step in forming the optimized morphology. This has been shown in many other systems, including both mixed solvent systems and low vapor pressure additive-based system. To investigate the effect of different solvents on polymer ordering during the drying process, *in-situ* GIWAXD measurements were performed to track the evolution of the OOP (100) peak corresponding to the polymer side chain ordering in the blend. Particularly, CF/pXY and CF/CB systems were investigated, since both of these secondary solvents have similar vapor pressures (pXY slightly lower than CB), but significantly different polarities (**Table 2.1**). A small amount of blend solution was drop cast onto PEDOT:PSS coated Si substrates. We note that, from the time of casting the blend solution to the beginning of data collection, ~60 s was elapsed due to instrumental preparation. Therefore, OOP (100) peak evolution during the initial 60 s could not be tracked. The intensity profiles as a function of evaporation times, are shown in **Figure 2.10a, b**. CF evaporates faster than the secondary solvents, due to its high vapor pressure. Then the final morphology develops in a more concentrated secondary solvent environment. Changes in d-spacings, d_{100} and crystallite sizes, D_{100} were obtained from the intensity profiles and given in **Figure 2.10a'** and **2.10b'**. The d_{100} spacings of PDPPBT stabilize after ~150-200 s, with similar values for both CF/pXY and CF/CB. However, it is quite interesting to observe the distinctive difference in D_{100} growth for these two

systems. D_{100} (crystallite size) growth is much faster in CF/CB system than in CF/pXY (**Figure 2.10a', b'**). It stabilizes after 150 s for CF/CB, whereas it continues to grow slowly in CF/pXY and begins to stabilize after 620 s. This indicates that even after the majority solvents are evaporated, the residual solvents interact more with PDPPBT polymer in CF/pXY system than in the CF/CB case, thus aiding in increasing the crystallite size in the BHJ blend processed with CF/pXY. The reason for this longer pXY-polymer interaction can be attributed to the unfavorable pXY-$PC_{71}BM$ interactions, as described earlier in section 2.3.4. This indicates that during the drying process, most of the $PC_{71}BM$ will crush out first in this CF/pXY system, forming large aggregates, while the polymer and remaining $PC_{71}BM$ continue to interact with the residual pXY, creating a fibrillar type networked structure. Both of these morphological features were observed by TEM in CF/pXY system (**Figure 2.4d**). On the other hand, such slow D_{100} growth was not observed in CF/CB system, indicating that the polymer network formation is stabilized first in this system, while $PC_{71}BM$ may still interact with the residual solvent and be deposited in between the fibrillar mesh created by the polymer. For the other polar solvent system, CF/Ani, a relatively faster growth of D_{100} was also observed as in the CF/CB system (**Figure 2.11**). Interestingly, D_{100} slightly decreases in the CF/DCB system. Most likely in this case, DCB is keeping the BHJ system in a swelling state due to its prolonged presence because of the very low vapor pressure. Thus, as it slowly evaporates, the swelled size slightly decreases. We note that the *in-situ* observation of the CF/TLN system was difficult due to its fast evaporation, therefore the CF/TLN data is not shown. **Figure 2.12** schematically

represents this morphology evolution mechanism from the non-polar and the polar solvent system.

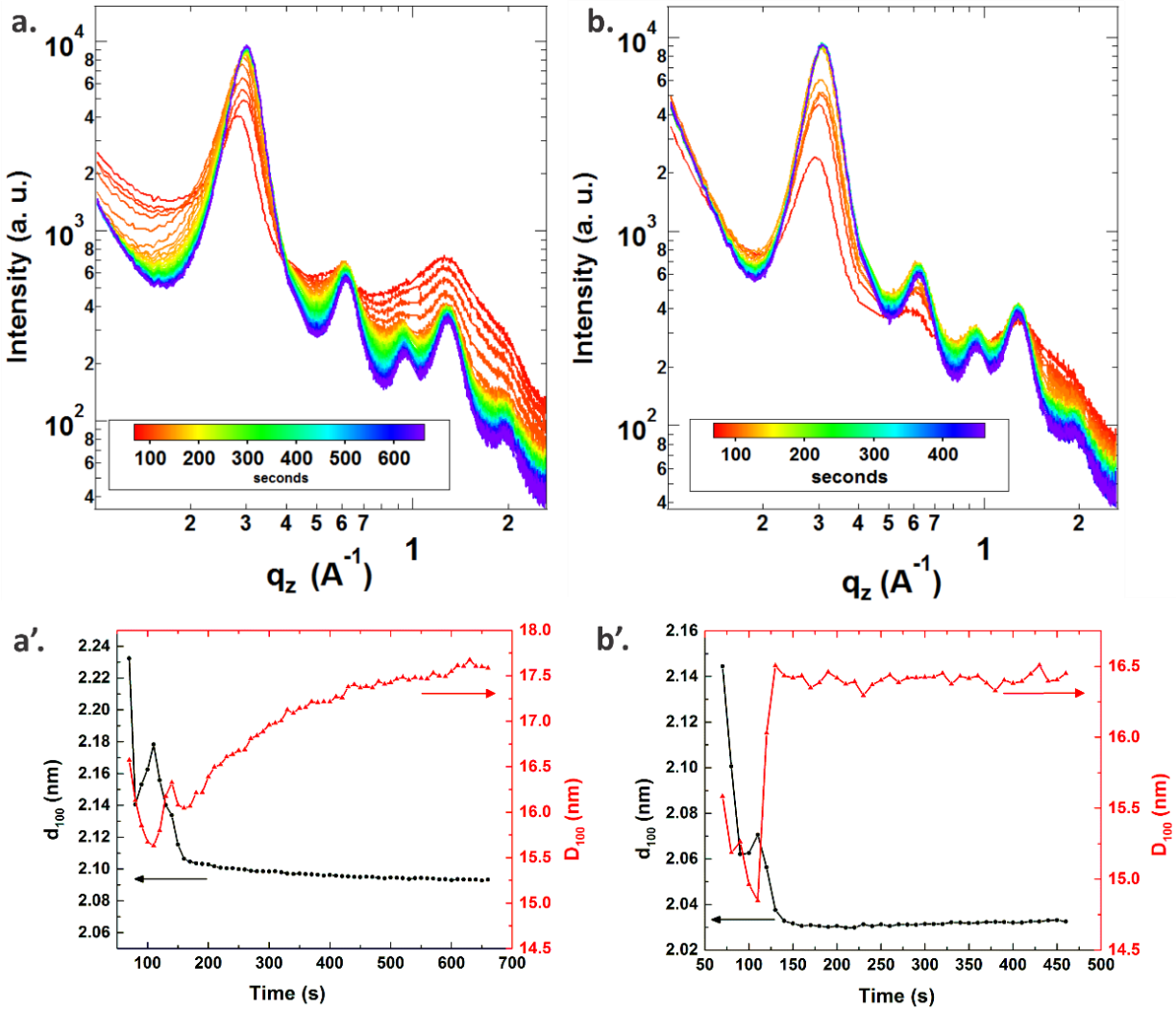

Figure 2.10 The out of plane (OOP) 1D GIWAXD profiles of PDPPBT:$PC_{71}BM$ blend films as a function of solvent evaporation time from the a) CF/pXY, and b) CF/CB systems. Change in OOP (100) d-spacings (d_{100}) and OOP (100) crystallite sizes (D_{100}) were obtained from these intensity profiles for a') CF/pXY, and b') CF/CB systems.

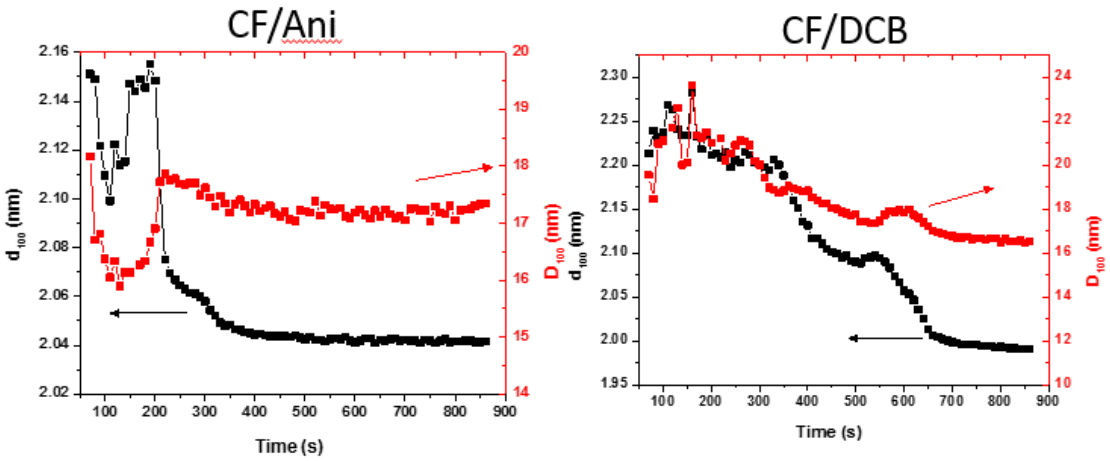

Figure 2.11 Change in OOP (100) d-spacings (d_{100}) and OOP (100) crystallite sizes (D_{100}) for CF/Ani and CF/DCB processed films.

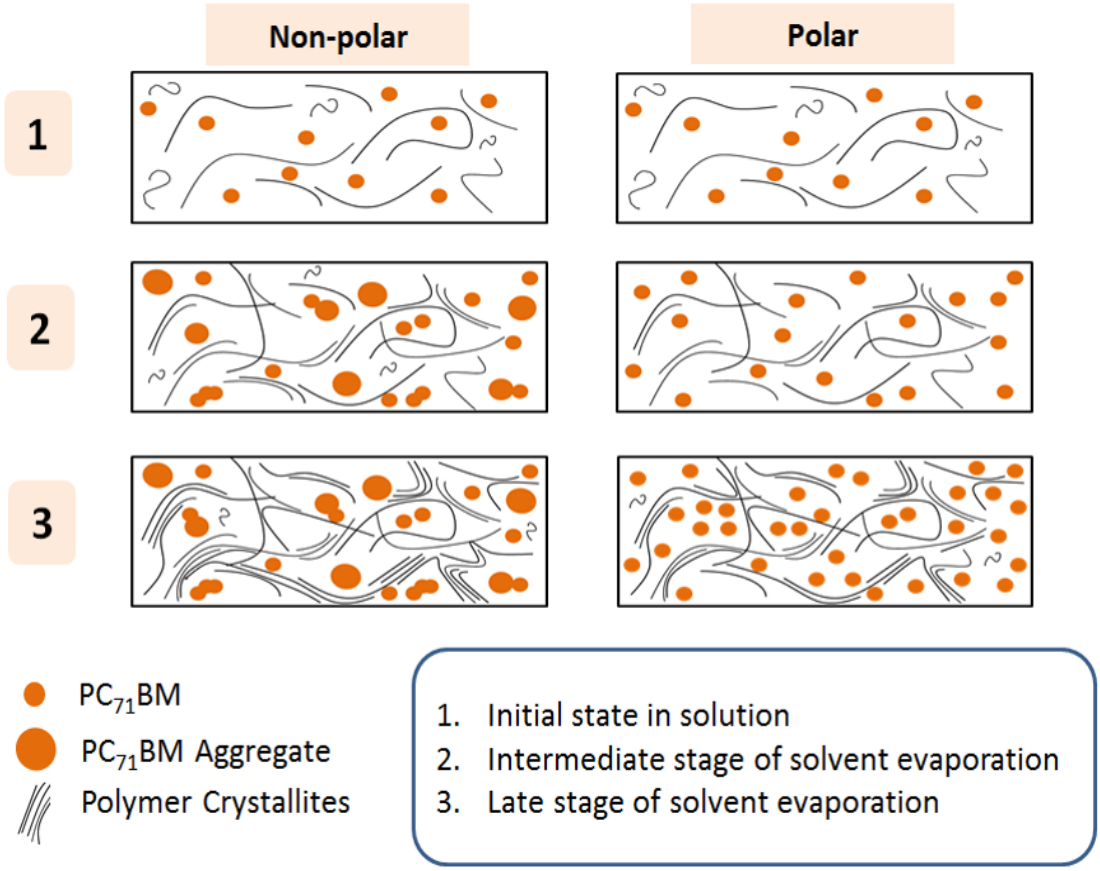

Figure 2.12 Schematic showing the morphology evolution mechanisms from the non-polar and the polar solvent system.

We note that the drop-cast films in our *in-situ* measurements are much thicker (~1 μm) than the spin-coated films. However, the fundamental principle regarding the morphology evolution and polymer chain packing, as a function of solvent evaporation time, would be similar for both drop-cast and spin-coated films. This is evidenced by the fact that polymer chain orientation remained the same (edge-on) in both spin-coated and drop-cast films of CF/pXY and CF/CB systems with very similar d-spacings (**Table 2.3** and **Figure 2.10a', 2.10b'**). A general consensus in additive-based BHJ devices is that the additive must have higher boiling point than the primary solvent, and it must have preferential interaction with one of the active layer components. In our case, pXY and TLN have higher boiling points compared to the primary solvent (CF), but they appear to preferentially interact more with the polymer rather than $PC_{71}BM$. This results in a larger PDPPBT D_{100} crystallite sizes in CF/pXY and CF/TLN systems, as observed here. This is also in agreement with the crystallite sizes observed from the spin coated samples (**Table 2.3**). This can qualitatively explain why much stronger vibronic peaks at 720 nm were observed in **Figure 2.1c**. However, any benefit of the increased crystallinity is diminished by the large agglomerates formed, due to the poor interaction of pXY and TLN with $PC_{71}BM$, demonstrating why pXY and TLN do not work as additives while CB, Ani, and DCB perform well in that regard.

2.4 Conclusion

In summary, polar and low vapor pressure secondary solvents were important for optimizing the BHJ morphology and enhancing device performance for PDPPBT:$PC_{71}BM$

system. DCB and Ani, the relatively lower vapor pressure and higher polarity secondary solvents, yielded the smallest fibril-to-fibril distance that was optimal for charge transport. In choosing the secondary solvents, it was found that solvent-$PC_{71}BM$ interactions were very critical for the formation of final morphology. Even with similar vapor pressures, an unfavorable solvent-$PC_{71}BM$ interaction, due to polarity mismatch, can produce drastically different morphology, consequently also affecting the growth process of polymer crystallites. In addition, when the vapor pressure was very low within the polar solvent systems, crystallite size was found to decrease as solvent evaporated, which was opposite to the results observed for the polar solvents with relatively higher vapor pressures. This can indicate that the polar solvent with low vapor pressure, may act as a plasticizer by keeping the BHJ in a swelling state due to its longer retention time. This underscores the importance of the morphology evolution mechanisms that can be drastically different due to the complex interplay of interactions between the components. These results provide a guideline in choosing the most suitable solvents by considering the effects of polarity, solubility as well as vapor pressure to control the morphology in the PDPPBT:$PC_{71}BM$ system or other additive-based processing of similar low band gap polymer system so as to optimize performance.

2.5 References

[1] S. E. Shaheen, C. J. Brabec, N. S. Sariciftci, F. Padinger, T. Fromherz, J. C. Hummelen, *Appl. Phys. Lett.* **2001**, *78*, 841.

[2] J. Liu, Y. Shi, Y. Yang, *Adv. Funct. Mater.* **2001**, *11*, 1.

[3] H. Hoppe, M. Niggemann, C. Winder, J. Kraut, R. Hiesgen, a. Hinsch, D. Meissner, N. S. Sariciftci, *Adv. Funct. Mater.* **2004**, *14*, 1005.

[4] L.-J. Zuo, X.-L. Hu, T. Ye, T. R. Andersen, H.-Y. Li, M.-M. Shi, M. Xu, J. Ling, Q. Zheng, J.-T. Xu, E. Bundgaard, F. C. Krebs, H.-Z. Chen, *J. Phys. Chem. C* **2012**, *116*, 16893.

[5] F. Liu, Y. Gu, J. W. Jung, W. H. Jo, T. P. Russell, *J. Polym. Sci. Part B Polym. Phys.* **2012**, *50*, 1018.

[6] D. M. DeLongchamp, R. J. Kline, A. Herzing, *Energy Environ. Sci.* **2012**, *5*, 5980.

[7] J. Peet, J. Y. Kim, N. E. Coates, W. L. Ma, D. Moses, a J. Heeger, G. C. Bazan, *Nat. Mater.* **2007**, *6*, 497.

[8] Y. Yao, J. Hou, Z. Xu, G. Li, Y. Yang, *Adv. Funct. Mater.* **2008**, *18*, 1783.

[9] M. M. Wienk, M. Turbiez, J. Gilot, R. A. J. Janssen, *Adv. Mater.* **2008**, *20*, 2556.

[10] F. Liu, Y. Gu, C. Wang, W. Zhao, D. Chen, A. L. Briseno, T. P. Russell, *Adv. Mater.* **2012**, *24*, 3947.

[11] Y. Gu, C. Wang, T. P. Russell, *Adv. Energy Mater.* **2012**, *2*, 683.

[12] W. Chen, T. Xu, F. He, W. Wang, C. Wang, J. Strzalka, Y. Liu, J. Wen, D. J. Miller, J. Chen, O. K. Hong, O. L. Yu, S. B. Darling, *Nano Lett.* **2011**, *11*, 3707.

[13] W. Chen, M. P. Nikiforov, S. B. Darling, *Energy Environ. Sci.* **2012**, *5*, 8045.

[14] A. Pivrikas, H. Neugebauer, N. S. Sariciftci, *Sol. Energy* **2011**, *85*, 1226.

[15] J. Bijleveld, *J. Am. Chem. Soc.* **2009**, *131*, 16616.

[16] W. Li, W. S. C. Roelofs, M. M. Wienk, R. a J. Janssen, *J. Am. Chem. Soc.* **2012**, *134*, 13787.

[17] C. Reichardt, *Solvents and Solvent Effects in Organic Chemistry*, WILEY-VCH Verlag GmbH & Co. KGaA, Weinheim, **2003**.

[18] C. M. Hansen, *Hansen Solubility Parameters A User's Handbook*, CRC Press, Boca Raton, **2007**.

[19] J. Rivnay, S. C. B. Mannsfeld, C. E. Miller, A. Salleo, M. F. Toney, *Chem. Rev.* **2012**, *112*, 5488.

[20] M. Y. Chiu, U. S. Jeng, C. H. Su, K. S. Liang, K. H. Wei, *Adv. Mater.* **2008**, *20*, 2573.

[21] H.-C. Liao, C.-S. Tsao, T.-H. Lin, C.-M. Chuang, C.-Y. Chen, U.-S. Jeng, C.-H. Su, Y.-F. Chen, W.-F. Su, *J. Am. Chem. Soc.* **2011**, *133*, 13064.

[22] S. Swaraj, C. Wang, H. Yan, B. Watts, J. Lüning, C. R. McNeill, H. Ade, *Nano Lett.* **2010**, *10*, 2863.

[23] H. Ade, A. P. Hitchcock, *Polymer (Guildf).* **2008**, *49*, 643.

[24] B. A. Collins, J. E. Cochran, H. Yan, E. Gann, C. Hub, R. Fink, C. Wang, T. Schuettfort, C. R. McNeill, M. L. Chabinyc, H. Ade, *Nat. Mater.* **2012**, *11*, 536.

[25] A. F. M. Barton, *Chem. Rev.* **1975**, *75*, 731.

[26] B. Walker, A. Tamayo, D. T. Duong, X. D. Dang, C. Kim, J. Granstrom, T. Q. Nguyen, *Adv. Energy Mater.* **2011**, *1*, 221.

[27] K. R. Graham, P. M. Wieruszewski, R. Stalder, M. J. Hartel, J. Mei, F. So, J. R. Reynolds, *Adv. Funct. Mater.* **2012**, *22*, 4801.

[28] F. MacHui, S. Langner, X. Zhu, S. Abbott, C. J. Brabec, *Sol. Energy Mater. Sol. Cells* **2012**, *100*, 138.

[29] B. A. Collins, Z. Li, J. R. Tumbleston, E. Gann, C. R. Mcneill, H. Ade, *Adv. Energy Mater.* **2013**, *3*, 65.

CHAPTER 3

DEVELOPMENT OF SLOT-DIE COATING METHODOLOGIES: FAST PRINTING AND *IN-SITU* MORPHOLOGY OBSERVATION OF PDPPBT/$PC_{71}BM$ SOLAR CELLS

3.1 Introduction

One of the major driving forces behind the recent vast scientific research effort on polymer based solar cells is grounded on the argument of low processing cost. The idea is to utilize its solution processability to fabricate large area flexible devices using a roll-to-roll coating method.[1–3] To date, the power conversion efficiency (PCE) has been over 10%[4], however, majority of the reported PCEs in the literature are based on small area devices fabricated by spin-coating methods. Translation to large-size-scale devices has always been met with significant reductions in the PCE.[5,6] This can be attributed, in part, to the differences in the methods of preparation. Spin coating is routinely used to prepare laboratory-scale devices, while industrial processes have used blade coating or slot-die coating processes in a roll-to-roll (R2R) setting.[5,7] These coating processes are fundamentally different in terms of solvent removal rate, which is critical in defining the kinetically trapped morphologies encountered in the generation of the active layers.[8,9] Therefore, understanding the morphology evolution by industrial-coating process is of critical importance in the next phase of OPV research.

In this chapter, we present the use of a mini slot-die coating system to fabricate OPV devices, using coating parameters that are applicable to larger scale processes, using very small quantities of materials and, as such, can be used to investigate a large number

of materials at minimal cost. The slot-die coater was used in conjunction with grazing-incidence wide angle X-ray diffraction (GIWAXD) to study the evolution of the morphology over a wide range of length scales at different film drying conditions. The best performing solvent additive, 1,2-dichlorobenzene (DCB) from Chapter 2 was used with the same active layer materials (PDPPBT/$PC_{71}BM$) system to investigate the transfer of spin-coating conditions to slot-die coating conditions. Although a 20% (v/v) solvent additive (DCB) was found to give 5.0% efficiency in the spin-coated devices (Chapter 2), a much smaller amount of solvent additive (5% v/v) was required to obtain the comparable efficiency of 5.2% in the slot-die processed devices.

3.2 Experimental

3.2.1 Materials and Methods

PDPPBT was synthesized in our lab by Dr. Feng Liu and $PC_{71}BM$ were purchased from Nano-C Inc. All solvents were purchased from Sigma-Aldrich and used without further purifications. Large indium tin oxide (ITO) coated glass were purchased from Thin Film Devices Inc. The thickness and the resistivity of the ITO was 145 ± 10 nm and 20 ± 2 ohms/sq, respectively. Poly(3,4-ethylenedioxythiophene): polystyrene sulphonate (PEDOT: PSS) was purchased from CLEVIOS^{TM}.

3.2.2 Device Preparation and Characterization

All devices were fabricated in a conventional geometry with the structure: ITO/PEDOT:PSS/BHJ/LiF/Al. To prevent contamination of the slot-die head, PEDOT:PSS was first spin-coated on cleaned ITO substrates at 2800 RPM for 1 min followed by heating

at 150°C for 15 min, yielding a thickness of 30 nm. Subsequently, all active layer solutions were fabricated using the mini slot-die coater with a coating speed of 10 mm/s, head to substrate gap of ~ 100 μm, and a solution injection rate of 0.2 mL/min. LiF (1.5 nm) and Al (100 nm) were sequentially thermally evaporated to complete the device. The final thickness of the active layer was ~100 nm. The current-voltage characteristics of the devices were measured inside a glove-box with simulated AM1.5G irradiation (100 mW cm^{-2}) using a Xe lamp-based Newport 91160 300-W solar simulator. A photo-mask was used to define the active area.

3.2.3 Morphology and Structure Characterizations

The scattering characterization of the active layer morphology was performed at the Advanced Light Source, Lawrence Berkeley National Laboratory at beamlines 7.3.3 (GIWAXD) and 11.0.1.2 (RSoXS). The slot-die set up was mounted within the GIWAXD chamber for the real time measurements. Samples were coated on PEDOT:PSS coated Si substrates to mimic the device configurations. Bright field TEM experiments were performed with a JEOL 2000 FX TEM operating at an accelerating voltage of 200 kV.

3.3 Results and Discussions

3.3.1 Slot-Die Set Up

A schematic of the slot-die components is shown in **Figure 3.1**. The substrate can be securely held on the linear translation stage (substrate stage) by application of vacuum. The position of the translation stage can be electronically controlled using the motor software. The tilt angle and the position of the slot-die head are adjusted manually

using the die-alignment manipulator stage. The BHJ solution can be transferred through the slot-die solution feeding system onto PEDOT:PSS coated ITO substrates using a syringe pump, followed by moving the substrate stage at a constant speed, and thus producing a homogeneous wet film. Furthermore, solution injection rate can be controlled electronically by the syringe pump software. Generally, the speed of the translation stage (or, web speed or, coating speed) and the flow rate of the solution feed determine the wet film thickness. The following equation[10] estimates the thickness of the dry film:

$$d = \frac{f}{Sw} \times \frac{c}{\rho}$$

where, d is the thickness (cm), f is the flow rate ($cm^3\ min^{-1}$), w is the coating width (cm), S is the coating speed ($cm\ min^{-1}$), c is the solid content in the ink ($g\ cm^{-3}$), and ρ is the density of the dried ink material ($g\ cm^{-3}$).

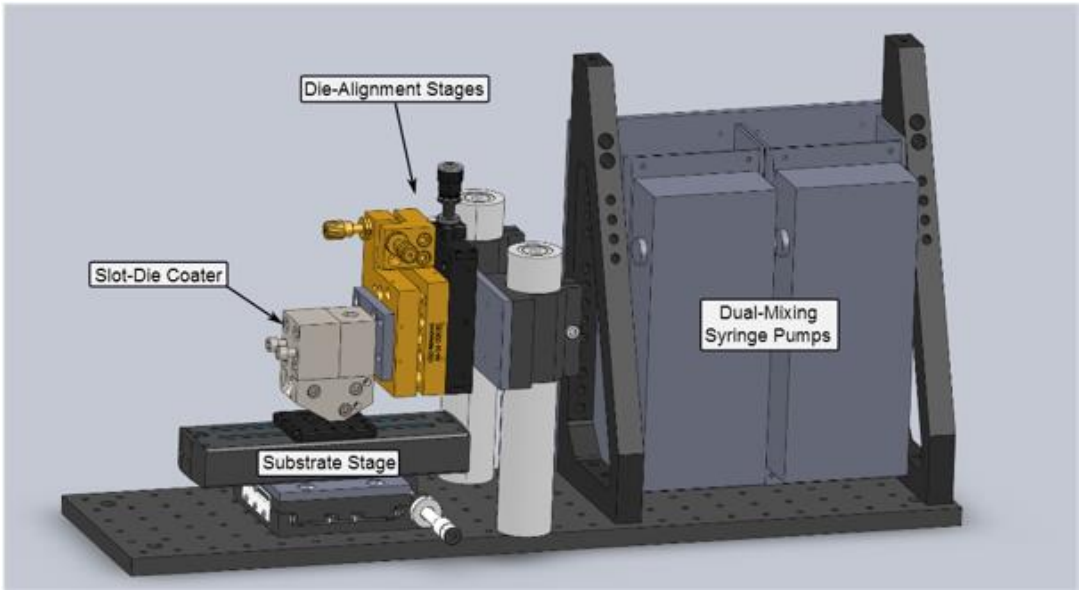

Figure 3.1 Schematic of the slot-die set up.

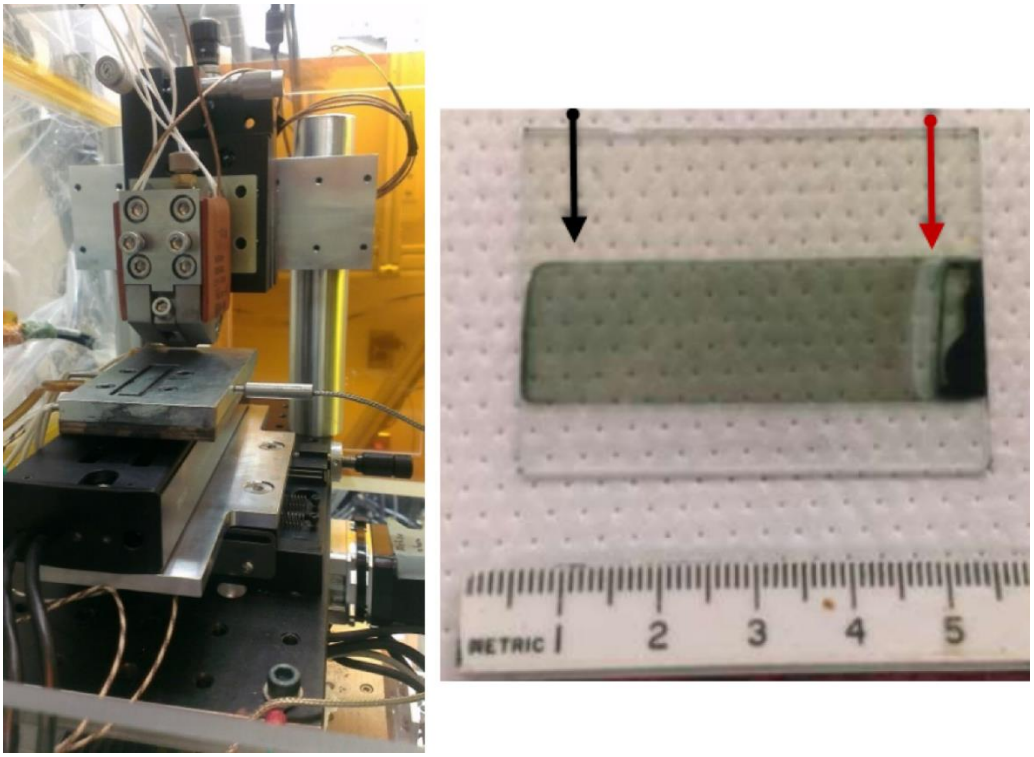

Figure 3.2 The actual set up (left) with a representative PDPPBT/$PC_{71}BM$ BHJ film (right). The black and the red arrows indicate the start and the end of coating, respectively.

The actual set-up is shown in **Figure 3.2** (left) with a representative PDPPBT/ $PC_{71}BM$ BHJ film (right). Smooth and continuous BHJ thin films of 100 nm thickness can be routinely obtained by tuning the substrate to head gap, solution concentrations, and coating speeds. Temperature controlled processing is also enabled by incorporating flexible heating pads on the slot-die head, as well as cartridge heaters inside the substrate holder. For the study presented here, ITO substrate was pre-coated with a layer of 30 nm PEDOT:PSS. All devices were fabricated in air under a nitrogen flow, unlike typical fabrication of OPV cells in a glove box with inert conditions. A coating speed of 10 mm/s with a solution injection rate of 0.2 mL/min were used to control the film thickness at room temperature.

3.3.2 Device Characteristics

As described in Chapter 2, chloroform (CF) is the major solvent, and 1,2-dichlorobenzene (DCB) is the minor solvent that was used as a solvent additive. Here, the concentration of the solvent additive was varied (5%, 20%, and 50% v/v) to investigate the influence of the solvent concentration on the morphology and the device performance of slot-die processed BHJ films. Device statistics are shown in **Figure 3.3**. The V_{oc} of the devices fabricated from the different solvent mixtures are quite similar. Fill factors (FF) were slightly higher for the devices prepared from a low DCB concentration. The best average efficiency (5.2%) was obtained from devices prepared from a 5% DCB solution, with a maximum efficiency of 5.5% recorded. This value is slightly higher than that obtained from the optimized spin-coated devices using the 20% DCB solution. This result indicates that the slot-die coating also yields high-efficiency devices.

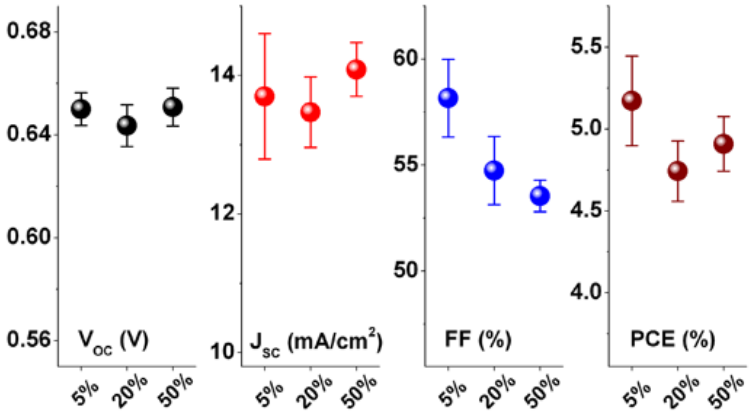

Figure 3.3 Device Statistics from 5%, 20%, and 50% DCB processed BHJs.

3.3.3 Bulk Morphology

Thin-film morphologies of the slot-die processed BHJ films were characterized by transmission electron microscopy (TEM) and resonant soft X-ray scattering (RSoXS).[12] Shown in **Figure 3.4a** are the TEM results for films prepared with different ratios of DCB and CF. All films showed a fibrillar mesh network with a close inter-fibrillar spacing. Thin films coated from 5% DCB showed a well-developed scattering reflection at ~0.016 A^{-1}, corresponding to a spacing of ~40 nm. Films coated from 20% to 50% DCB showed features on a similar length scale, but the reflections were weaker and less pronounced. The 40 nm length scale is attributed to average mesh size or average center-to-center distance between the fibrils. Increasing the DCB content (20% and 50%) led to a reduction in this length scale indicating the presence of a larger amount of fibrils due to the poorer quality of the solvent toward DPPBT. In addition, with the increase of DCB concentrations, a new length scale was observed at lower q (**Figure 3.4b**). In films cast from 20% DCB, an interference at ~0.0029 A^{-1} was observed, corresponding to a distance of 220 nm; and in films cast from 50% DCB solutions, a pronounced upturn of scattering is seen at very low scattering vectors. These large-scale features can be ascribed to aggregates of $PC_{71}BM$. The scattering results are supported by the TEM images where domains (darker regions in the images) are observed that increase in size with increasing DCB concentration, which reduces the average $PC_{71}BM$ concentration within the effective active layer (fibril network area with small-sized phase separation), giving rise to the lower FF.

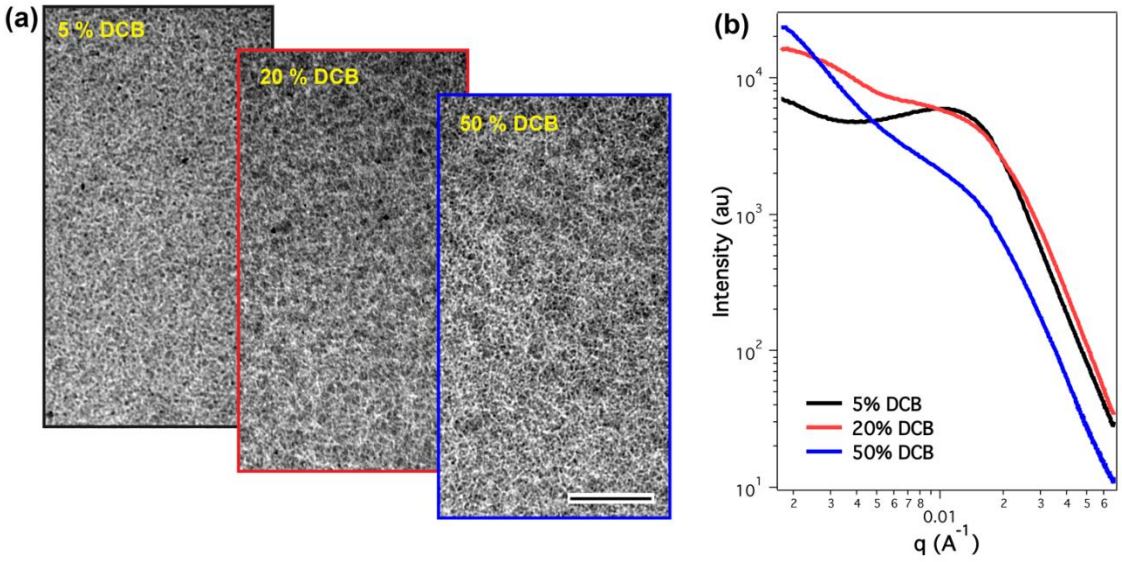

Figure 3.4 a) Transmission electron microscopy images and b) resonant soft X-ray scattering of BHJ blends cast from different solvent composition fusing the mini-slot-die coater. The scale bar in TEM images is 500 nm.

3.3.4 *In-situ* Morphology Evolution

The real-time evolution of the morphology was investigated by *in-situ* GIWAXD.[13–18] The slot-die coater was integrated with the sample chamber in a helium atmosphere. A slight flow of helium was maintained during the data acquisition in order to reduce the air scattering. The coating speed was kept the same as the device preparation conditions (10 mm/s), with the synchrotron beam incident on the sample substrate at a fixed distance from the die. The coating and data acquisition was started simultaneously which enabled the *in-situ* characterization as a function of solvent evaporation time. **Figure 3.5a** shows the 1D line profiles in the out-of-plane (OOP) directions, and the corresponding analysis of the (100) reflections is given in **Figure 3.5b**. The top panel represents data from 5%, the middle panel from the 20%, and the bottom panel from the 50% DCB solutions. It is evident that polymer ordering ((100) peak area) occurs much more rapidly in the 5%

DCB processed film than in the 20% or 50% processed films. This is due to the rapid evaporation of CF, giving rise to a deterioration of the overall solvent quality, which consequently results in an early aggregation and ordering of the PDPPBT chains compared to the 20% and the 50% samples. For the 20% and the 50% films, CF will also evaporate rapidly, however, due to the larger amount of the remainder DCB in these situations, the onset of polymer aggregations are delayed. The different CF:DCB compositions will also lead to the different solute concentrations in DCB, at any given time, since CF evaporates more rapidly than DCB. The saturation limit of the PDPPBT in the mixed solvent will be influenced by the total polymer concentration, which in turn, will also influence the growth and connectivity of the aggregates formed.[19]

Furthermore, similar to Chapter 2, a decrease in d-spacing (red symbols) was observed as a function of solvent evaporation time for all three DCB compositions. The final d-spacing values were similar for all cases. Moreover, a slight decrease in the crystallite size (also referred as the coherence length) was observed in these CF/DCB slot-die processed films (**Figure 3.5**) as in the CF/DCB results in Chapter 2 (**Figure 2.11**). It should be also noted that in Chapter 2, an increase in crystallite size (coherence length) was observed for the rest of the solvent systems (CF/pXY, CF/CB, CF/Ani). This most likely indicates that if a solvent additive remains in the film for a prolonged period of time due to its low vapor pressure, it may act as a plasticizer by keeping the BHJ in a swelling state. Thus, the crystallite size/coherence length will also be swelled initially and will decrease as the solvent additive slowly evaporates. Therefore, we anticipate that the other relatively high vapor pressure additives in

Chapter 2 (CF/TLN, CF/pXY, CF/CB, CF/Ani), where an increase in the crystallite size was observed as the solvent additive evaporated, to act as simply a poor solvent without any additional plasticizing behavior as in the CF/DCB case.

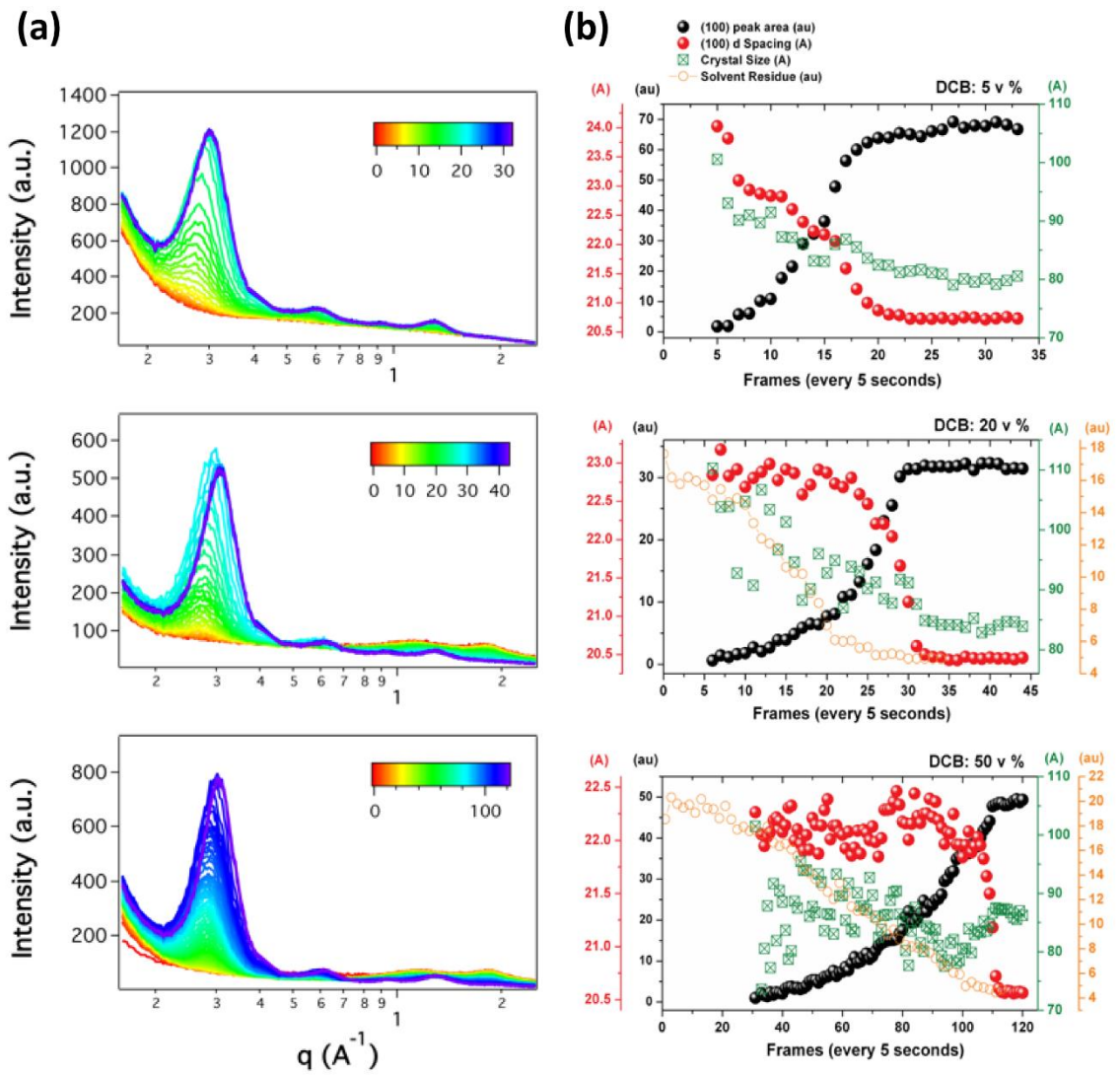

Figure 3.5 *In-situ* GIWAXD scattering results.[20] Top, middle and bottom panels are from 5%, 20%, and 50% DCB solutions, respectively. a) I*n-situ* GIWAXD scattering profiles. b) Corresponding analysis of the OOP (100) peaks arising from PDPPBT. Peak fitting was used to estimate the d-spacing (red), relative crystallinity (black), and crystal size information (green). Residual solvent content is also shown in orange for the 20% and 50% DCB case.

3.4 Conclusion

In summary, this chapter demonstrated the device fabrication of PDPPBT:$PC_{71}BM$ system using a mini slot-die coater. The device performance was comparable with those of the spin-coated devices. However, the best device performance was obtained when only 5% DCB was used as the solvent additive, whereas 20% DCB gave the best performance in the spin-coated devices as discussed in Chapter 2. The mini-slot-die coater was also used in concert with GIWAXD so as to obtain *in-situ*, real-time characterization of the morphology evolution during solution-casting process.

3.5 References

[1] B. C. Thompson, J. M. J. Fréchet, *Angew. Chemie - Int. Ed.* **2008**, *47*, 58.

[2] S. Gu, H. Neugebauer, N. S. Sariciftci, *Chem.Rev.* **2007**, *107*, 1324.

[3] C. J. Brabec, S. Gowrisanker, J. J. M. Halls, D. Laird, S. Jia, S. P. Williams, *Adv. Mater.* **2010**, *22*, 3839.

[4] J. You, L. Dou, K. Yoshimura, T. Kato, K. Ohya, T. Moriarty, K. Emery, C.-C. Chen, J. Gao, G. Li, Y. Yang, *Nat. Commun.* **2013**, *4*, 1446.

[5] F. C. Krebs, T. Tromholt, M. Jorgensen, *Nanoscale* **2010**, *2*, 873.

[6] F. C. Krebs, J. Fyenbo, D. M. Tanenbaum, S. a. Gevorgyan, R. Andriessen, B. van Remoortere, Y. Galagan, M. Jørgensen, *Energy Environ. Sci.* **2011**, *4*, 4116.

[7] R. Søndergaard, M. Hösel, D. Angmo, T. T. Larsen-Olsen, F. C. Krebs, *Mater. Today* **2012**, *15*, 36.

[8] F. Liu, Y. Gu, X. Shen, S. Ferdous, H. W. Wang, T. P. Russell, *Prog. Polym. Sci.* **2013**, *38*, 1990.

[9] F. Liu, Y. Gu, J. W. Jung, W. H. Jo, T. P. Russell, *J. Polym. Sci. Part B Polym. Phys.* **2012**, *50*, 1018.

[10] F. C. Krebs, *Sol. Energy Mater. Sol. Cells* **2009**, *93*, 394.

[11] F. C. Krebs, *Sol. Energy Mater. Sol. Cells* **2009**, *93*, 394.

[12] C. Wang, D. H. Lee, a Hexemer, M. I. Kim, W. Zhao, H. Hasegawa, H. Ade, T. P. Russell, *Nano Lett.* **2011**, *11*, 3906.

[13] J. T. Rogers, K. Schmidt, M. F. Toney, G. C. Bazan, E. J. Kramer, *J Am Chem Soc* **2012**, *134*, 2884.

[14] N. Shin, L. J. Richter, A. a. Herzing, R. J. Kline, D. M. DeLongchamp, *Adv. Energy Mater.* **2013**, *3*, 938.

[15] B. Schmidt-Hansberg, M. Sanyal, M. F. G. Klein, M. Pfaff, N. Schnabel, S. Jaiser, A. Vorobiev, E. Müller, A. Colsmann, P. Scharfer, D. Gerthsen, U. Lemmer, E. Barrena, W. Schabel, *ACS Nano* **2011**, *5*, 8579.

[16] M. Sanyal, B. Schmidt-Hansberg, M. F. G. Klein, A. Colsmann, C. Munuera, A. Vorobiev, U. Lemmer, W. Schabel, H. Dosch, E. Barrena, *Adv. Energy Mater.* **2011**, *1*, 363.

[17] M. Sanyal, B. Schmidt-Hansberg, M. F. G. Klein, C. Munuera, A. Vorobiev, A. Colsmann, P. Scharfer, U. Lemmer, W. Schabel, H. Dosch, E. Barrena, *Macromolecules* **2011**, *44*, 3795.

[18] A. J. Pearson, T. Wang, D. G. Lidzey, *Rep. Prog. Phys.* **2013**, *76*, 022501.

[19] T. Wang, A. D. F. Dunbar, P. a. Staniec, A. J. Pearson, P. E. Hopkinson, J. E. Macdonald, S. Lilliu, C. Pizzey, N. J. Terrill, A. M. Donald, A. J. Ryan, R. a. L. Jones, D. G. Lidzey, **2010**, *6*, 4128.

[20] F. Liu, S. Ferdous, E. Schaible, A. Hexamer, M. Church, X. Ding, C. Wang, T. Russell, *Adv. Mater.* **2014**, *27*, 886.

CHAPTER 4

SLOT-DIE PROCESSING OF PTB7/$PC_{71}BM$ SOLAR CELLS: UNDERSTANDING THE ROLE OF ADDITIVE ON MORPHOLOGY AND DEVICE PERFORMANCE

4.1 Introduction

In recent years, the use of solvent additives has become ubiquitous in optimizing the morphologies of many high-efficiency, low-band-gap polymer active layers. A small amount of these additives were shown to either drastically reduce the size scale of the phase separated domains in the polymer/fullerene blends[1] or induce phase separation in the homogeneously mixed blends[2,3]. Among such additive-assisted systems, a thieno[3,4-b]-thiophene and benzodithiophene based low band-gap polymer (PTB7), was the first polymer system that gave power conversion efficiency (PCE) over 7% when blended with phenyl-C71-butyric acid methyl ester ($PC_{71}BM$)[4]. Inherent immiscibility[5] between PTB7 and $PC_{71}BM$ necessitates the use of a small amount of 1,8-diiodooctane (DIO) as the solvent additive to achieve an optimal morphology during solution casting. DIO, in this case, reduces the size scale of the phase separated domains of PTB7 and $PC_{71}BM$. Despite numerous studies dealing with the formation of a hierarchical morphology[6,7] of the active layer in this system, other observations of narrow and elongated domains[8], and an enrichment of the surface with PTB7 face-on crystals[9], a clear understanding of the role of DIO during the film formation remains unclear.

In this chapter, we attempt to elucidate the mechanistic influence of DIO on PTB7/$PC_{71}BM$ BHJ structures as the morphology evolution progresses. The mini slot-die

coater described in Chapter 3, will be used here as well. Slot-die coated devices will be optimized first, followed by studies on the influence of DIO on the evolution of the morphology during film formation process. Although, DIO is a poor solvent for PTB7, the results suggest a strong interaction between the DIO and the PTB7 polymer chains, even at supersaturated conditions. This was further confirmed by dielectric constant measurements of PTB7 in the solution phase with DIO. The final morphologies were also characterized by electron microscopy and resonant soft X-ray scattering.

4.2 Experimental

4.2.1 Materials and Methods

PTB7 and $PC_{71}BM$ were purchased from 1-Material Inc. and Nano-C Inc. Chlorobenzene (CB) and 1,8-diiodooctane (DIO) were purchased from Sigma-Aldrich. All materials were used without further purifications. Solutions were prepared from CB or CB/DIO mixtures with different concentrations and stirred overnight at 55 °C for complete dissolution. Large indium tin oxide (ITO) coated glass substrates (76.2mm x 25.4mm) were purchased from Thin Film Devices Inc. The thickness and the resistivity of the ITO was 145 ± 10 nm and 20 ± 2 ohms/sq, respectively. Poly(3,4-ethylenedioxythiophene): polystyrene sulphonate (PEDOT: PSS) was purchased from CLEVIOS™.

4.2.2 Device Preparation and Characterization

All devices were fabricated in a conventional geometry with the structure: ITO/PEDOT:PSS/BHJ/LiF/Al. To prevent contamination of the slot-die head, PEDOT:PSS was first spin-coated on cleaned ITO substrates at 2800 RPM for 1 min followed by heating

at 150°C for 15 min, yielding a thickness of 30 nm. Subsequently, all active layer solutions were fabricated using the mini slot-die coater with a coating speed of 10 mm/s, head to substrate gap of ~ 100 µm, and a solution injection rate of 0.2 mL/min. The wet films were vacuum dried for about 10 hr prior to thermal evaporation of the cathode layer (1.5 nm LiF and 100 nm Al). The final thickness of the active layer was 90-100 nm. The current-voltage characteristics of the devices were measured inside a glove-box with simulated AM1.5G irradiation (100 mW cm^{-2}) using a Xe lamp-based Newport 91160 300-W solar simulator. A photo-mask was used to define the active area. Impedance measurements were also performed inside the glove-box using an Agilent 4294A Precision Impedance Analyzer.

4.2.3 Morphology and Structure Characterizations

The characterization of the active layer morphology using scattering methods was performed at the Advanced Light Source, Lawrence Berkeley National Lab at beamlines 7.3.3 (GIWAXD and GISAXS) and 11.0.1.2 (RSoXS). The slot-die set up was mounted with the GIWAXD/GISAXS chamber for *in-situ* measurements. Samples were coated on PEDOT:PSS coated Si substrates to mimic the device configurations. Bright field TEM experiments were performed with a JEOL 2000 FX TEM operating at an accelerating voltage of 200 kV. UV-Vis spectra were collected using a spectrometer Lambda 25 (Perkin Elmer). The samples were prepared on PEDOT:PSS coated quartz substrates.

4.2.4 Solution Capacitance Measurement

Solution capacitance was measured using a liquid test fixture (Agilent 16452A) connected with the Agilent 4294A Precision Impedance Analyzer. The test fixture employs the parallel plate method, which sandwiches the liquid material between two electrodes to form a capacitor. All measurements were performed at room temperature.

4.3 Results and Discussions

4.3.1 Miscibility of PTB7 and $PC_{71}BM$

A preliminary experiment was performed with a series of PTB7:$PC_{71}BM$ thin films, processed with and without DIO (3% v/v), by varying polymer concentrations ranging from 6.2 w% to 40 w% with respect to the $PC_{71}BM$ content to determine the onset of phase separation between these components. The chemical structures of PTB7 and $PC_{71}BM$ are shown in **Figure 4.1**. Bright field TEM micrographs are shown in **Figure 4.2** for different PTB7:$PC_{71}BM$ mixture compositions. The top panel represents the blends cast from only CB solutions and the bottom panel represents the blends cast from CB/DIO solutions. All films were vacuum dried overnight to remove excess DIO prior to the TEM experiments.

The onset of large-scale phase separation in these kinetically trapped morphologies occurred when the polymer content is ~16.7 w% of the total solid content (**Figure 4.2b**), and the length scale of this phase separation stabilizes when the polymer content approaches ~34.8 w% (**Figure 4.2d, e**). The large size aggregates (darker areas in **Figure 4.2**) are due to the $PC_{71}BM$ phase, as observed previously by us and others.[10,7,11,5]

When DIO was used as the solvent additive, the size scale of the phase separated domains was reduced and a fibrillar type bicontinuous network structure with large interfacial areas was observed (**Figure 4.2, bottom panel**). Furthermore, upon addition of DIO, the mesh size of the fibrillar network decreases as the polymer content progressively increased (**Figure 4.2b'-e'**) to 40 w%. This implies that a certain composition of the active material components, relative to the DIO, is required to effectively generate the bicontinuous morphology.

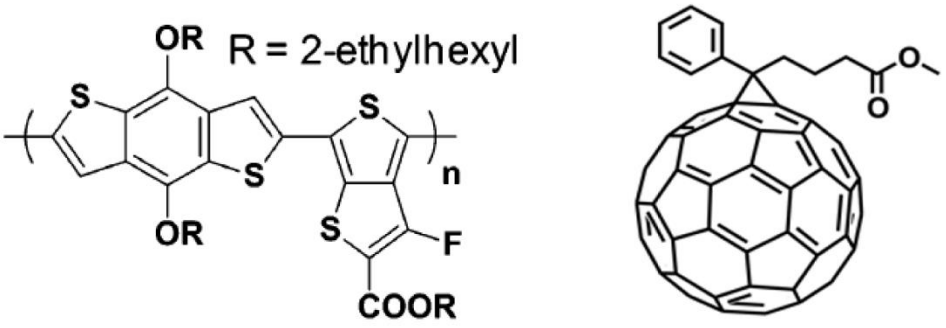

Figure 4.1 Chemical structures of PTB7 (left) and $PC_{71}BM$ (right).

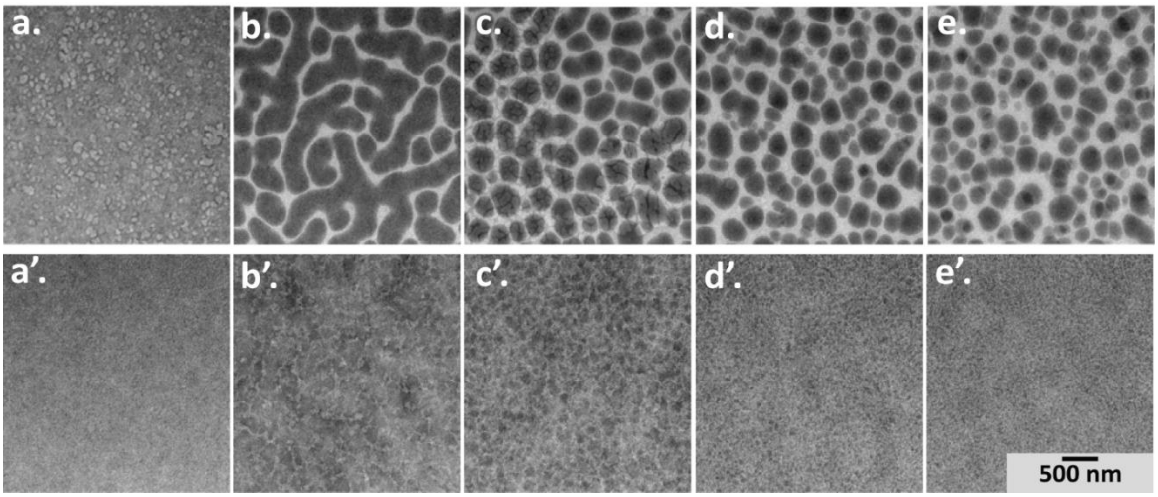

Figure 4.2 TEM micrographs of PTB7:$PC_{71}BM$ blend thin films: CB processed films (top panel) and CB:DIO (97:30 v/v) processed films (bottom panel). a, a') $PC_{71}BM$: PTB7 = 15 mg : 1 mg; b, b') $PC_{71}BM$: PTB7 = 15 mg : 3 mg; c, c') $PC_{71}BM$: PTB7 = 15 mg : 5 mg; d, d') $PC_{71}BM$: PTB7 = 15 mg : 8 mg; e, e') $PC_{71}BM$: PTB7 = 15 mg : 10 mg.

4.3.2 Device Characteristics

Three different DIO concentrations (1%, 2%, and 3% by volume) were used to investigate the device performances of the slot-die processed PTB7:$PC_{71}BM$ (1:1.5) BHJ active layers. The details of device fabrication using the mini slot-die coater is described in Chapter 3.[12] Briefly, the BHJ solution was transferred through the slot-die solution feeding system onto PEDOT:PSS coated ITO substrates, followed by moving the substrate at a constant speed, and thus, producing a homogeneous wet film. The excess solvent was then removed by placing the wet films under vacuum for 8-10 hours, followed by thermal depositions of 1.5 nm LiF and 100 nm Al as the top electrode. A representative film, before and after the depositions of the top electrode, is given in **Figure 4.3**. It should be noted that the coating process was performed in air under a nitrogen flow, unlike typical fabrication of OPV cells in a glove box with inert conditions. The completed devices were then measured in the glove-box under 100 mW/cm^2 simulated solar irradiation. A photomask was used to define the active areas (0.05 cm^2, 0.11 cm^2, and 0.31 cm^2). Representative current density - voltage (J-V) plots from the devices with 0.11 cm^2 active area are shown in **Figure 4.4a** and corresponding device statistics are given in **Table 4.1**.

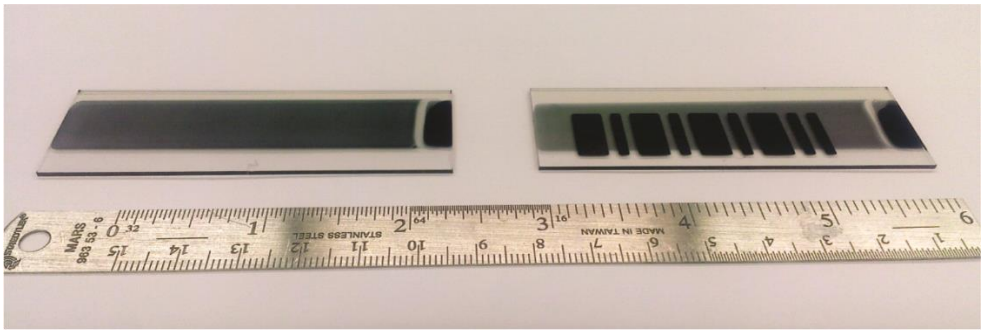

Figure 4.3 Representative slot-die coated BHJ films before (left) and after (right) top electrode deposition.

BHJ films fabricated from 1% DIO had poor performance with an average PCE of 5.58%. This is expected due to the small amount of processing additive. Earlier studies on spin coated active layers reported[9] the use of ~3 vol% DIO as the optimized condition to achieve a PCE of ~7.4-7.7% in a conventional device geometry (ITO/PEDOT:PSS/BHJ/LiF or Ca/Al). From our slot-die processed BHJ films, an average PCE of 7.53% (average of 10 devices) was achieved from 2% DIO processed films. When 3% DIO was used, the PCE further increased to 8.02% (average of 10 devices) which is considerably higher than the spin-coated devices in the same geometry. The highest PCE from the 3% DIO processed active layer was 8.14% with corresponding FF, J_{sc} and V_{oc} values of 67.1%, 16.63 mA/cm^2, and 0.73 V, respectively. To the best of our knowledge, this is the highest reporting efficiency from a continuous coating method to date. It is evident that the substantial increase in PCEs of the 2% and 3% DIO processed films, compared to the 1% DIO film, arose from enhancements in the J_{sc} and the FF, while the average V_{oc} decreased slightly for these 2% and 3% DIO processed films (**Table 4.1 and Figure 4.4**).

Table 4.1 Device performance with standard deviations.

Sample	J_{sc} (mA/cm^2)	V_{oc} (V)	FF (%)	PCE (%)
1% DIO	14.2 ± 0.52	0.73 ± 0.015	54.3 ± 2.2	5.58 ± 0.29
2% DIO	16.5 ± 0.30	0.71 ± 0.018	64.4 ± 1.7	7.53 ± 0.17
3% DIO	16.7 ± 0.15	0.71 ± 0.014	67.5 ± 0.9	8.02 ± 0.07

These enhancements in J_{sc} and FF are a direct consequence of the photon absorption by the BHJ structure, as well as the charge carrier generation and extraction in the internal morphology. To further explore the device parameters that are responsible for this performance boost, impedance spectroscopy (IS) was used. IS measures resistive and capacitive responses, and has been recently employed in the OPV field to get a deeper understanding of the electrical losses that can occur in an operating device based on the differences in bulk morphology, interfacial contacts, as well as differences in device geometry.[13–15] Our measurements were carried out under 100 mW/cm^2 simulated solar irradiation at 0 V DC applied bias (short-circuit condition). A small AC bias of 20 mV was applied along with the sweeping frequency range of 100 Hz – 1 MHz. **Figure 4.4b** shows the Cole-Cole plots obtained from these devices where x-axis is the real component of impedance and y-axis represents the negative imaginary component of impedance. The experimental results (symbols) were fit with a commonly used simple equivalent circuit model[16,17] shown in the inset of **Figure 4.4b**. R_s represents the series resistance arising from the electrodes and the contact wires, whereas R_{hf} and C_{hf} are related to the interfacial charge transport resistance and capacitance, respectively, and can be extracted from the high frequency region of the Cole-Cole plot (closest to the origin).

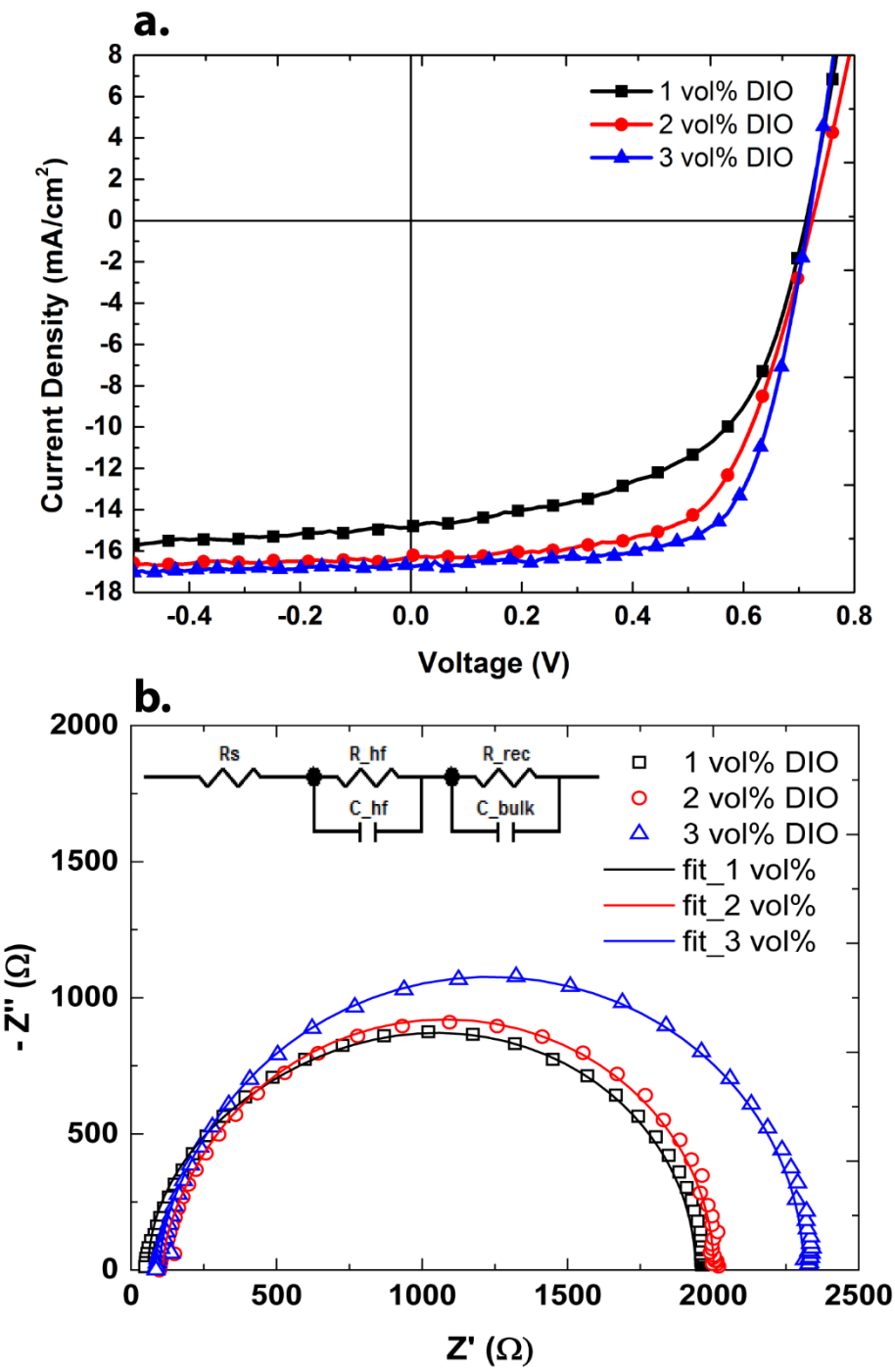

Figure 4.4 Device characteristics. a) Current density – voltage characteristics, and b) impedance measurements at 0 V DC applied bias under 100 mW/cm^2 simulated solar irradiation.

R_{rec} is the recombination resistance in the bulk that can be obtained from the low frequency region of the Cole-Cole plot (farthest from the origin) with the associated chemical capacitance, C_{bulk}. As seen in **Figure 4.4b** (solid lines), this equivalent circuit model gave good quality fits over the entire frequency range of the experimental data with chi-squared values less than 0.028. For the 1%, 2%, and 3% DIO processed devices, recombination resistances (R_{rec}), primarily from the photo-generated carriers, are 186, 218, and 255 Ω.cm^2 respectively, while the carrier transport resistances (R_{hf}) are 39.5, 8.5, and 10 Ω.cm^2 respectively (**Table 4.2**). To obtain the best efficiency from a device, a high recombination resistance and a low transport resistance are desirable, such that the maximum numbers of carriers are collected at the electrodes. The high recombination resistances and low transport resistances from these results are in accordance with the improved short-circuit current densities of the 2% and 3% DIO processed BHJs. This underscores the role DIO plays to effectively modulate the BHJ structures, which in turn reduces the electrical losses in the operating devices.

Table 4.2 Fitting results of impedance measurements.

Sample	R_s (Ω.cm^2)	R_{hf} (Ω.cm^2)	R_{rec} (Ω.cm^2)	C_{hf} (nF)	C_{bulk} (nF)
1% DIO	7.1	39.5	186	11.6	8.12
2% DIO	13.2	8.5	218	31.8	8.38
3% DIO	11.9	10	255	33.2	8.15

4.3.3 Bulk Morphology

The device performance discussed above are strongly correlated with the observed morphology, characterized by transmission electron microscopy (TEM) and resonance soft X-ray scattering[5] (RSoXS) shown in **Figure 4.5**. A well-defined scattering reflection at ~0.002 A^{-1} is observed (**Figure 4.5d**) for the 1% DIO processed film, equivalent to a spacing of ~310 nm which is in good agreement with the corresponding TEM micrograph. The majority of the photo-generated carriers in this large-scale phase separated morphology are likely to undergo a recombination process [18] (geminate and/or bimolecular type) without being able to transport through the entire film thickness, as evidenced by its smaller recombination resistance and large transport resistance from the IS results (**Table 4.2**). Conversely, 2% and 3% DIO processed BHJ films yield fibrillar-type networked morphologies with large interfacial areas between the donor and the acceptor moieties (**Figure 4.5 b, c**). From the RSoXS profiles, 2% DIO sample shows a scattering reflection at ~0.0042 A^{-1}, corresponding to a phase separated domain spacing of ~149 nm, with a second weak reflection at ~0.023 A^{-1}, corresponding to a length scale of ~27 nm. On the other hand, the diffuse reflection in the 3% DIO processed film shifted to ~ 0.0076 A^{-1}, corresponding to a distance of ~81 nm. It should be noted that it is difficult to observe the presence of the very weak shoulder in the higher q-range that would correspond to a ~30 nm domain spacing in this 3% DIO processed sample, compared to the 2% sample. However, the presence of a scattering reflection in this q-range (equivalent to smaller length scale fibrillary-type network) is very clear in the GISAXS profile which will be discussed later in this chapter.

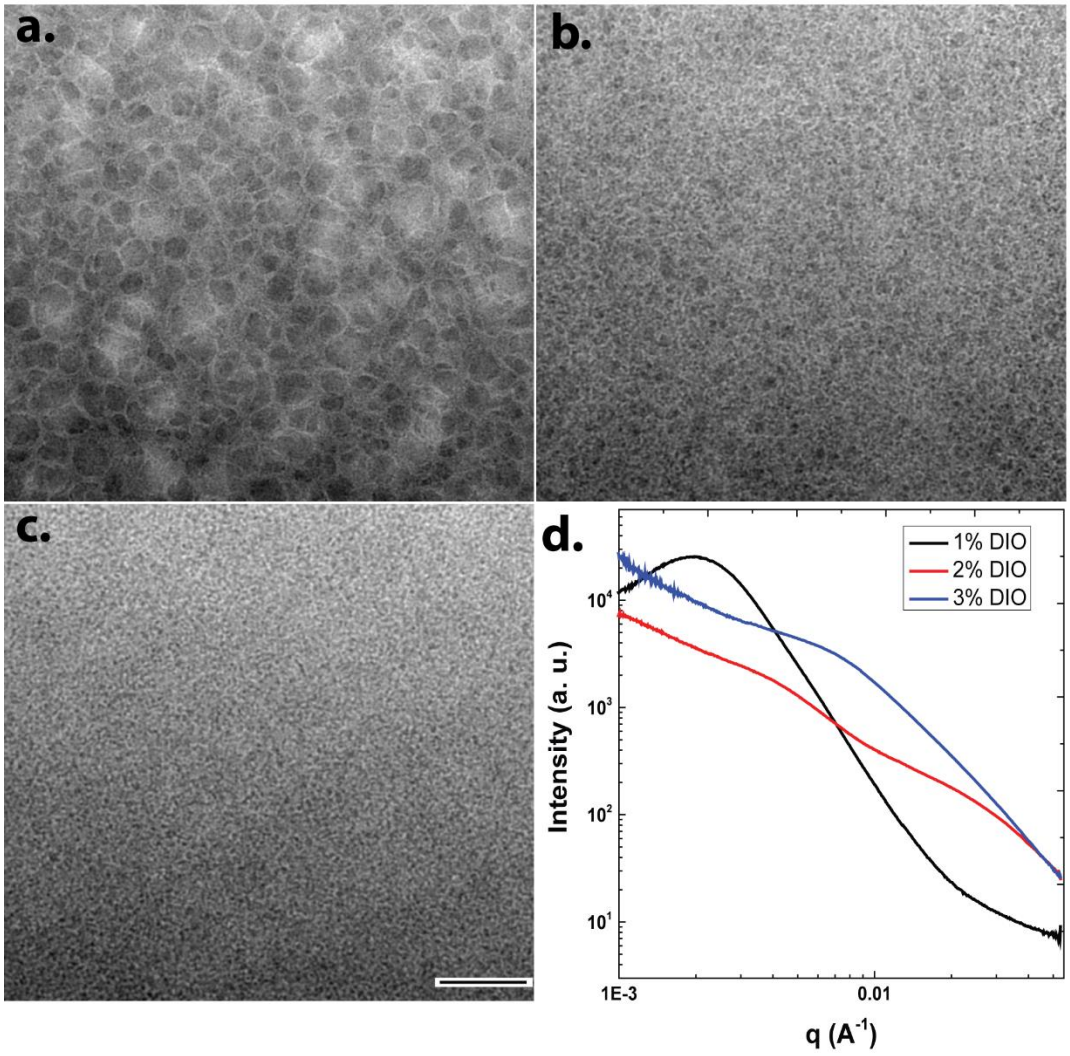

Figure 4.5 Bulk morphologies. Representative TEM images from a) 1% DIO, b) 2% DIO, and 3% DIO processed BHJ films. Scale bar is 500 nm. d) RSoXS profiles of the corresponding BHJ films.

The RSoXS results, together with the TEM micrographs, confirm the presence of a multi-length-scale morphology of the slot-die processed BHJs from both the 2% and the 3% DIO processed films, which is similar to previous observations from the spin-coated devices.[7,6] The smaller ~27-30 nm domain spacing is attributed to the inter-fibrillar regions as can be seen in the TEM micrographs and is primarily responsible for the

enhancement of device performance. The brighter regions are predominantly from the polymer-rich phase and the darker regions are from the $PC_{71}BM$-rich phase as also observed in the earlier chapters. We attribute the smaller fibril-to-fibril distance in the 3% DIO processed BHJ to be responsible for the improved FF over the 2% DIO sample (**Figure 4.5**). This is also evidenced by the larger R_{rec} for the 3% DIO film compared to the 2% DIO film, yielding a higher PCE than the 2% DIO processed film. This establishes the presence of a multi-length scale morphology for the optimized BHJ films processed from 3% DIO, which is a similar condition for the spin-coated PTB7/$PC_{71}BM$ devices. This is unlike the PDPPBT polymer system, studied in Chapter 2 and Chapter 3, where the optimized slot-die coated processing conditions differed from the optimized spin-coated processing conditions.

The focus of the subsequent sections of this chapter will aim to investigate the role of this initial 3% DIO on generating the optimal phase separation between PTB7 and $PC_{71}BM$ starting from the solution phase through the film solidification process to the final percolated morphology.

4.3.4 Understanding Influence of DIO during the Film Solidification Process

A combination of UV-Vis absorbance spectroscopy, grazing incidence wide angle X-ray diffraction (GIWAXD), and grazing incidence small angle X-ray scattering (GISAXS) methods were used to gain insight on the mechanism that dictates the film solidification process. Onset of polymer chain ordering was tracked from neat PTB7 with no solvent additive (PTB7/CB), neat PTB7 with solvent additive (PTB7/CB/DIO), as well as from

PTB7:$PC_{71}BM$ mixture with solvent additive (PTB7:$PC_{71}BM$/CB/DIO). From herein, PTB7:$PC_{71}BM$/CB/DIO system will be denoted as only BHJ/CB/DIO. 1% (w/v) solutions were prepared for the neat PTB7/CB and neat PTB7/CB/DIO systems, while a 2.5% (w/v) solution was prepared for the BHJ/CB/DIO system with the PTB7:$PC_{71}BM$ weight ratio of 1:1.5. It should be noted that a 2.5% (w/v) solution from only the neat polymer is not feasible for slot-die coating due to the very high viscosity of the polymer solution at that concentration. A 3% (v/v) DIO was added to the host solvent (CB) for the compositions that contained DIO additive, thus matching the optimized device preparation condition. For convenience, the solution concentration in w/v % is also given as w/w % in **Table 4.3**. For the scattering measurements, the mini slot-die coater was assembled with the scattering measurement systems at the Advanced Light Source at the Lawrence Berkeley National Laboratory, as described earlier in Chapter 3. Solutions were coated on Si/PEDOT:PSS substrates at 10 mm/s coating speed, and with approximately the same gap between the slot-die head and the substrate as in the device fabrication process. The X-ray scattering measurement routine was initiated immediately at the time of coating, thus enabling us to perform real time experiments to monitor the film solidification process from approximately time zero.

Table 4.3 Initial Solution Concentrations.

Solution	Concentration in w/v (%)	Concentration in w/w (%)
PTB7/CB	1%	0.90%
PTB7/CB/DIO	1%	0.88%
BHJ/CB/DIO	2.5%	2.17%

4.3.4.1 CB Evaporation and Polymer Structural Order

To better understand the effect of DIO during the film solidification process, it is imperative to study the development of polymer ordering first in the neat PTB7/CB only, without the presence of the solvent additive. The appearance of (100) domain spacing, corresponding to the separation distance between the main chain that are separated by the alkyl side chains, was used to identify the onset of polymer chain ordering as the solvent evaporates. **Figure 4.6** shows some representative snap shots of the 2D GIWAXS patterns during different times of the PTB7/CB drying process. The large isotropic halo in the 5 s pattern at q ~ 1.33 A^{-1} is characteristic of CB liquid scattering. For reference, the liquid scattering peaks at ~1.3 A^{-1} and ~1.5 A^{-1} from CB and DIO, respectively, are presented in **Figure 4.7**. As is evident in the 2D patterns and the corresponding in-plane (IP) line profiles in **Figure 4.6**, the majority of the CB evaporates within the first 25 seconds. The scattering profiles show no significant change after 30 s. Face-on orientation of the polymer chain is also evident from the 2D patterns after solvent removal, with the presence of a π-π stacking peak (010) in the out-of-plane (OOP) direction at q ~ 1.6 A^{-1} and the alkyl chain stacking peak (100) in the in-plane (IP) direction at q ~ 0.3 A^{-1}.

Initially, IP scattering in the q-range of 0.7 – 2.2 A^{-1} (**Figure 4.6**) is predominantly comprised of scattering contribution from CB. Contribution from the polymer content in this q-range is nominal as observed in the scattering profile of the dry film (after 30 s). Therefore, we aimed to estimate the residual CB content as a function of time from this q-range by subtracting the minimal polymer contribution (obtained from the dried film after 415 s) from the initial scattering profiles (5 s to 30 s elapsed time) as shown in **Figure**

4.8. No detectable CB scattering was observed after about 30 s indicating that CB evaporates in 30 s, which is in good agreement with the real time studies performed by Delongchamp *et. al.* for P3HT/PCBM system[19]. The further details on structural ordering of the PTB7 will be discussed in the later part of this chapter.

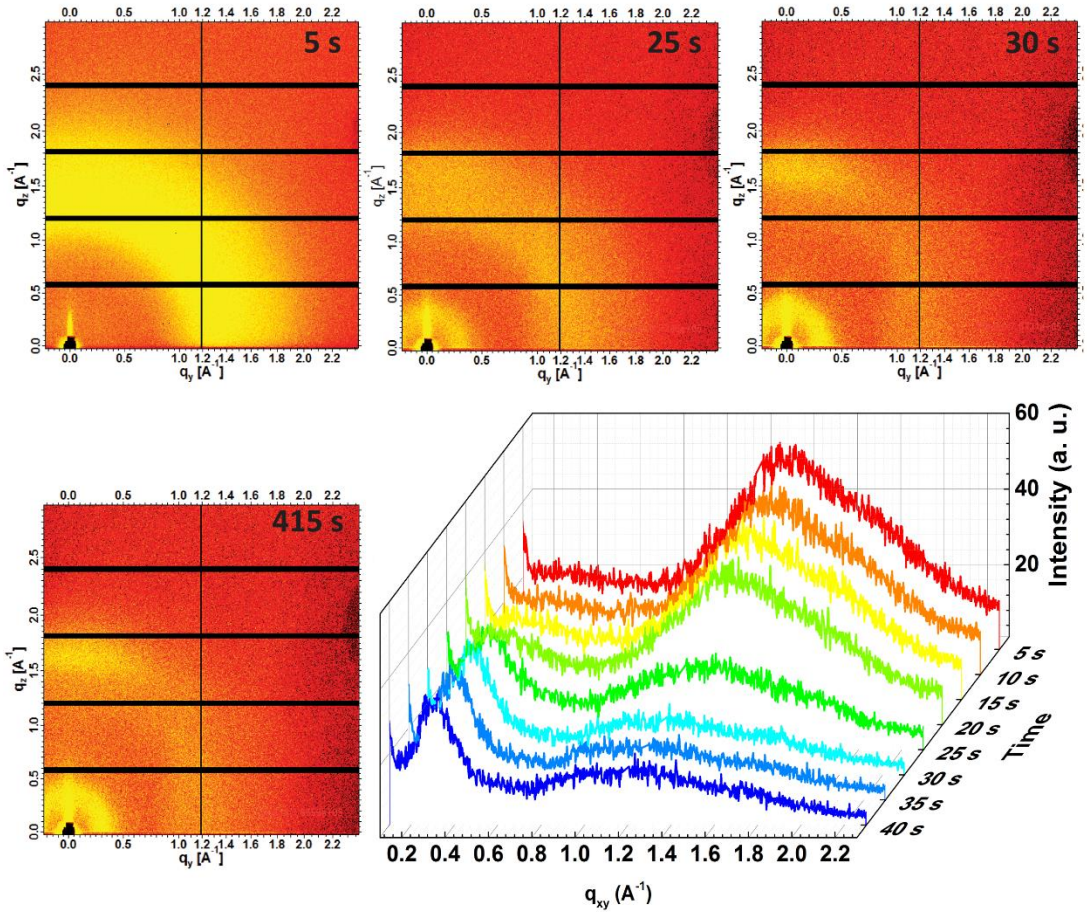

Figure 4.6 Some representative snap shots of 2D scattering patterns along with some initial scattering profiles from the neat PTB7/CB system.

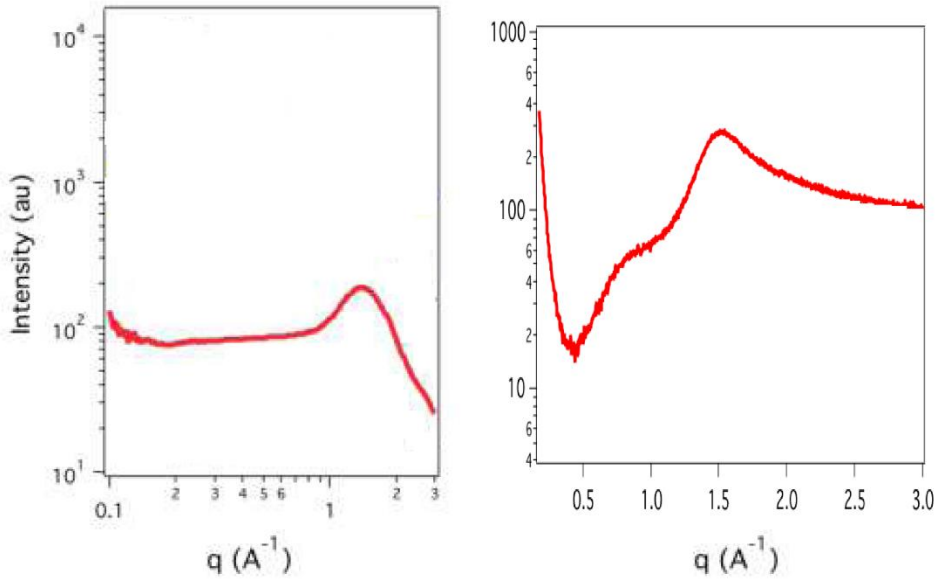

Figure 4.7 Solvent scattering peak of CB (left) and DIO (right)

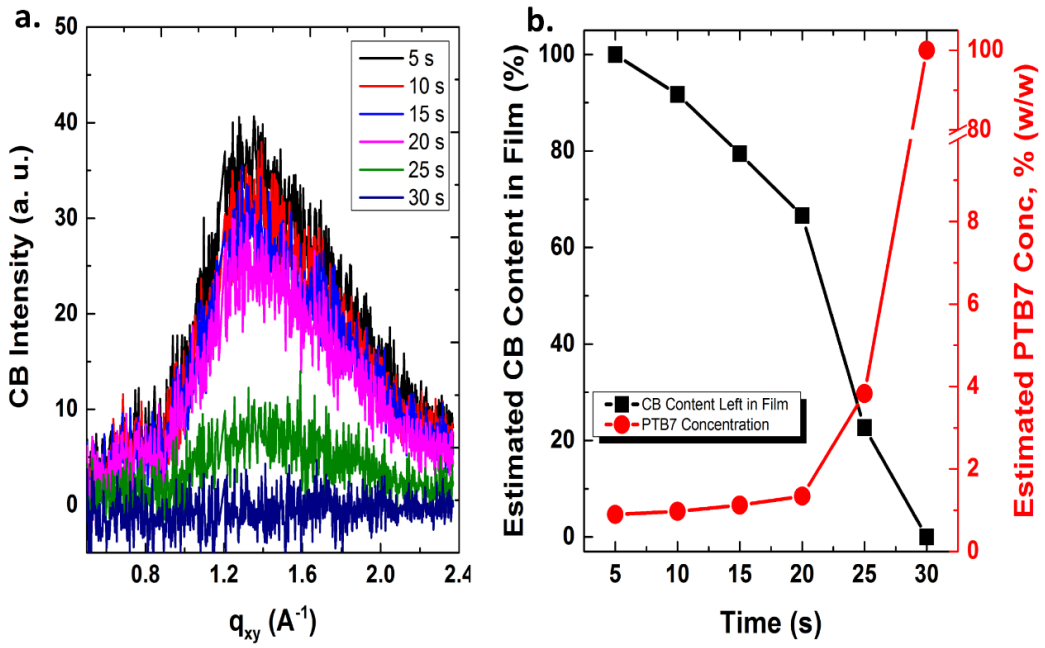

Figure 4.8 a) The reduction of CB intensity as a function of time after subtracting the minimal polymer scattering contribution (obtained from the final dried film) from the 5, 10, 15, 20, 25, and 30 s in-plane line profiles in the displayed q-range. b) Estimated CB content retained in the film and the estimated PTB7 content as a function of time.

4.3.4.2 DIO Evaporation and its Influence on Polymer Optical Order

Unlike CB, DIO has an extremely low vapor pressure (b. p. 167-169 °C at 6 mm Hg) which results in negligible evaporation at room temperature. It is necessary to apply vacuum or heat to remove DIO from the wet films. Due to the difficulty of estimating DIO content in the wet polymer film from the scattering measurements, we used UV-Vis absorption spectroscopy on the DIO containing wet films to determine the DIO removal rate at different stages of the drying process. This also allowed us to monitor the change in polymer aggregation behavior. PTB7/CB, PTB7/CB/DIO and BHJ/CB/DIO films were slot-die coated on quartz/PEDOT:PSS substrates. Each sample was then evacuated under vacuum for different amounts of time followed by immediate UV-Vis measurements. The absorption spectra of pure CB and pure DIO are shown in **Figure 4.9**. Both CB and DIO show peaks around ~192 nm, however, CB is expected to rapidly evaporate from the wet films (within ~30 s) as evidenced by the GIWAXD measurements and, therefore, not expected to overlap with the DIO peak in the UV-Vis measurement. The corresponding spectra from PTB7/CB, PTB7/CB/DIO, and BHJ/CB/DIO films are shown in **Figure 4.10**, where the left column displays data in the 180-300 nm range and the right column displays data in the 600-800 nm range. It should be noted that the elapsed time, immediately after coating and before the UV-Vis data acquisition, was approximately 2 min.

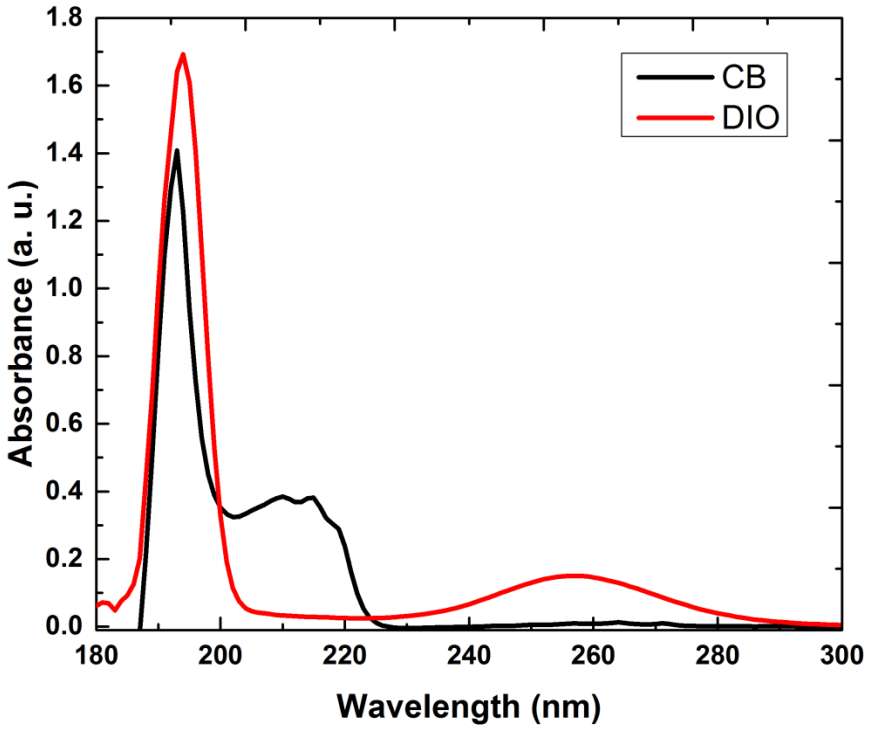

Figure 4.9 Absorbance Spectra of CB and DIO.

To ensure that the absorbance in the ~185-200 nm range for DIO containing compositions did not overlap with CB absorbance in the same wavelength range, we first examined the UV-Vis measurements from the PTB7/CB composition. As expected, no absorbance from CB was observed in this wavelength range (**Figure 4.10a**) confirming the complete removal of CB by the time absorption data were acquired. For the DIO containing compositions, a strong DIO peak was observed in the initial runs, which progressively decreased in intensity with longer evacuation time. It should be noted that BHJ/CB/DIO composition shows additional absorbance contribution in this wavelength range compared to the neat PTB7/CB/DIO composition, which is arising from the presence of $PC_{71}BM$ in the BHJ. Due to this overlap of DIO and $PC_{71}BM$ absorbance in the

initial runs for this BHJ/CB/DIO composition, we only used the neat PTB7/CB/DIO composition to estimate the residual DIO content as a function of time. Nonetheless, the trend of DIO removal time is similar for both cases as can be observed from the reductions of DIO peak intensity peaks.

Figure 4.11 shows that DIO removal is slow in the first couple of minutes of evacuation, then decreases significantly after a total evacuation time of 5 min. This is also similar for the BHJ composition as observed in **Figure 4.10c**. Due to the negligible evaporation of DIO at room temperature, the initial DIO absorption contribution, before any application of vacuum, will correspond to the ~3% (v/v) DIO concentration, as in the original solution composition. Within 5 min of evacuation, this significantly drops to 0.4% of the initial solution concentration, and then further decreases to 0.15% after 20 min of evacuation and to an undetectable amount after 30 min of evacuation. The corresponding PTB7 concentration (w/w) is also plotted in **Figure 4.11**, as well as the BHJ concentration in the BHJ/CB/DIO composition after complete CB removal. Combination of this UV-Vis results and the GIWAXD results on PTB7/CB described earlier, establishes the solvent removal rates for both DIO and CB, which will be used in the later sections of this chapter to evaluate the influence of DIO on the structural ordering of the PTB7 and the phase separation of PTB7 and $PC_{71}BM$.

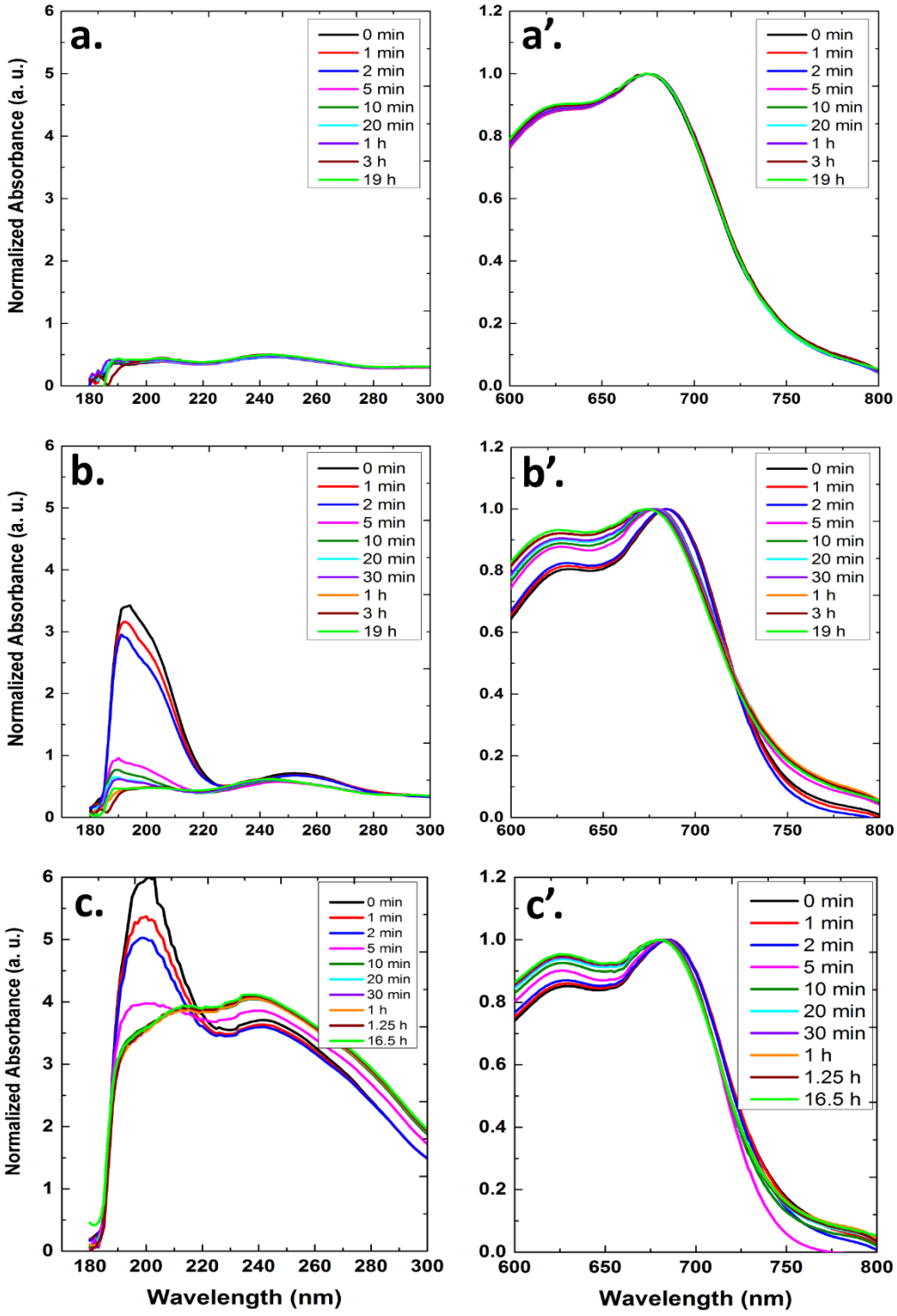

Figure 4.10 UV-Vis measurements of PTB7/CB (a, a'), PTB7/CB/DIO (b, b'), and BHJ/CB/DIO (c, c') compositions at different stages of the drying process.

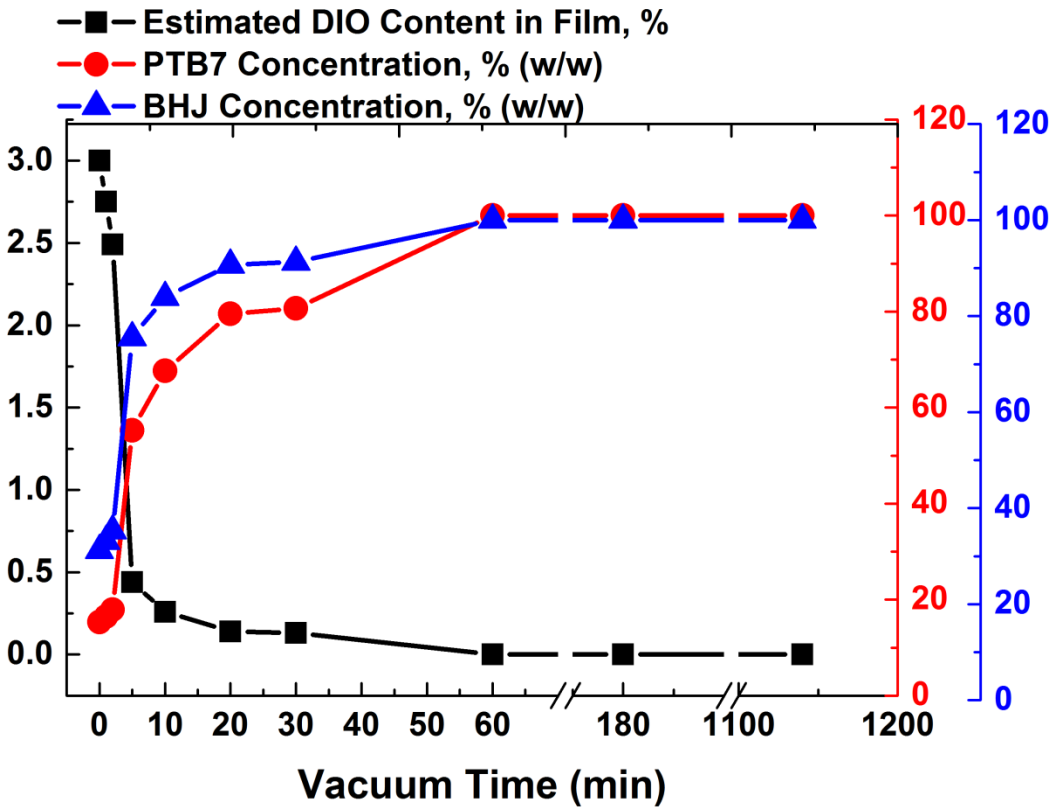

Figure 4.11 Estimated concentrations of DIO, PTB7, and BHJ contents as a function of vacuum time.

In addition to providing information on the removal of DIO, the UV-Vis absorbance spectra also provided an important information on the influence of DIO on the PTB7 aggregation states (**Figure 4.10a', b', c'**) in the wet films. For the PTB7/CB composition, there was no significant change in the polymer vibronic peaks at 675 nm and 624 nm, which are associated with (0-0) and (0-1) transitions, respectively, during the different stages of evacuation. This is due to the rapid removal of CB immediately after coating. Consequently, further evacuation shows no impact on the polymer aggregation.

Conversely in the PTB7/CB/DIO and BHJ/CB/DIO compositions, DIO does not evaporate without application of vacuum. The presence of this 3% DIO appears to impact the relative nature of PTB7 aggregation states (J-type vs. H-type). It is noteworthy that once the CB has evaporated, the remaining PTB7 and the BHJ contents are in a supersaturated condition. From **Figure 4.10 b'**, it is evident that the initial (0-0) vibronic peak at ~685 nm does not change up to 2 min of evacuation when the DIO content drops to ~2.5%. When the DIO content reaches ~0.4% after 5 min of evacuation (PTB7 concentration at this point is 55.3% w/w), the (0-0) peak interestingly blue shits to 679 nm, followed by further progressive blue shifts up to ~ 675 nm in the PTB7/CB/DIO system. Furthermore, the relative amount of the (0-1) vibronic transition (~624 nm) progressively increases as DIO is removed from the system. A similar trend was also observed for the BHJ/CB/DIO system (**Figure 4.10 c'**). Typically, relative blue shifts of the vibronic peaks, as well as relative increase in the (0-1)/(0-0) vibronic peak intensity ratios in polymeric semiconductors, point to an increased population of H-type aggregates.[20,21] This suggest that the PTB7 moieties remains in a more planar configuration in the presence of DIO, indicating that the polymer chains have relatively higher amount of J-type aggregates giving rise to more intra-chain excitonic coupling. On the other hand, as the DIO is removed, the population of H-type aggregates increases, giving rise to non-planarity in the polymer structure. We attribute this to the occurrence of possible backbone tilts in the polymer chains as DIO is removed from the system. In a recent theoretical study[22] on the crystal structure and optical properties of PTB7, it was also found that a different degree of backbone tilt occurs between the respective planes of thiophene moieties (benzodithiophene and thieno

thiophene) and the a-axis. Previous theoretical work from the same group has also identified similar backbone tilts in other thiophene based polymer semiconductors, such as P3HT[23] and PBTTT[24]. Thus, our results suggest the possibility of preferential interaction of DIO with PTB7 backbone even if it is a very poor solvent for this polymer.

4.3.4.3 Onset of PTB7 Diffraction Order from the Different Composition Systems

Initial scattering profiles from the PTB7/CB was briefly discussed in the last section to establish the CB and DIO removal times. Here, the onset and growth of PTB7 crystallization will be discussed in more detail as the host solvent and the solvent additive evaporates. **Figure 4.12** shows the time evolution of the IP and OOP scattering profiles for the three compositions: PTB7/CB, PTB7/CB/DIO, and BHJ/CB/DIO. The initial red profile corresponds to measurements after 5 s of coating for all cases. The last blue profiles correspond to measurements after 415 s of coating for PTB7/CB (**Figure 4.12a**), 950 s of coating for PTB7/CB/DIO (**Figure 4.12b**), and 955 s of coating for BHJ/CB/DIO (**Figure 4.12c**) compositions. It should be noted that the gap/increase in intensity from the intermediate line profile (yellow frames) in **Figure 4.12 b, c** are due to increasing the exposure time to 10 s from the initial 5 s frames for longer data acquisition time. The peak evolution of the (100) reflection in the IP direction and the (010) reflection in the OOP direction is clear for PTB7/CB system. The reduction of intensity at q ~ 1.3 A^{-1} in both IP and OOP directions corresponds to the CB evaporation (**Figure 4.12a**) as discussed earlier.

For PTB7/CB/DIO composition, the initial broad peak around 1.3-1.5 A^{-1} includes contributions from CB and DIO in the IP direction, and contributions from CB, DIO, and

possibly some contribution from PTB7 (010) stacking peak in the OOP direction. For BHJ/CB/DIO composition, the initial broad peak around 1.3-1.5 A^{-1} includes contributions from $PC_{71}BM$, CB, DIO in the IP direction, along with some possible contribution from PTB7 (010) stacking peak[25] in the OOP direction. Unlike **Figure 4.12a**, time evolution of both (100) and (010) reflections in IP and OOP directions, respectively, are not quite obvious in **Figure 4.12 b, c**, indicating that the presence of DIO is prohibiting polymer crystallization even though CB has evaporated, leaving the system in a saturated condition. For the remainder of the discussions, the IP (100) reflection will be of our primary concern.

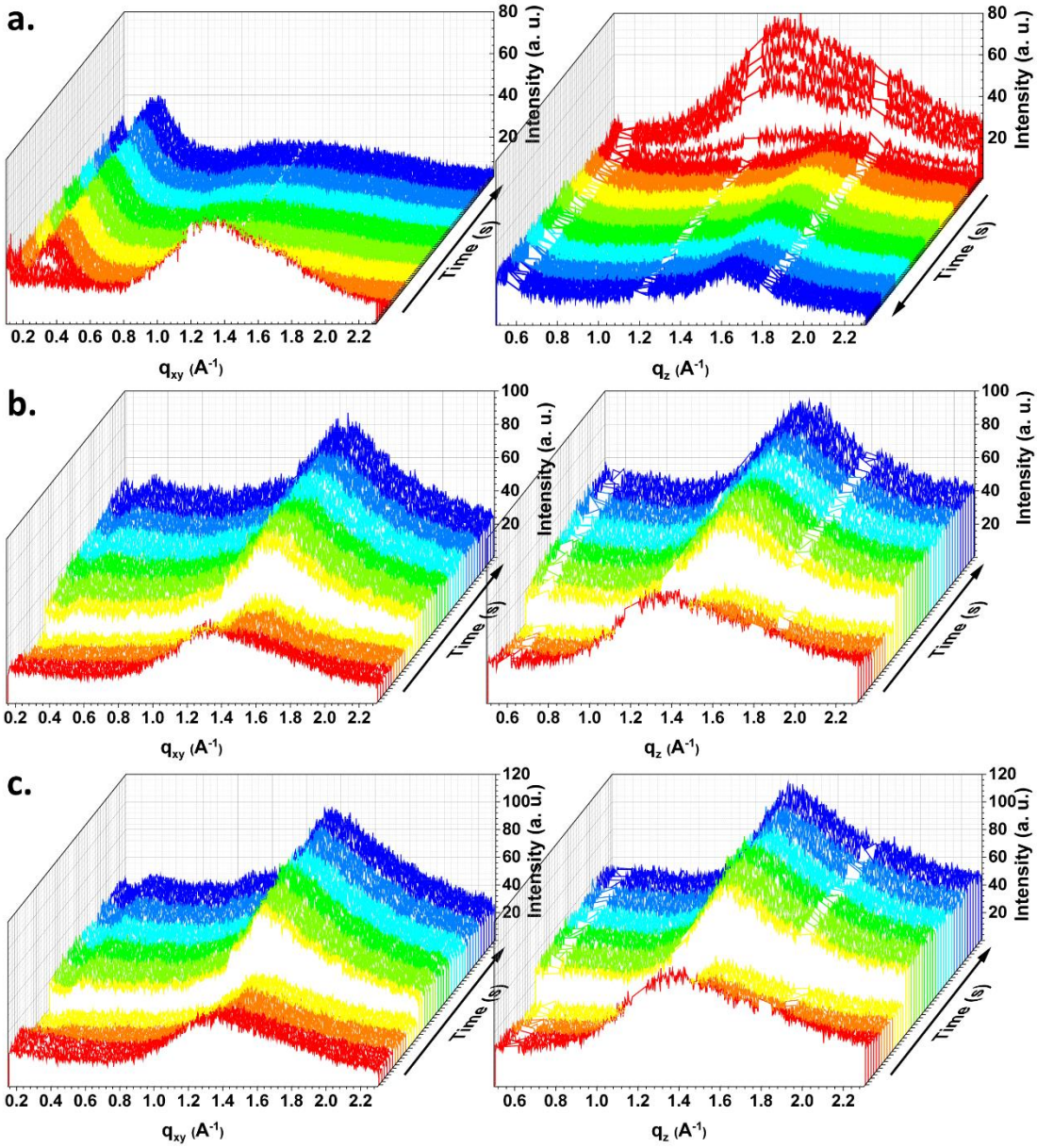

Figure 4.12 GIWAXD line profiles from a) PTB7/CB, b) PTB7/CB/DIO, and c) BHJ/CB/DIO. Left column represents the scattering profiles in the in-plane (IP) direction, and right column represents the scattering profiles in the out-of-plane (OOP) direction. In all cases, red profiles are the beginning of *in-situ* measurements and blue profiles are at the end of in-situ measurements.

The time evolution of parameters extracted from the (100) reflections are presented in **Figure 4.13**. The d-spacings were obtained from the corresponding Bragg

reflections at $q = \frac{2\pi}{d}$, while the coherence lengths of the crystals were calculated using the Scherrer equation, $D_{hkl} = 0.9 \times \frac{2\pi}{\Delta q}$, where Δq represents the full width at half maximum (FWHM) of the peak of interest. Furthermore, time evolution of the thickness changes are also presented in **Figure 4.13** for all three compositions. An interferometer with wavelength range of ~ 380 – 1100 nm and corresponding thickness range of 15 nm – 70 µm, was mounted with the *in-situ* scattering measurement set up to continuously monitor the thickness as the solvent evaporated at room temperature. Fitting was performed in the 850-1100 nm wavelength range, where the active material components have negligible absorbance. Initial thicknesses of the wet films were in the range of 8-10 µm, which then rapidly stabilized after about 20 seconds into the drying phase for all three compositions. This is attributed to the fast evaporation of the CB content as established in the last section. The measured *in-situ* thickness of the PTB7/CB after CB removal was ~80 nm, which was similar to the thickness measured by surface profilometer afterwards, indicating almost complete CB removal within ~30 s of coating. On the other hand, the measured *in-situ* thicknesses plateaued at ~340 nm and ~605 nm for PTB7/CB/DIO and BHJ/CB/DIO compositions, respectively. This larger thicknesses of the PTB7/CB/DIO and the BHJ/CB/DIO compositions, compared to the completely dried film thickness of ~80-100 nm, further confirms the continued presence of DIO before any application of vacuum.

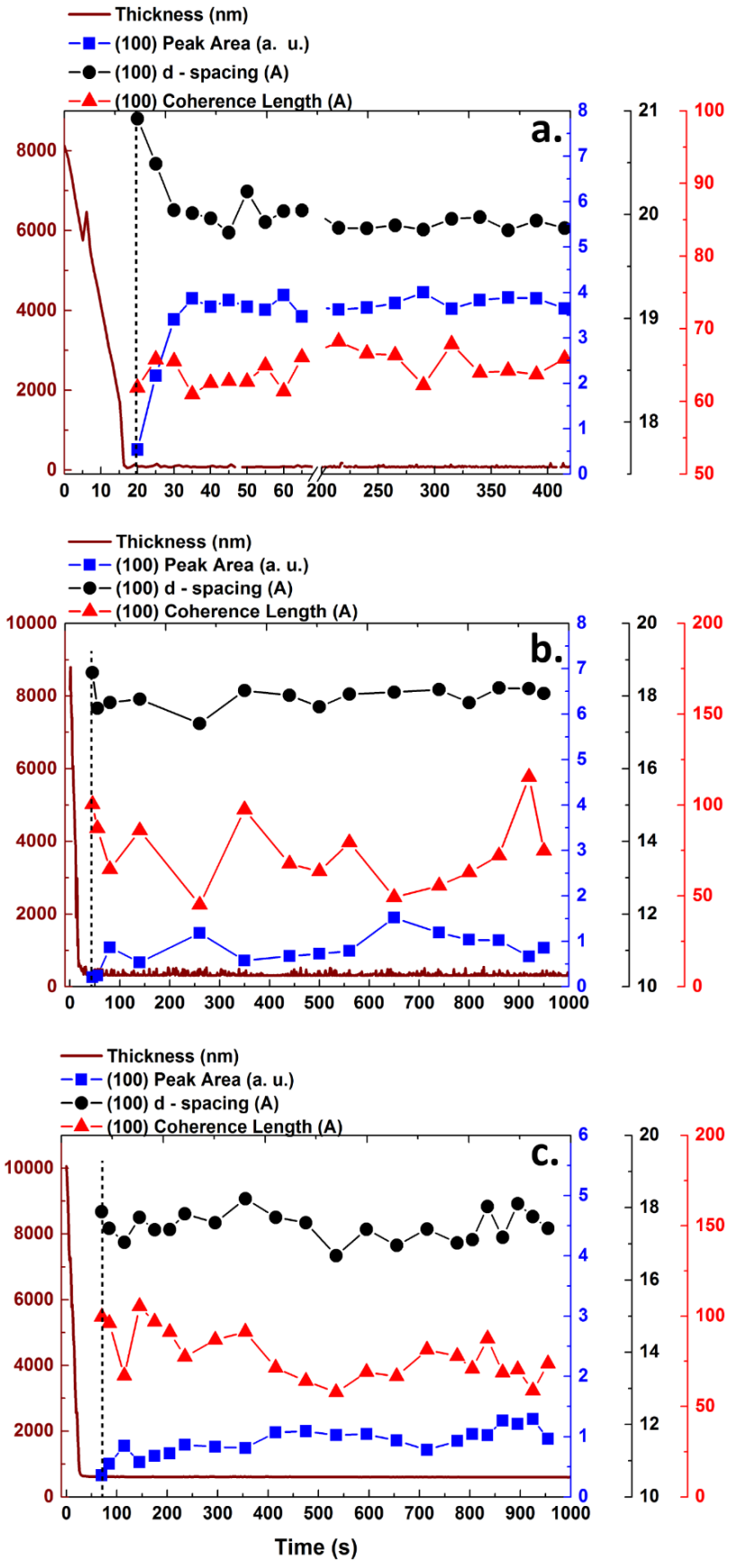
Thickness (nm)
(100) Peak Area (a. u.)
(100) d - spacing (A)
(100) Coherence Length (A)
a.
b.
c.
Time (s)

Figure 4.13 Changes in film thicknesses, (100) d-spacings, (100) peak areas, and (100) coherence lengths in the IP direction for a) PTB7/CB, b) PTB7/CB/SDIO, c) BHJ/CB/DIO compositions. The dashed lines indicate the times where the (100) reflection was first detected after coating.

From **Figure 4.13**, it is notable that the appearance of the (100) stacking peak shifted from ~20 s, to ~50 s, to ~70 s for PTB7/CB, PTB7/CB/DIO, and BHJ/CB/DIO compositions, respectively. During the drying process of the PTB7/CB composition as observed in **Figure 4.13a**, the appearance of polymer crystallization occurred when polymer concentration reached ~1.34% w/w (**Figure 4.8b**) from its initial solution concentration of 0.9% w/w (or, 1% w/v). This crystallization further increased when the polymer concentration increased to ~3.83% w/w after 25 s, and subsequently stabilized after 30 s when no further CB was detected, giving a polymer concentration of ~100% w/w. On the other hand, polymer and BHJ concentrations at the delayed appearance of the (100) peak in PTB7/CB/DIO and BHJ/CB/DIO compositions (**Figure 4.13b, c**) were ~15% and ~31% w/w as shown in **Figure 4.11**, respectively. No significant development of the (100) reflection was observed up to ~1000 s after coating in the cases where DIO was present. These results are in stark contrast with the PTB7/CB system, where the onset of polymer ordering was observed at a polymer concentration of only 1.34% w/w. Subsequently, DIO was evacuated from the wet PTB7/CB/DIO and BHJ/CB/DIO compositions for different durations, as in the optical measurements, followed by successive GIWAXD measurements. The resulting parameters from the (100) reflections are presented in **Figure 4.14**. No significant increase in the (100) peak area was observed up to a polymer (BHJ) concentration of ~55% (~75%) w/w (evacuation time of 5 min). It is

evident that at least 20 min of vacuum time was necessary to observe a significant enhancement in the (100) peak areas for the DIO containing compositions with both the neat PTB7 and the BHJ films. This corresponds to a PTB7 (BHJ) concentration of ~80% (~90%) w/w after 20 min of evacuation. Comparison of our optical measurements (**Figure 10 b', c'**) with the scattering measurements confirms the fact that the optical order precedes the diffraction order in these systems, which is similar to the earlier observations for P3HT system[19].

The final coherence lengths in the (100) direction are 65 Å, 68 Å, and 60 Å obtained from the dried films from the PTB7/CB, PTB7/CB/DIO, and BHJ/CB/DIO, respectively. The change in (100) d-spacing of the PTB7 as a function of solvent evaporation time is rather interesting. For the neat PTB7, d-spacing slightly drops from ~21 Å to ~20 Å (**Figure 4.13a**) as the solvent evaporates in the additive free composition (PTB7/CB). However, it increases slightly from the initial spacing of ~18 Å to ~19.5 Å (**Figure 4.14a**), as the solvent additive evaporates from the PTB7/CB/DIO system. In the case of BHJ/CB/DIO, the trend is similar to that for PTB7/CB. Here, the d-spacing decreases slightly from ~18 Å to ~17 Å (**Figure 4.14b**). In general, this smaller d-spacing in this BHJ film, compared to the neat polymer films, is in agreement with the *ex-situ* scattering measurements reported by Darling *et al*.[6]. This lower d-spacing in the BHJ points to an enhanced side chain interdigitation in the BHJ film when $PC_{71}BM$ is present. From the trend in d-spacing changes in the neat polymer systems, with and without the solvent additive, it is clear that initially DIO is interacting with the PTB7 side chains by retaining the side chains in a more relaxed state, hence the lower initial d-spacing in PTB7/CB/DIO. Subsequently, this

increases as DIO is removed from the system, causing the side chain to stretch and increase the d-spacing. On the other hand when additive is not present, the polymer chains are most likely farther apart from each other, separated by the CB host solvent molecule. Hence a larger d-spacing was observed initially that subsequently decreased as CB evaporated from the system. It is important to mention that the final d-spacing after complete removal of the solvents (CB or CB/DIO) is about the same for both CB and CB/DIO (20 Å vs. 19.5 Å) processed films. Finally, in the wet BHJ/CB/DIO film, the initial d-spacing is also ~18 Å similar to initial d-spacing in the neat PTB7/CB/DIO system. In this case, however, DIO is not only retaining the PTB7 side chains in a more relaxed state, it is also keeping the $PC_{71}BM$ solubilized. As film solidification progresses with DIO removal, the reduction in d-spacing points to an enhanced side-chain interdigitation, presumably due to constraints on the polymer chain by the presence of $PC_{71}BM$. These *in-situ* scattering results combined with the *ex-situ* scattering measurements on the vacuum dried samples, as well as the optical results discussed earlier, strongly suggest that DIO prevents the development of PTB7 crystallization even at extremely high concentrations which are certainly above the PTB7 solubility threshold in DIO, and keeps the polymer and the BHJs at swelling states.

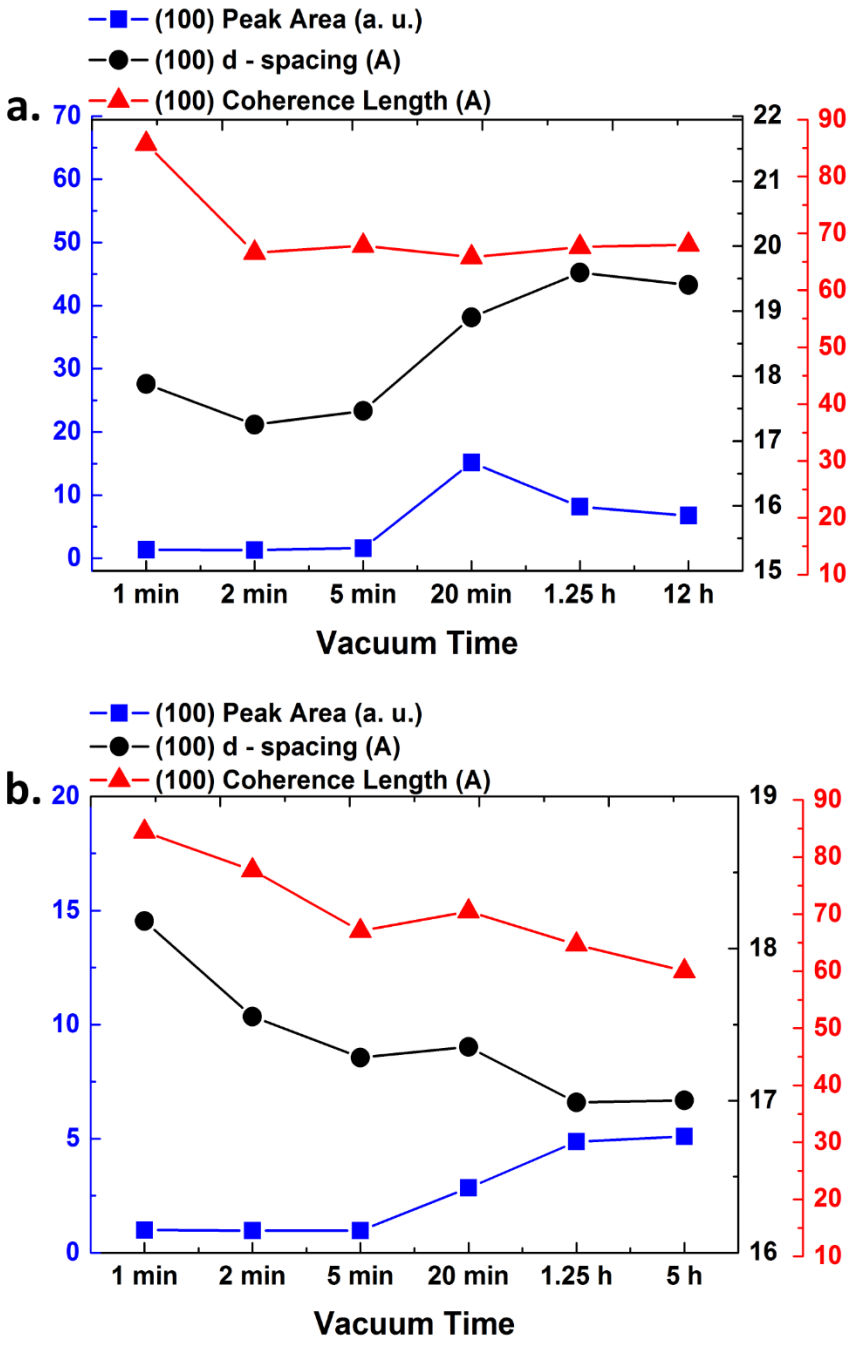

Figure 4.14 Changes in PTB7 (100) peak areas, d-spacings, and coherence lengths after applying vacuum for different times for a) PTB7/CB/DIO, and b) BHJ/CB/DIO systems.

4.3.4.4 Onset of PTB7/$PC_{71}BM$ Phase Separation

To determine the onset of lateral phase separation between PTB7 and $PC_{71}BM$, grazing incidence small angle X-ray scattering (GISAXS) measurements were performed on the BHJ/CB/DIO. Some representative snap shots of the 2D GISAXS scattering patterns are shown in **Figure 4.15**. The top panel represents scattering patterns at different times after coating, but before applying any vacuum for DIO removal. It is clear that no apparent phase separation occurs when DIO is present before evacuation. The bottom panel represents scattering patterns of the same film, but after different evacuation times for DIO removal. The corresponding 1D line profiles are shown in **Figure 4.16**. The monotonic decrease in intensities of the scattering profiles up to 10 min of evacuation time suggests that no well-defined phase separated morphology is observed in this q-range when the BHJ concentration reaches ~84% w/w. It should be noted that a larger scale of phase separation (smaller q regions) may exist at this point, however, not visible due to the limitation in this experimental q-range and resolution. As the BHJ concentration reaches ~90% w/w after 20 min of evacuation time, a broad reflection appears around 0.008 – 0.03 $Å^{-1}$ range, which corresponds to a center-to-center domain spacing in the range of 21 - 78 nm. This domain spacing is consistent with the TEM and RSoXS results obtained from the 3% DIO processed film, as seen in **Figure 4.5 c, d**. Furthermore, additional evacuation time does not lead to any significant changes in the domain spacing, as evidenced by the shape of the scattering profiles (**Figure 4.16**).

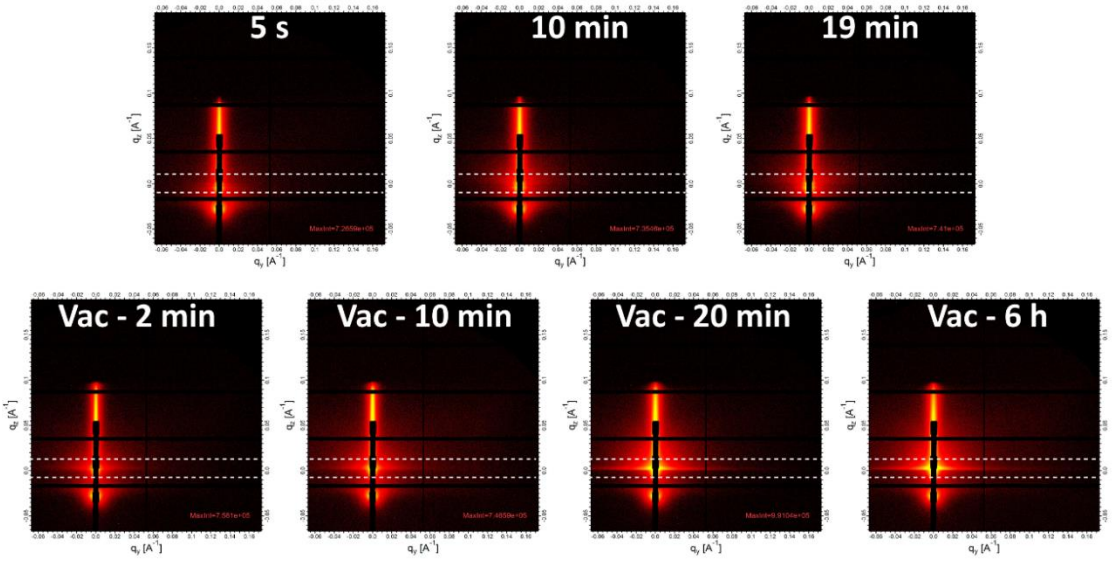

Figure 4.15 2D GISAXS patterns before any evacuation (top panel), and after different evacuation durations of DIO removal (bottom panel). The areas between the dashed lines represent the regions of interest for the scattering intensities.

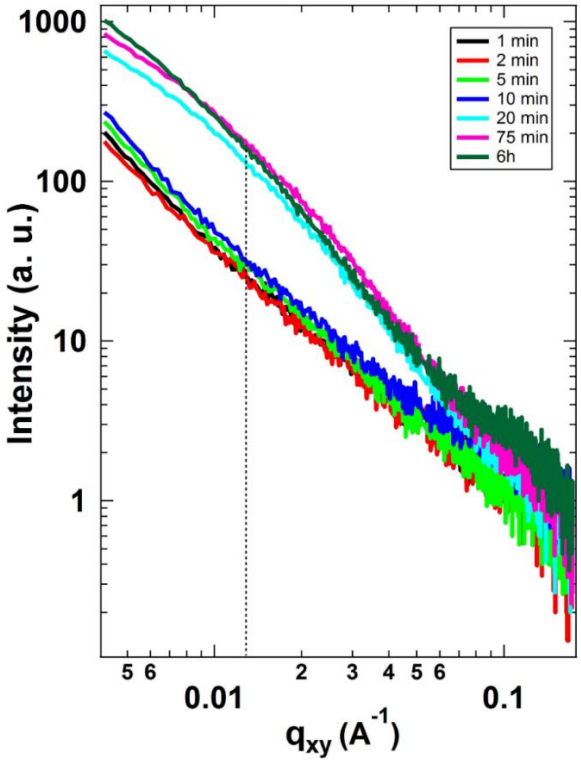

Figure 4.16 1D line profiles obtained from the 2D GISAXS patterns in the horizontal directions.

4.3.4.5 Origin of the Favorable Interaction between DIO and PTB7

So far, the optical results where DIO was seen to retain the polymer chains in a more planar configuration and the scattering results where DIO was seen to delay and prevent further development of polymer crystallization until the concentrations approached far beyond the solubility limit, indicate that DIO is preferentially interacting with the polymer chains in the wet films. It is, therefore, imperative to understand the solution properties of these systems in order to obtain a clear insight on the influence of DIO during the nanostructure morphology formation. In a recent study by Yu and coworkers, a substantial local dipole moment was found to be present in the PTB7 chain through the BDT to TT moiety. An average dipole moment of 7.06 D was calculated for 4 repeat units and the number is expected to increase as the length of the polymer chain increases.[26] For the case of DIO, it is expected to bear a net dipole moment of 0 D due to its symmetric structure. Inspired by this PTB7 dipole moment result, we performed a series of solution dielectric constant measurements since dipole moments and polarizabilities of materials are directly related to their dielectric constants. Dielectric constant measurements have also proven to be extremely beneficial to investigate the solution properties of various polymer systems[27–29].

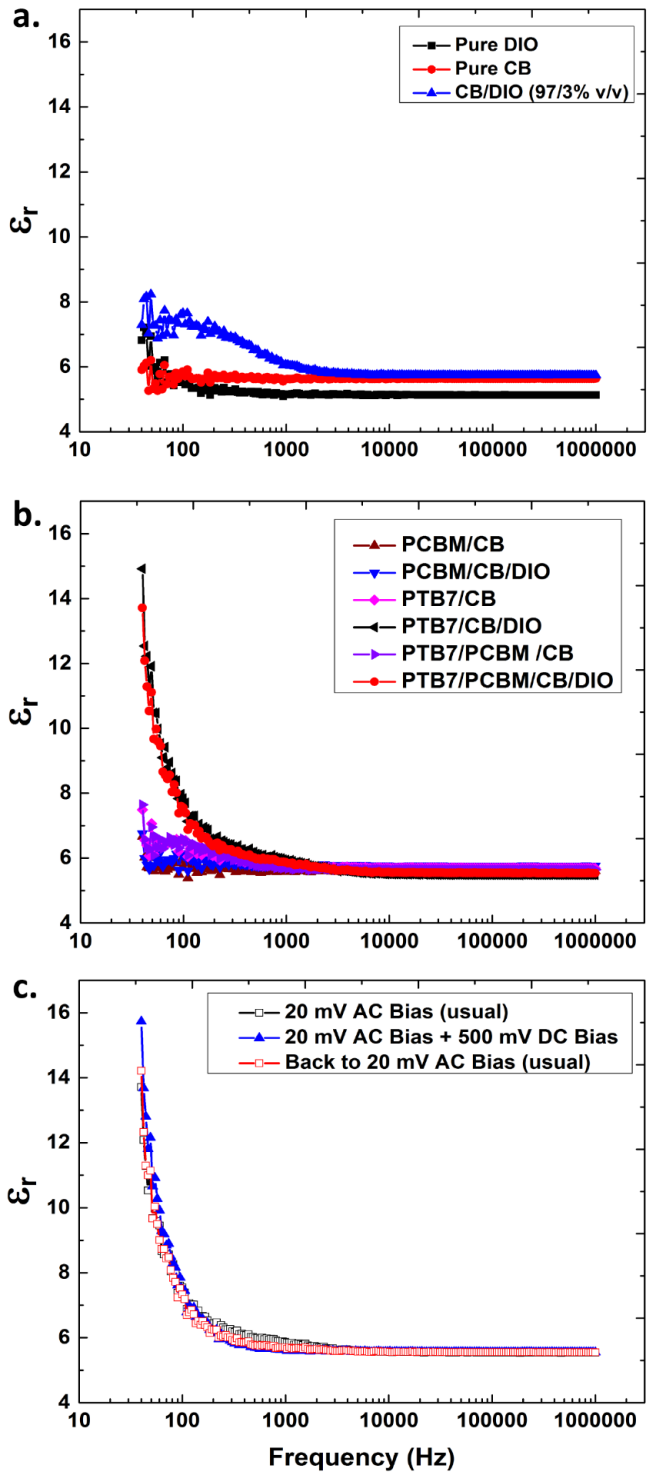

Figure 4.17 Relative dielectric constants vs frequency measurements for a) pure and mixed solvets, b) solutions from all the relevant compositions, and c) PTB7/PCBM/CB/DIO solution with and without a 500 mV DC bias.

For this experiment, first, the solution capacitance was measured at 25 ℃ in the frequency range of 40 Hz – 1 MHz, using a four probe parallel plate capacitor set up with a 300 µm separation gap. An AC bias of 20 mV was used for the mentioned frequency range, and no DC bias was applied unless otherwise indicated. The relative dielectric constants ($€_r$) were then calculated from these capacitance measurements and the resulting dielectric relaxation plots are provided in **Figure 4.17**. Pure CB gave a $€_r$ value close to 6 in the low frequency region (quasi static), which is similar to the reported static $€_r$ value of chlorobenzene[30]. Interestingly, when 3% (v/v) DIO was added to CB, $€_r$ increased to ~7.5 in this low frequency region, which is more than likely, an indication of induced dipole moments on DIO in the presence of CB under the electric field generated by the 20 mV oscillation bias (**Figure 4.17 a**). For comparisons, **Figure 4.17 b** shows data from all relevant solutions for this study, namely: $PC_{71}BM$ /CB, $PC_{71}BM$ /CB/DIO, PTB7/CB, PTB7/CB/DIO, BHJ(PTB7 + $PC_{71}BM$)/CB, and BHJ(PTB7+ $PC_{71}BM$)/CB/DIO. There was no significant change in $€_r$ for the neat $PC_{71}BM$ solutions regardless of the presence or absence of DIO, giving a $€_r$ value of ~6 for both cases. Comparing this to the pure CB/DIO value of ~7.5, suggests that the presence of $PC_{71}BM$ molecules most probably disrupts the small induced dipole on DIO previously imposed by the presence of CB. The $€_r$ values for the PTB7 and the BHJ (PTB7+PCBM) solutions from only CB, were also very similar to each other, although slightly higher than the neat $PC_{71}BM$ solutions. We attribute this small increase in $€_r$ in the PTB7/CB and BHJ/CB solutions (**Figure 4.17 b**) compared with the neat $PC_{71}BM$ solutions to the presence of electronegative fluorine atoms in the polymer chains.

What is more interesting is the dramatic increase of ϵ_r in the low frequency regions for the PTB7/CB/DIO and the PTB7/$PC_{71}BM$/CB/DIO solutions compared to the rest of the compositions. In **Figure 4.17 c**, 500 mV DC bias was applied to the same PTB7/ $PC_{71}BM$ /CB/DIO solution to determine whether the polarization increases with increasing electric field strength. The result shows no significant difference compared to the 0 DC applied bias measurements. We note that the application of 500 mV DC bias will not be able to cause an extremely large electric field in the system, however, it is certainly larger than the electric field imposed by only the 20 mV oscillation bias. This illustrates that, only when both the PTB7 and the DIO are simultaneously present in solutions, the polarization of the system increases significantly, which strongly suggests that DIO is preferentially interacting with the polymer chains most likely by induced dipole-induced dipole interactions. Due to the electronegative fluorine atoms and the resulting dipole moments in PTB7, we expect the BDT moiety to be partially positive while the TT moiety to be partially negative. When DIO is added in this composition, the partially negative Iodine sides in DIO are likely to interact with the partially positive BDT sides of the polymer. This is schematically illustrated in **Figure 4.18**.

This uncovers the nature of interaction of DIO with PTB7 chains in the solution phase. Due to this favorable interaction between DIO and PTB7 in the solution state, DIO is not expected to increase the polymer aggregate size in solutions even though technically it is a poor solvent for the polymer. This is in good agreement with the results of Chen and Marks groups where DIO was found to cause no significant increase in polymer aggregate size measured by transmission small angle X-ray scatterings of

polymer or BHJ solutions with and without DIO.[25] Their results also show a reduction of $PC_{71}BM$ aggregates in the solution phase upon addition of DIO. They hypothesized that iodine atom bears a partial negative charge and $PC_{71}BM$ is electro-deficient, and hence the relatively strong interactions between DIO and $PC_{71}BM$ which may be causing the enhanced $PC_{71}BM$ solubility into DIO. From our preliminary results of the dielectric measurements, we propose that DIO is rather interacting strongly with the PTB7 moieties, instead of $PC_{71}BM$. However, the reduction of $PC_{71}BM$ aggregate size in solution may simply be due to the good solubility between DIO and $PC_{71}BM$.

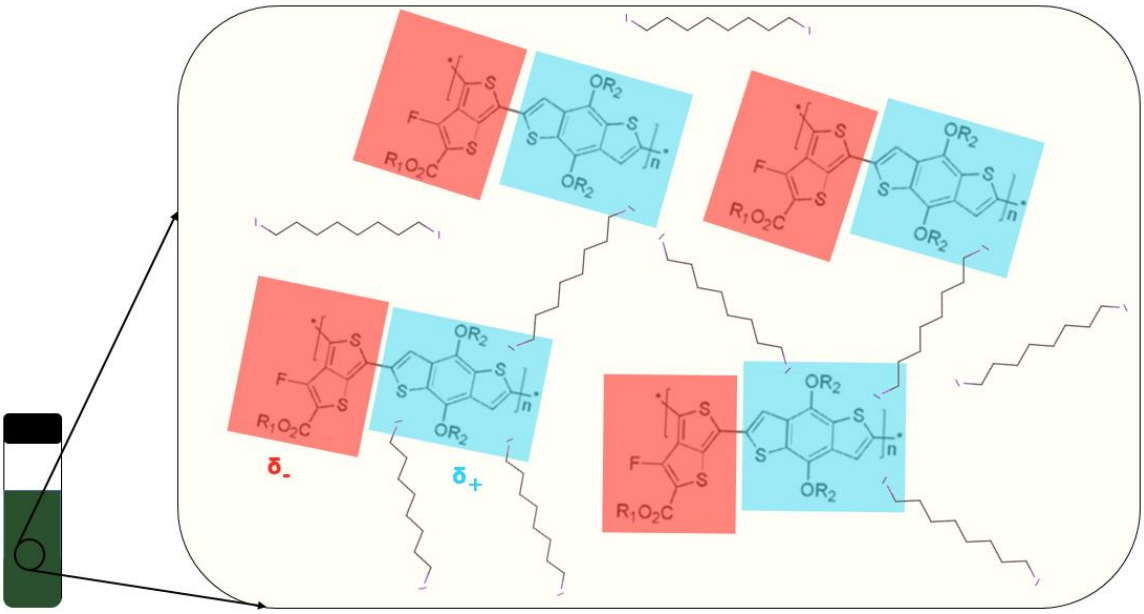

Figure 4.18 Schematic showing induced dipole – induced dipole interactions between DIO and PTB7 in solution phase.

4.3.5 Proposed Mechanism

The combined results lead to the conclusion that optical aggregations precedes intermolecular structural aggregations. Furthermore, we propose that DIO preferentially

interacts with PTB7 from the solution phase, possibly via the induced dipole-induced dipole interactions. Such preferential interactions between DIO and PTB7 chains persist throughout the film solidification process, thus prohibiting PTB7 to crystallize until most DIO evaporates as observed from the scattering measurements. The same applies for the BHJ drying film. This is schematically represented in the bottom row of **Figure 4.19**. Moreover, for the BHJ film, the enhancement of polymer (100) reflections in GIWAXD, as well as the appearance of a broad reflection from the center-to-center domain spacing in GISAXS occur at similar time indicating that polymer ordering and phase separation occur almost simultaneously. During the wet stage, DIO will keep the polymer chains separated from each other, while also retaining the $PC_{71}BM$. As DIO is almost completely removed, $PC_{71}BM$ contents will then settle between the chains thus reducing the degree of overall PTB7 crystallization. This proposed mechanism is schematically shown in **Figure 4.19** for all three compositions studied.

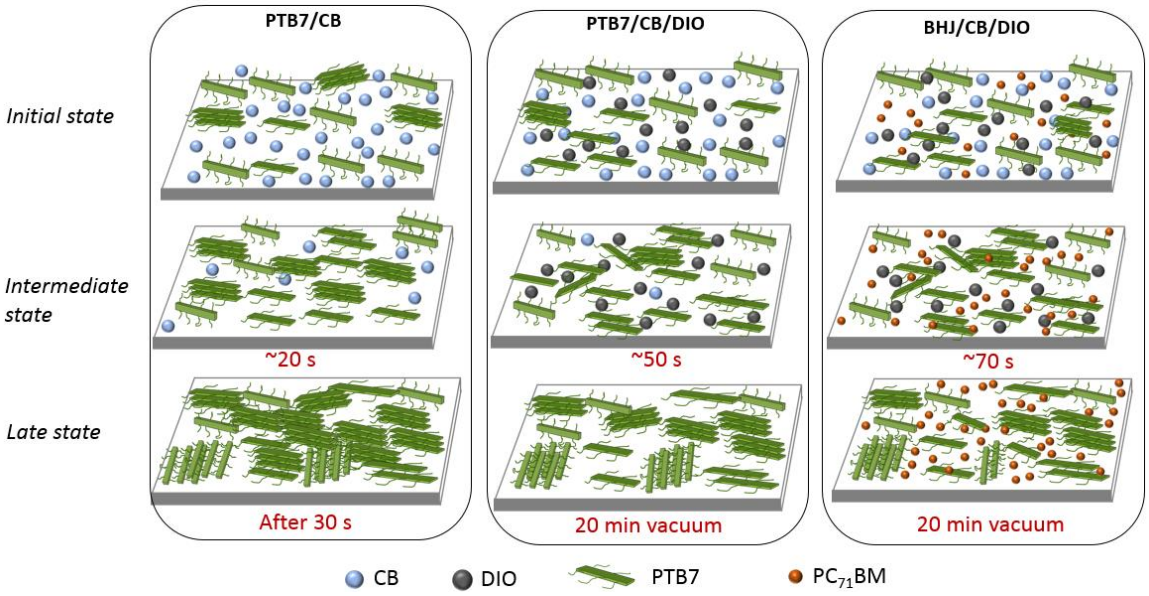

Figure 4.19 Proposed mechanism of the morphology evolution process in PTB7/CB, PTB7/CB/DIO, and BHJ/CB/DIO compositions. All active layer components remain well solubilized in the initial state. As CB mostly evaporates in the intermediate state, polymer crystallization is observed only in the PTB7/CB composition, however, crystallization is prevented by the preferential interactions between DIO and PTB7 in PTB7/CB/DIO and BHJ/CB/DIO compositions, even at supersaturated conditions. PTB7 crystallization is observed in these later two compositions once almost all DIO is removed such that not enough DIO-PTB7 induced dipole-induced dipole interactions can persist.

4.4 Conclusion

In summary, a comprehensive study was carried out to obtain a deeper understanding of the interplay between DIO, PTB7, and $PC_{71}BM$. An 8% efficiency device from PTB7/$PC_{71}BM$ system was successfully achieved using the mini slot-die coater developed in our lab. The optimized device showed a larger recombination resistance, and a smaller carrier transport resistance which was well correlated with the final morphology. Although, DIO is a poor solvent for PTB7, the combined *ex-situ* and *in-situ* results from optical and scattering experiments indicate the presence of a strong interaction between DIO and PTB7 polymer chains, even at supersaturated conditions.

This was further confirmed by dielectric constant measurements of PTB7 and PTB7/$PC_{71}BM$ blend in the solution phase with and without DIO, suggesting the presence of a significant induced dipole-induced dipole type interaction between DIO and PTB7. These results provide new insights about the role of DIO for the PTB7/$PC_{71}BM$ system which can provide further guidance in the materials design and processing of new high efficiency polymer solar cells.

4.5 References

[1] M. M. Wienk, M. Turbiez, J. Gilot, R. A. J. Janssen, *Adv. Mater.* **2008**, *20*, 2556.

[2] J. Peet, J. Y. Kim, N. E. Coates, W. L. Ma, D. Moses, a J. Heeger, G. C. Bazan, *Nat. Mater.* **2007**, *6*, 497.

[3] Y. Gu, C. Wang, T. P. Russell, *Adv. Energy Mater.* **2012**, *2*, 683.

[4] Y. Liang, Z. Xu, J. Xia, S. T. Tsai, Y. Wu, G. Li, C. Ray, L. Yu, *Adv. Energy Mater.* **2010**, *22*, 135.

[5] B. Collins, Z. Li, J. R. Tumbleston, E. Gann, C. R. Mcneill, H. Ade, *Adv. Energy Mater.* **2013**, *3*, 65.

[6] W. Chen, T. Xu, F. He, W. Wang, C. Wang, J. Strzalka, Y. Liu, J. Wen, D. J. Miller, J. Chen, O. K. Hong, O. L. Yu, S. B. Darling, *Nano Lett.* **2011**, *11*, 3707.

[7] F. Liu, W. Zhao, J. R. Tumbleston, C. Wang, Y. Gu, D. Wang, A. L. Briseno, H. Ade, T. P. Russell, *Adv. Energy Mater.* **2014**, *4*, 1301377 doi: 10.1002/aenm.201301377.

[8] G. J. Hedley, A. J. Ward, A. Alekseev, C. T. Howells, E. R. Martins, L. a Serrano, G. Cooke, A. Ruseckas, I. D. W. Samuel, *Nat. Commun.* **2013**, *4*, DOI: 10.1038/ncomms3867.

[9] D. Wang, F. Liu, N. Yagihashi, M. Nakaya, S. Ferdous, X. Liang, A. Muramatsu, K. Nakajima, T. P. Russell, *Nano Lett.* **2014**, *14*, 5727.

[10] G. J. Hedley, A. J. Ward, A. Alekseev, C. T. Howells, E. R. Martins, L. a Serrano, G. Cooke, A. Ruseckas, I. D. W. Samuel, *Nat. Commun.* **2013**, *4*, 2867.

[11] S. Ferdous, F. Liu, D. Wang, T. P. Russell, *Adv. Energy Mater.* **2014**, *4*, DOI: 10.1002/aenm.201300834.

[12] F. Liu, S. Ferdous, E. Schaible, A. Hexamer, M. Church, X. Ding, C. Wang, T. Russell, *Adv. Mater.* **2014**, *27*, 886.

[13] G. Garcia-Belmonte, A. Guerrero, J. Bisquert, *J. Phys. Chem. Lett.* **2013**, *4*, 877.

[14] L. Xu, Y.-J. Lee, J. W. P. Hsu, *Appl. Phys. Lett.* **2014**, *105*, 123904.

[15] B. Yang, Y. Yuan, J. Huang, *J. Phys. Chem. C* **2014**, *118*, 5196.

[16] A. Guerrero, N. F. Montcada, J. Ajuria, I. Etxebarria, R. Pacios, G. Garcia-Belmonte, E. Palomares, *J. Mater. Chem. A* **2013**, *1*, 12345.

[17] G. Perrier, R. De Bettignies, S. Berson, N. Lemaître, S. Guillerez, *Sol. Energy Mater. Sol. Cells* **2012**, *101*, 210.

[18] J. Kniepert, I. Lange, J. Heidbrink, J. Kurpiers, T. J. K. Brenner, L. J. A. Koster, D. Neher, *J. Phys. Chem. C* **2015**, *119*, 8310.

[19] N. Shin, L. J. Richter, A. a. Herzing, R. J. Kline, D. M. DeLongchamp, *Adv. Energy Mater.* **2013**, *3*, 938.

[20] F. C. Spano, C. Silva, *Annu. Rev. Phys. Chem.* **2014**, *65*, 477.

[21] M. D. Barnes, M. Baghar, *J. Polym. Sci. Part B Polym. Phys.* **2012**, *50*, 1121.

[22] L.-H. Li, O. Y. Kontsevoi, A. J. Freeman, *Phys. Rev. B* **2014**, *90*, 1.

[23] T. Tsumuraya, J.-H. Song, A. Freeman, *Phys. Rev. B* **2012**, *86*, 075114.

[24] L. H. Li, O. Y. Kontsevoi, S. H. Rhim, A. J. Freeman, *J. Chem. Phys.* **2013**, *138*, 164503.

[25] S. J. Lou, J. M. Szarko, T. Xu, L. Yu, T. J. Marks, L. X. Chen, *J. Am. Chem. Soc.* **2011**, *133*, 20661.

[26] B. Carsten, J. M. Szarko, H. J. Son, W. Wang, L. Lu, F. He, B. S. Rolczynski, S. J. Lou, L. X. Chen, L. Yu, *J. Am. Chem. Soc.* **2011**, *133*, 20468.

[27] R. J. Sengwa, S. Sankhla, *J. Macromol. Sci. Part B* **2007**, *46*, 717.

[28] A. V. Sarode, A. C. Kumbharkhane, *Polym. Int.* **2012**, *61*, 609.

[29] U. Kaatze, 0 Gottmann, R. Podbielski, R. Pottel, U. Terveer, *J. Phys. Chem.* **1978**, *82*, 112.

[30] A. Maryott, E. Smith, *Table of Dielectric Constants of Pure Liquids*, **1951**.

CHAPTER 5

CONCLUSIONS AND FUTURE WORKS

5.1 Conclusions

5.1.1 Role of Solvent Additives on PDPPBT-Based LBG Polymer Photovoltaics

Optimal active layer morphology is strongly dependent on processing conditions such as thermal annealing, solvent annealing, and solvent-additives. Recently, solvent-additive based processing method has proven to be extremely effective for achieving high efficiency solar cells. However, the complete selection criteria of these solvent-additive systems still remain unclear despite its wide spread use in many low band gap polymer system. A series of solvent additives with varied polarities and vapor pressures were systematically investigated. An unfavorable solvent additive-$PC_{71}BM$ interaction in the non-polar systems induced a rather prolonged, favorable interaction between the polymer and the solvent additive. This results into a slow growth rate of polymer crystallites in the particular BHJ film and ultimately produces relatively larger polymer crystallites compared to the other BHJ films from polar additives. Such unfavorable additive-$PC_{71}BM$ interactions, occurring at the intermediate stages of the drying period, are due to their extreme polarity mismatch. $PC_{71}BM$ is initially soluble in that non-polar solvent, and the unfavorable interaction occurs when the concentration becomes much higher during the drying time, causing a large scale phase separation presumably by going through a liquid-liquid type phase separation first. The studied solvent additives were chosen based on the generally accepted criteria for selecting a solvent additive/secondary

solvent: i) it should have relatively higher solubility toward the phenyl-C71-butyric acid methyl ester ($PC_{71}BM$) and should be a bad solvent for the polymers, and ii) the boiling point must be significantly higher than that of the primary solvent.[1] However, our results indicate that mismatch between the polar components of the solubility parameters can cause large scale phase separation, even if they are soluble initially. Therefore, a more careful additive selection criteria should be defined by considering the change in the nature of interactions during solvent evaporation period. In addition, the polymer crystallite size was shown to decrease as a function of solvent evaporation time in the CF/DCB case, whereas the crystallite sizes increased as a function of solvent evaporation time for the rest of the solvent additive systems (CF/TLN, CF/pXY, CF/CB, CF/Ani). This suggests that DCB in the CF/DCB case acts as a plasticizer for the polymer component during the film solidification process by keeping the polymer network slightly swelled up, thus a slightly larger crystallite size initially, which then decreases as the DCB slowly evaporates. By tuning the properties of these solvent additives, power conversion efficiencies ranging from 0.03% to 5% are obtained.

5.1.2 Development of Slot-Die Coating Methodologies: PDPPBT/$PC_{71}BM$ Solar Cells

To date, majority of the power conversion efficiencies in the literature have been reported based on small active areas that are fabricated by spin-coating methods. While spin-coating is a quick way to check device performance and screen new materials, this method cannot be directly transferred to device fabrication in an industrial setting. Thus, for BHJ devices to realize commercial applications, active materials must be processed in

a roll-to-roll coating fashion which requires a deposition process, like blade coating. Krebs *et al*. as well as some other groups have reported efficiencies using such techniques[2–4], and in some cases, the structure formation was monitored during such coating methods.[5–7] However, the number of studies is still quite limited and requires more attention since not all active materials, which are processable by the spin-coating method generating high efficiencies, are able to create a decent film via such blade coating methods. Moreover, the drying process in such coating methods is significantly different than that of the spin-coating method. We demonstrated the device fabrication of PDPPBT/$PC_{71}BM$ system using a mini slot-die coater. The device performance was comparable with those of the spin-coated devices. However, the best device performance was obtained when only 5% DCB was used as the solvent additive, whereas 20% DCB gave the best performance in the spin-coated devices as discussed in Chapter 2. The mini-slot-die coater was also used in concert with GIWAXD measurements so as to obtain *in-situ*, real-time characterization of the morphology evolution during solution-casting process.

5.1.3 Slot-Die Processing of PTB7/$PC_{71}BM$ Solar Cells: Understanding the Role of DIO on Morphology and Device Performance

Among the recently emerging additive-assisted optimized BHJ morphologies, PTB7 was the first polymer system that gave power conversion efficiency over 7% when blended with $PC_{71}BM$[8]. The inherent immiscibility[9] between the PTB7 and the $PC_{71}BM$ necessitates the use of small amount of 1,8-diiodooctane (DIO) as the solvent additive to achieve an optimal morphology during solution casting. However, to date, there has not been any clear evidence of the mechanism as to how DIO interacts with the polymer and

fullerene components during the morphology evolution process. The slot-die methodologies developed in Chapter 3, was utilized here for real time X-ray scattering measurements. Our results showed that, the onset of neat PTB7 crystallization starts at a solute concentration of only 1.34% w/w when processed from only chlorobenzene (CB). On the other hand, the appearance of the (100) peak was significantly delayed in the cases where DIO was present (PTB7/CB/DIO and BHJ/CB/DIO). PTB7 and BHJ concentrations at this delayed (100) peak appearance were ~15% and ~31% w/w for the PTB7/CB/DIO and BHJ/CB/DIO, respectively. Furthermore, no significant development of this (100) reflection was observed up to a PTB7 (BHJ) concentration of ~55% (~75%) w/w (evacuation time of 5 min). It was evident that at least 20 min of vacuum time was necessary to observe a significant enhancement in the (100) peak areas for the DIO containing compositions in both the neat PTB7 and the BHJ films. This corresponds to a PTB7 (BHJ) concentration of ~80% (~90%) w/w after the 20 min evacuation. The results indicated a strong interaction between DIO and the polymer chain. This was further confirmed by dielectric constant measurements of PTB7 and PTB7/$PC_{71}BM$ in the solution phase with and without DIO, suggesting the presence of a significant induced dipole-induced dipole type interaction between DIO and PTB7. These results provide new insights about the role of DIO for the PTB7/$PC_{71}BM$ system which can further guide the materials design process for other emerging high efficiency polymer solar cells.

5.2 Future Work

5.2.1 Temperature Dependent Processing for Enhanced PTB7 Crystallinity

In chapter 4, DIO was effectively removed from the neat polymer films or the BHJ films by application of vacuum. This can be also performed by heating the samples at different temperatures. Neat PTB7/CB/DIO and the BHJ/CB/DIO were also slot-die coated at a substrate temperature of 70 ℃. The coating speed was similar as in Chapter 4 (10 mm/s). Preliminary results showed a significant enhancement of the polymer crystallinity both in the neat polymer film and the BHJ film upon coating the samples at an elevated temperature (**Figure 5.1**). Preliminary device results, fabricated under non-optimal conditions and at 60 ℃ coating temperature, showed poor performance (~5% PCE) as shown in **Figure 5.2**. However, the results show that with controlled temperature and further optimization, a much improved device efficiency could be achieved due to the increased PTB7 chain ordering. This will allow for temperature/time dependent study of PTB7 crystallization kinetics. However, in terms of device performance, the degree of phase separation also need to be carefully controlled so that large scale phase separation could be prevented.

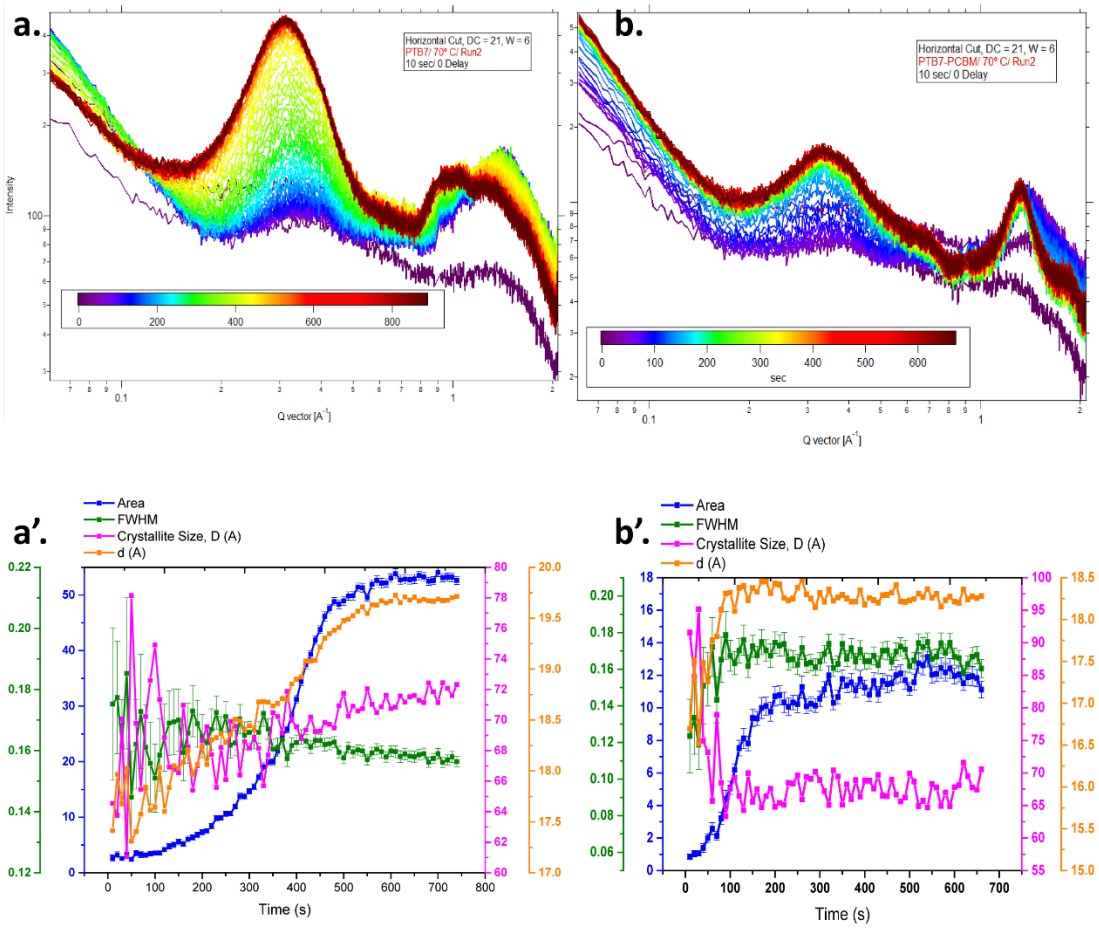

Figure 5.1 Neat PTB7 (a, a') and PTB7/PCBM blend (b, b') from CB/DIO solvent with a coating temperature of 70 °C with continued annealing of ~15 min. The top panel shows the scattering line profiles in the in-plane directions and the bottom panel shows corresponding analysis of the (100) reflection.

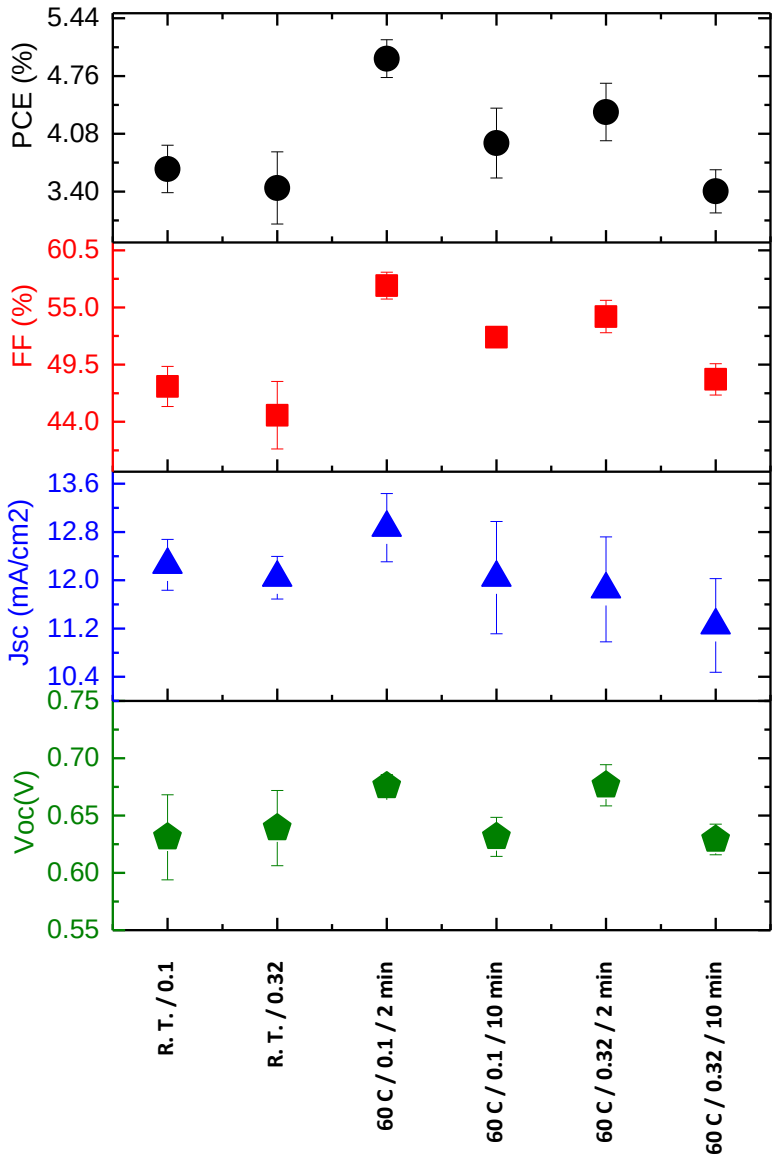

Figure 5.2 PTB7/$PC_{71}BM$ device with a coating temperature of 60 ℃ with an active area of either 0.1 or 0.32 cm^2, and with different drying/annealing period at 60 ℃ right after the coating.

5.2.2 Challenges in Large Area Fabrication of Crystalline Small Molecule Based OPV

Besides polymer based OPV, there has been a great interest in the solution processability of small molecule based OPVs. DTS(FBTTh2)2 has been reported to be one of the highest performing small molecules giving power conversion efficiencies in the range of 7-8%.[10] However, due to its extremely high crystallinity, the processing steps generally requires a very rapid spin-coating from a hot BHJ solution. In our experiments, fabrication of DTS(FBTTh2)2/$PC_{71}BM$ based devices using the mini slot-die coater at various coating temperatures yielded extremely non-uniform films with very large crystallites demonstrating that roll-to-roll coating is not feasible for this materials system without further enhancement in the materials design/processing condition to reduce the crystallinity. A small addition (10-30% w/w) of another DPP based low band gap polymer, DT-PDPP2T-TT, was found to increase the viscosity of the DTS(FBTTh2)2/$PC_{71}BM$ solution. Furthermore, addition of the DT-PDPP2T-TT polymer reduced the large scale crystallization of the small molecule, giving an efficiency of ~3% (**Figure 5.3 and 5.4**). In addition, the polymer has complementary absorption spectra relative to the DTS(FBTTh2)2 small molecule. Therefore, use of this photoactive DT-PDPP2T-TT polymer, will play both as a solid additive, and a photoactive material as in a ternary blend solar cell. The initial device performance results are promising and more experiments are required to optimize the BHJ performance. Further *in-situ* studies on this ternary system will also reveal the influence of the polymer on DTS(FBTTh2)2 crystallization. Both the DTS(FBTTh2)2 small molecule and the DT-PDPP2T-TT polymer were purchased from 1-material.

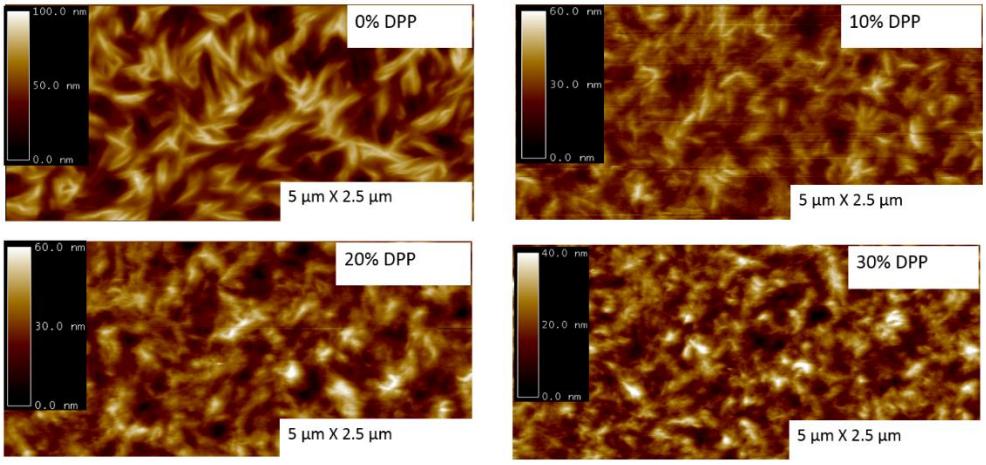

Figure 5.3 AFM height images of DTS(FBTTh2)2/PCBM blends with different ratios of the DT-PDPP2T-TT polymer.

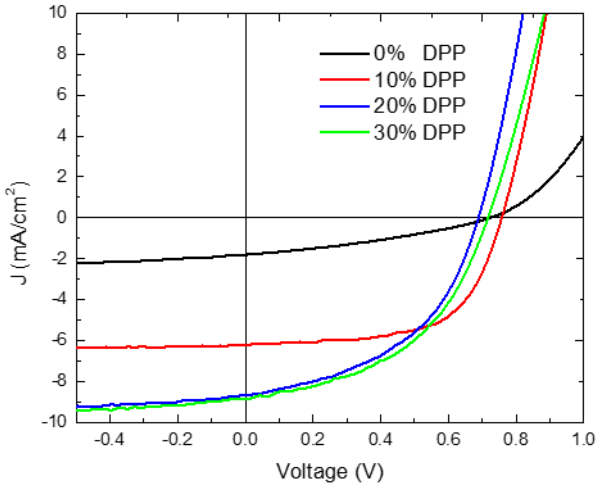

Figure 5.4 Preliminary device performance of DTS(FBTTh2)2/PCBM blends with different ratios of the DT-PDPP2T-TT polymer.

5.3 References

[1] A. Pivrikas, H. Neugebauer, N. S. Sariciftci, *Sol. Energy* **2011**, *85*, 1226.

[2] F. C. Krebs, *Sol. Energy Mater. Sol. Cells* **2009**, *93*, 394.

[3] J. W. Jung, W. H. Jo, *Adv. Funct. Mater.* **2010**, *20*, 2355.

[4] J. Lee, H. Back, J. Kong, H. Kang, S. Song, H. Suh, S.-O. Kang, K. Lee, *Energy Environ. Sci.* **2013**, *6*, 1152.

[5] B. Schmidt-Hansberg, M. Sanyal, M. F. G. Klein, M. Pfaff, N. Schnabel, S. Jaiser, A. Vorobiev, E. Müller, A. Colsmann, P. Scharfer, D. Gerthsen, U. Lemmer, E. Barrena, W. Schabel, *ACS Nano* **2011**, *5*, 8579.

[6] B. Schmidt-Hansberg, M. F. G. Klein, M. Sanyal, F. Buss, G. Q. G. de Medeiros, C. Munuera, A. Vorobiev, A. Colsmann, P. Scharfer, U. Lemmer, E. Barrena, W. Schabel, *Macromolecules* **2012**, *45*, 7948.

[7] N. Shin, L. J. Richter, A. a. Herzing, R. J. Kline, D. M. DeLongchamp, *Adv. Energy Mater.* **2013**, *3*, 938.

[8] Y. Liang, Z. Xu, J. Xia, S. T. Tsai, Y. Wu, G. Li, C. Ray, L. Yu, *Adv. Energy Mater.* **2010**, *22*, 135.

[9] B. Collins, Z. Li, J. R. Tumbleston, E. Gann, C. R. Mcneill, H. Ade, *Adv. Energy Mater.* **2013**, *3*, 65.

[10] T. S. Van Der Poll, J. a. Love, T. Q. Nguyen, G. C. Bazan, *Adv. Mater.* **2012**, *24*, 3646.

BIBLIOGRAPHY

Ade, H., & Hitchcock, A. P. (2008). NEXAFS microscopy and resonant scattering: Composition and orientation probed in real and reciprocal space. *Polymer*, *49*(3), 643–675. doi:10.1016/j.polymer.2007.10.030

Barnes, M. D., & Baghar, M. (2012). Optical probes of chain packing structure and exciton dynamics in polythiophene films, composites, and nanostructures. *Journal of Polymer Science, Part B: Polymer Physics*, *50*(15), 1121–1129. doi:10.1002/polb.23105

Barton, A. F. M. (1975). Solubility parameters. *Chemical Reviews*, *75*(6), 731–753. doi:10.1021/cr60298a003

Bijleveld, J. (2009). Poly (diketopyrrolopyrrole- terthiophene) for Ambipolar Logic and Photovoltaics. *Journal of American Chemical Society*, *131*, 16616–16617. doi:10.1002/adma.200901819.

Bijleveld, J. C., Gevaerts, V. S., Di Nuzzo, D., Turbiez, M., Mathijssen, S. C. J., De Leeuw, D. M., … Janssen, R. A. J. (2010). Efficient solar cells based on an easily accessible diketopyrrolopyrrole polymer. *Advanced Materials*, *22*(35), 242–246. doi:10.1002/adma.201001449

Blom, P. W. M., Mihailetchi, V. D., Koster, L. J. A., & Markov, D. E. (2007). Device physics of polymer:Fullerene bulk heterojunction solar cells. *Advanced Materials*, *19*(12), 1551–1566. doi:10.1002/adma.200601093

Brabec, C. J., Gowrisanker, S., Halls, J. J. M., Laird, D., Jia, S., & Williams, S. P. (2010). Polymer-fullerene bulk-heterojunction solar cells. *Advanced Materials*, *22*(34), 3839–3856. doi:10.1002/adma.200903697

Carsten, B., Szarko, J. M., Son, H. J., Wang, W., Lu, L., He, F.,Yu, L. (2011). Examining the effect of the dipole moment on charge separation in donor-acceptor polymers for organic photovoltaic applications. *Journal of the American Chemical Society*, *133*(50), 20468–20475. doi:10.1021/ja208642b

Chapin, D. M., Fuller, C. S., & Pearson, G. L. (1954). A new silicon p-n junction photocell for converting solar radiation into electrical power [3]. *Journal of Applied Physics*, *25*(5), 676–677. doi:10.1063/1.1721711

Chen, D., Nakahara, A., Wei, D., Nordlund, D., & Russell, T. P. (2011). P3HT/PCBM bulk heterojunction organic photovoltaics: Correlating efficiency and morphology. *Nano Letters*, *11*(2), 561–567. doi:10.1021/nl103482n

Chen, H., Hsiao, Y.-C., Hu, B., & Dadmun, M. (2014). Tuning the Morphology and Performance of Low Bandgap Polymer:Fullerene Heterojunctions via Solvent Annealing in Selective Solvents. *Advanced Functional Materials*, *24*, 5129–5136. doi:10.1002/adfm.201400552

Chen, H. Y., Yang, H., Yang, G., Sista, N. S., Zadoyan, R., Li, G., & Yang, Y. (2009). Fast-grown interpenetrating network in poly(3-hexylthiophene): Methanofullerenes solar cells processed with additive. *Journal of Physical Chemistry C*, *113*(18), 7946–7953. doi:10.1021/jp810798z

Chen, W., Nikiforov, M. P., & Darling, S. B. (2012a). Morphology characterization in organic and hybrid solar cells. *Energy & Environmental Science*, *5*(8), 8045. doi:10.1039/c2ee22056c

Chen, W., Nikiforov, M. P., & Darling, S. B. (2012b). Morphology characterization in organic and hybrid solar cells. *Energy & Environmental Science*, *5*(8), 8045. doi:10.1039/c2ee22056c

Chen, W., Xu, T., He, F., Wang, W., Wang, C., Strzalka, J., Darling, S. B. (2011). Hierarchical Nanomorphologies Promote Exciton Dissociation in polymère/fullerene bulk heterojunction solar cells. *Nano Letters*, *11*, 3707–3713.

Chiu, M. Y., Jeng, U. S., Su, C. H., Liang, K. S., & Wei, K. H. (2008). Simultaneous use of small- and wide-angle X-ray techniques to analyze nanometerscale phase separation in polymer heterojunction solar cells. *Advanced Materials*, *20*(13), 2573–2578. doi:10.1002/adma.200703097

Collins, B. a, Tumbleston, J. R., & Ade, H. (2011). Miscibility, Crystallinity, and Phase Development in P3HT/PCBM Solar Cells: Toward an Enlightened Understanding of Device Morphology and Stability. *J. Phys. Chem.Lett.*, *2*, 3135–3145. doi:10.1021/jz2014902

Collins, B. A., Cochran, J. E., Yan, H., Gann, E., Hub, C., Fink, R., Ade, H. (2012). Polarized X-ray scattering reveals non-crystalline orientational ordering in organic films. *Nature Materials*, *11*(6), 536–543. doi:10.1038/nmat3310

Collins, B. A., Li, Z., Tumbleston, J. R., Gann, E., Mcneill, C. R., & Ade, H. (2013). Absolute measurement of domain composition and nanoscale size distribution explains performance in PTB7:PC71bm solar cells. *Advanced Energy Materials*, *3*(1), 65–74. doi:10.1002/aenm.201200377

Darling, S. B., & You, F. (2013). The case for organic photovoltaics. *RSC Advances*, *3*, 17633–17648. doi:10.1039/c3ra42989j

Deibel, C., & Dyakonov, V. (2010). Polymer–fullerene bulk heterojunction solar cells. *Reports on Progress in Physics*, *73*(9), 096401. doi:10.1088/0034-4885/73/9/096401

DeLongchamp, D. M., Kline, R. J., & Herzing, A. (2012). Nanoscale structure measurements for polymer-fullerene photovoltaics. *Energy & Environmental Science*, *5*(3), 5980. doi:10.1039/c2ee02725a

Dennler, G., Scharber, M. C., & Brabec, C. J. (2009). Polymer-Fullerene Bulk-Heterojunction Solar Cells. *Advanced Materials*, *21*(13), 1323–1338. doi:10.1002/adma.200801283

Ferdous, S., Liu, F., Wang, D., & Russell, T. P. (2014). Solvent-polarity-induced active layer morphology control in crystalline diketopyrrolopyrrole-based low band gap polymer photovoltaics. *Advanced Energy Materials*, *4*(2), DOI: 10.1002/aenm.201300834. doi:10.1002/aenm.201300834

G. Yu, J. Gao, J. C. Hummelen, F. Wudl, A. J. H. (1995). Polymer Photovoltaic Cells: Enhanced Efficiencies via a Network of Internal Donor-Acceptor Heterojunctions. *Science*, *270*, 1789–1791.

Garcia-Belmonte, G., Guerrero, A., & Bisquert, J. (2013). Elucidating Operating Modes of Bulk-Heterojunction Solar Cells from Impedance Spectroscopy Analysis. *The Journal of Physical Chemistry Letters*, *4*(6), 877–886. doi:10.1021/jz302064z

Gehan, T. S., Bag, M., Renna, L. a, Shen, X., Algaier, D. D., Lahti, P. M., Venkataraman, D. (2014). Multiscale Active Layer Morphologies for Organic Photovoltaics Through Self-Assembly of Nanospheres. *Nano Letters*, *14*, 5238–5243. doi:10.1021/nl502209s

Graham, K. R., Wieruszewski, P. M., Stalder, R., Hartel, M. J., Mei, J., So, F., & Reynolds, J. R. (2012). Improved performance of molecular bulk-heterojunction photovoltaic cells through predictable selection of solvent additives. *Advanced Functional Materials*, *22*(22), 4801–4813. doi:10.1002/adfm.201102456

Gu, S., Neugebauer, H., & Sariciftci, N. S. (2007). Conjugated Polymer-Based Organic Solar Cells. *Chem.Rev.*, *107*, 1324–1338. doi:10.1021/cr050149z

Gu, Y., Wang, C., & Russell, T. P. (2012). Multi-length-scale morphologies in PCPDTBT/PCBM bulk-heterojunction solar cells. *Advanced Energy Materials*, *2*(6), 683–690. doi:10.1002/aenm.201100726

Guerrero, A., Montcada, N. F., Ajuria, J., Etxebarria, I., Pacios, R., Garcia-Belmonte, G., & Palomares, E. (2013). Charge carrier transport and contact selectivity limit the operation of PTB7-based organic solar cells of varying active layer thickness. *Journal of Materials Chemistry A*, *1*, 12345. doi:10.1039/c3ta12358h

Hansen, C. M. (2007). *Hansen Solubility Parameters A User's Handbook*. Boca Raton: CRC Press.

He, Z., Xiao, B., Liu, F., Wu, H., Yang, Y., Xiao, S., … Cao, Y. (2015). Single-junction polymer solar cells with high efficiency and photovoltage. *Nature Photonics*, *9*(February). doi:10.1038/nphoton.2015.6

Hedley, G. J., Ward, A. J., Alekseev, A., Howells, C. T., Martins, E. R., Serrano, L. A, Samuel, I. D. W. (2013a). Determining the optimum morphology in high-performance polymer-fullerene organic photovoltaic cells. *Nature Communications*, *4*, DOI: 10.1038/ncomms3867. doi:10.1038/ncomms3867

Heliatek News. (2013). www.heliatek.com/newscenter, p. www.heliatek.com/newscenter. Retrieved from www.heliatek.com/newscenter

Hoppe, H., Niggemann, M., Winder, C., Kraut, J., Hiesgen, R., Hinsch, A., Sariciftci, N. S. (2004). Nanoscale Morphology of Conjugated Polymer/Fullerene-Based Bulk-Heterojunction Solar Cells. *Advanced Functional Materials*, *14*(10), 1005–1011. doi:10.1002/adfm.200305026

Huang, Y., Kramer, E. J., Heeger, A. J., & Bazan, G. C. (2014). Bulk heterojunction solar cells: morphology and performance relationships. *Chemical Reviews*, *114*(14), 7006–7043. doi:10.1021/cr400353v

Hummelen, J. C., Knight, B. W., Lepeq, F., Wudl, F., Yao, J., & Wilkins, C. L. (1995). Preparation and Characterization of Fulleroid and Methanofullerene Derivatives, (20), 532–538.

Jung, J. W., & Jo, W. H. (2010). Annealing-Free High Efficiency and Large Area Polymer Solar Cells Fabricated by a Roller Painting Process. *Advanced Functional Materials*, *20*(14), 2355–2363. doi:10.1002/adfm.201000164

Kaatze, U., Gottmann, 0, Podbielski, R., Pottel, R., & Terveer, U. (1978). Dielectric Relaxation in Aqueous Solutions of Some Oxygen-Containing Linear Hydrocarbon Polymers. *The Journal of Physical Chemistry*, *82*(1), 112–120. doi:10.1016/0001-8716(75)80015-0

Kallmann, H., & Pope, M. (1959). Photovoltaic Effect in Organic Crystals. *The Journal of Chemical Physics*, *30*(2), 585–586. doi:10.1063/1.1729992

Kniepert, J., Lange, I., Heidbrink, J., Kurpiers, J., Brenner, T. J. K., Koster, L. J. A., & Neher, D. (2015). The Effect of Solvent Additive on Generation, Recombination and Extraction in PTB7:PCBM Solar Cells: A Conclusive Experimental and Numerical Simulation Study. *The Journal of Physical Chemistry C*, *119*, 8310–8320. doi:10.1021/jp512721e

Krebs, F. C. (2009a). Fabrication and processing of polymer solar cells: A review of printing and coating techniques. *Solar Energy Materials and Solar Cells*, *93*(4), 394–412. doi:10.1016/j.solmat.2008.10.004

Krebs, F. C. (2009b). Fabrication and processing of polymer solar cells: A review of printing and coating techniques. *Solar Energy Materials and Solar Cells*, *93*(4), 394–412. doi:10.1016/j.solmat.2008.10.004

Krebs, F. C., Fyenbo, J., Tanenbaum, D. M., Gevorgyan, S. a., Andriessen, R., van Remoortere, B., … Jørgensen, M. (2011). The OE-A OPV demonstrator anno domini 2011. *Energy & Environmental Science*, *4*(10), 4116. doi:10.1039/c1ee01891d

Krebs, F. C., Tromholt, T., & Jorgensen, M. (2010). Upscaling of polymer solar cell fabrication using full roll-to-roll processing. *Nanoscale*, *2*(6), 873–886. doi:10.1039/b9nr00430k

Lee, J., Back, H., Kong, J., Kang, H., Song, S., Suh, H., … Lee, K. (2013). Seamless polymer solar cell module architecture built upon self-aligned alternating interfacial layers. *Energy & Environmental Science*, *6*(4), 1152. doi:10.1039/c3ee24454g

Lee, J. K., Ma, W. L., Brabec, C. J., Yuen, J., Moon, J. S., Kim, J. Y., Heeger, A. J. (2008). Processing additives for improved efficiency from bulk heterojunction solar cells. *Journal of the American Chemical Society*, *130*(11), 3619–23. doi:10.1021/ja710079w

Li, L. H., Kontsevoi, O. Y., Rhim, S. H., & Freeman, A. J. (2013). Structural, electronic, and linear optical properties of organic photovoltaic PBTTT-C14 crystal. *Journal of Chemical Physics*, *138*(16), 164503. doi:10.1063/1.4802033

Li, L.-H., Kontsevoi, O. Y., & Freeman, A. J. (2014). Electronic and optical excitations of the PTB7 crystal: First-principles GW-BSE calculations. *Physical Review B*, *90*(19), 1–8. doi:10.1103/PhysRevB.90.195203

Li, W., Roelofs, W. S. C., Wienk, M. M., & Janssen, R. a J. (2012). Enhancing the photocurrent in diketopyrrolopyrrole-based polymer solar cells via energy level control. *Journal of the American Chemical Society*, *134*(33), 13787–95. doi:10.1021/ja305358z

Liang, Y., Xu, Z., Xia, J., Tsai, S. T., Wu, Y., Li, G., … Yu, L. (2010). For the bright future-bulk heterojunction polymer solar cells with power conversion efficiency of 7.4%. *Advanced Energy Materials*, *22*(20), 135–138. doi:10.1002/adma.200903528

Liao, H.-C., Tsao, C.-S., Lin, T.-H., Chuang, C.-M., Chen, C.-Y., Jeng, U.-S., … Su, W.-F. (2011). Quantitative nanoorganized structural evolution for a high efficiency bulk heterojunction polymer solar cell. *Journal of the American Chemical Society*, *133*(33), 13064–13073. doi:10.1021/ja202977r

Liu, F., Ferdous, S., Schaible, E., Hexamer, A., Church, M., Ding, X., … Russell, T. (2014). Fast Printing and In-Situ Morphology Observation of Organic Photovoltaics using Slot-Die Coating. *Advanced Materials*, *27*, 886–891. doi:10.1002/adma.201404040

Liu, F., Gu, Y., Jung, J. W., Jo, W. H., & Russell, T. P. (2012). On the morphology of polymer-based photovoltaics. *Journal of Polymer Science, Part B: Polymer Physics*, *50*(15), 1018–1044. doi:10.1002/polb.23063

Liu, F., Gu, Y., Shen, X., Ferdous, S., Wang, H. W., & Russell, T. P. (2013). Characterization of the morphology of solution-processed bulk heterojunction organic photovoltaics. *Progress in Polymer Science*, *38*(12), 1990–2052. doi:10.1016/j.progpolymsci.2013.07.010

Liu, F., Gu, Y., Wang, C., Zhao, W., Chen, D., Briseno, A. L., & Russell, T. P. (2012). Efficient polymer solar cells based on a low bandgap semi-crystalline DPP polymer-PCBM blends. *Advanced Materials (Deerfield Beach, Fla.)*, *24*(29), 3947–51. doi:10.1002/adma.201200902

Liu, F., Zhao, W., Tumbleston, J. R., Wang, C., Gu, Y., Wang, D., … Russell, T. P. (2014). Understanding the morphology of PTB7:PCBM blends in organic photovoltaics. *Advanced Energy Materials*, *4*, 1301377 doi: 10.1002/aenm.201301377. doi:10.1002/aenm.201301377

Liu, J., Shi, Y., & Yang, Y. (2001). Solvation-induced morphology effects on the performance of polymer-based photovoltaic devices. *Advanced Functional Materials*, *11*(6), 1–5.

Liu, Y., Zhao, J., Li, Z., Mu, C., Ma, W., Hu, H., Yan, H. (2014). Aggregation and morphology control enables multiple cases of high-efficiency polymer solar cells. *Nature Communications*, *5*, 5293. doi:10.1038/ncomms6293

Lou, S. J., Szarko, J. M., Xu, T., Yu, L., Marks, T. J., & Chen, L. X. (2011). Effects of Additives on the Morphology of Solution Phase Aggregates.pdf. *Journal of American Chemical Society*, *133*, 20661–20663.

MacHui, F., Langner, S., Zhu, X., Abbott, S., & Brabec, C. J. (2012). Determination of the P3HT:PCBM solubility parameters via a binary solvent gradient method: Impact of solubility on the photovoltaic performance. *Solar Energy Materials and Solar Cells*, *100*, 138–146. doi:10.1016/j.solmat.2012.01.005

Maryott, A., & Smith, E. (1951). *Table of Dielectric Constants of Pure Liquids*.

Pearson, A. J., Wang, T., & Lidzey, D. G. (2013). The role of dynamic measurements in correlating structure with optoelectronic properties in polymer : fullerene bulk-heterojunction solar cells. *Reports on Progress in Physics. Physical Society (Great Britain)*, *76*(2), 022501. doi:10.1088/0034-4885/76/2/022501

Peet, J., Kim, J. Y., Coates, N. E., Ma, W. L., Moses, D., Heeger, a J., & Bazan, G. C. (2007). Efficiency enhancement in low-bandgap polymer solar cells by processing with alkane dithiols. *Nature Materials*, *6*(7), 497–500. doi:10.1038/nmat1928

Perrier, G., De Bettignies, R., Berson, S., Lemaître, N., & Guillerez, S. (2012). Impedance spectrometry of optimized standard and inverted P3HT-PCBM organic solar cells. *Solar Energy Materials and Solar Cells*, *101*, 210–216. doi:10.1016/j.solmat.2012.01.013

Pivrikas, A., Neugebauer, H., & Sariciftci, N. S. (2011). Influence of processing additives to nano-morphology and efficiency of bulk-heterojunction solar cells: A comparative review. *Solar Energy*, *85*(6), 1226–1237. doi:10.1016/j.solener.2010.10.012

Qi, B., & Wang, J. (2013). Fill factor in organic solar cells. *Physical Chemistry Chemical Physics : PCCP*, *15*(23), 8972–82. doi:10.1039/c3cp51383a

Reichardt, C. (2003). *Solvents and solvent effects in organic chemistry*. Weinheim: WILEY-VCH Verlag GmbH & Co. KGaA. doi:10.1002/3527601791

Rivnay, J., Mannsfeld, S. C. B., Miller, C. E., Salleo, A., & Toney, M. F. (2012, October). Quantitative determination of organic semiconductor microstructure from the molecular to device scale. *Chemical Reviews*. doi:10.1021/cr3001109

Rogers, J. T., Schmidt, K., Toney, M. F., Bazan, G. C., & Kramer, E. J. (2012). Time-resolved structural evolution of additive-processed bulk heterojunction solar cells. *J Am Chem Soc*, *134*(6), 2884–2887. doi:10.1021/ja2104747

Salim, T., Wong, L. H., Brauer, B., Kukreja, R., Foo, Y. L., Bao, Z., & Lam, eng M. (2011). Solvent additives and their effects on blend morphologies of bulk heterojunctions. *Journal of Materials Chemistry*, *21*, 242–250. doi:10.1039/c0jm01976c

Sanyal, M., Schmidt-Hansberg, B., Klein, M. F. G., Colsmann, A., Munuera, C., Vorobiev, A., … Barrena, E. (2011). In situ X-ray study of drying-temperature influence on the structural evolution of bulk-heterojunction polymer-fullerene solar cells processed by doctor-blading. *Advanced Energy Materials*, *1*(3), 363–367. doi:10.1002/aenm.201100007

Sanyal, M., Schmidt-Hansberg, B., Klein, M. F. G., Munuera, C., Vorobiev, A., Colsmann, A., … Barrena, E. (2011). Effect of photovoltaic polymer/fullerene blend composition ratio on microstructure evolution during film solidification investigated in real time by X-ray diffraction. *Macromolecules*, *44*(10), 3795–3800. doi:10.1021/ma2000338

Sariciftci, N. S., Braun, D., Zhang, C., Srdanov, V. I., Heeger, a. J., Stucky, G., & Wudl, F. (1993). Semiconducting polymer-buckminsterfullerene heterojunctions: Diodes, photodiodes, and photovoltaic cells. *Applied Physics Letters*, *62*(6), 585. doi:10.1063/1.108863

Sariciftci, N. S., Smilowitz, L., Heeger, a J., & Wudl, F. (1992). Photoinduced electron transfer from a conducting polymer to buckminsterfullerene. *Science (New York, N.Y.)*, *258*(5087), 1474–6. doi:10.1126/science.258.5087.1474

Sarode, A. V., & Kumbharkhane, A. C. (2012). Dielectric relaxation and thermodynamic properties of polyvinylpyrrolidone using time domain reflectometry. *Polymer International*, *61*(4), 609–615. doi:10.1002/pi.3217

Schmidt-Hansberg, B., Klein, M. F. G., Sanyal, M., Buss, F., de Medeiros, G. Q. G., Munuera, C., … Schabel, W. (2012). Structure Formation in Low-Bandgap Polymer:Fullerene Solar Cell Blends in the Course of Solvent Evaporation. *Macromolecules*, *45*(19), 7948–7955. doi:10.1021/ma300945k

Schmidt-Hansberg, B., Sanyal, M., Klein, M. F. G., Pfaff, M., Schnabel, N., Jaiser, S., … Schabel, W. (2011). Moving through the phase diagram: morphology formation in solution cast polymer-fullerene blend films for organic solar cells. *ACS Nano*, *5*(11), 8579–90. doi:10.1021/nn2036279

Sengwa, R. J., & Sankhla, S. (2007). Dielectric Dispersion Study of Poly(vinyl Pyrrolidone)-Polar Solvent Solutions in the Frequency Range 20 Hz-1 MHz. *Journal of Macromolecular Science, Part B*, *46*(4), 717–747. doi:10.1080/00222340701388938

Shaheen, S. E., Brabec, C. J., Sariciftci, N. S., Padinger, F., Fromherz, T., & Hummelen, J. C. (2001). 2.5% Efficient Organic Plastic Solar Cells. *Applied Physics Letters*, *78*(6), 841–843. doi:10.1063/1.1345834

Shin, N., Richter, L. J., Herzing, A. a., Kline, R. J., & DeLongchamp, D. M. (2013). Effect of processing additives on the solidification of blade-coated polymer/fullerene blend films via in-situ structure measurements. *Advanced Energy Materials*, *3*(7), 938–948. doi:10.1002/aenm.201201027

Søndergaard, R., Hösel, M., Angmo, D., Larsen-Olsen, T. T., & Krebs, F. C. (2012). Roll-to-roll fabrication of polymer solar cells. *Materials Today*, *15*(1-2), 36–49. doi:10.1016/S1369-7021(12)70019-6

Spano, F. C., & Silva, C. (2014). H- and J-aggregate behavior in polymeric semiconductors. *Annual Review of Physical Chemistry*, *65*, 477–500. doi:10.1146/annurev-physchem-040513-103639

Swaraj, S., Wang, C., Yan, H., Watts, B., Lüning, J., McNeill, C. R., & Ade, H. (2010). Nanomorphology of bulk heterojunction photovoltaic thin films probed with resonant soft X-ray scattering. *Nano Letters*, *10*(8), 2863–2869. doi:10.1021/nl1009266

Thompson, B. C., & Fréchet, J. M. J. (2008). Polymer-fullerene composite solar cells. *Angewandte Chemie - International Edition*, *47*(1), 58–77. doi:10.1002/anie.200702506

Treat, N. D., & Chabinyc, M. L. (2014). Phase separation in bulk heterojunctions of semiconducting polymers and fullerenes for photovoltaics. *Annual Review of Physical Chemistry*, *65*, 59–81. doi:10.1146/annurev-physchem-040513-103712

Tsumuraya, T., Song, J.-H., & Freeman, A. (2012). Linear optical properties and electronic structures of poly(3-hexylthiophene) and poly(3-hexylselenophene) crystals from first principles. *Physical Review B*, *86*(7), 075114. doi:10.1103/PhysRevB.86.075114

Van Der Poll, T. S., Love, J. a., Nguyen, T. Q., & Bazan, G. C. (2012). Non-basic high-performance molecules for solution-processed organic solar cells. *Advanced Materials*, *24*(27), 3646–3649. doi:10.1002/adma.201201127

Walker, B., Tamayo, A., Duong, D. T., Dang, X. D., Kim, C., Granstrom, J., & Nguyen, T. Q. (2011). A systematic approach to solvent selection based on cohesive energy densities in a molecular bulk heterojunction system. *Advanced Energy Materials*, *1*(2), 221–229. doi:10.1002/aenm.201000054

Wang, C., Lee, D. H., Hexemer, a, Kim, M. I., Zhao, W., Hasegawa, H., Russell, T. P. (2011). Defining the Nanostructured Morphology of Triblock Copolymers Using Resonant Soft X-ray Scattering. *Nano Letters*, *11*(9), 3906–3911. doi:Doi 10.1021/Nl2020526

Wang, D., Liu, F., Yagihashi, N., Nakaya, M., Ferdous, S., Liang, X., Russell, T. P. (2014). New Insights into Morphology of High Performance BHJ Photovoltaics Revealed by High Resolution AFM. *Nano Letters*, *14*(10), 5727–5732. doi:10.1021/nl5025326

Wang, T., Dunbar, A. D. F., Staniec, P. a., Pearson, A. J., Hopkinson, P. E., Macdonald, J. E., Lidzey, D. G. (2010). The development of nanoscale morphology in polymer: fullerene photovoltaic blends during solvent casting, *6*, 4128–4134. doi:10.1039/c0sm00343c

Wienk, M. M., Turbiez, M., Gilot, J., & Janssen, R. A. J. (2008). Narrow-Bandgap Diketo-Pyrrolo-Pyrrole Polymer Solar Cells : The Effect of Processing on the Performance. *Advanced Materials*, *20*, 2556–2560. doi:10.1002/adma.200800456

Xu, L., Lee, Y.-J., & Hsu, J. W. P. (2014). Charge collection in bulk heterojunction organic photovoltaic devices: An impedance spectroscopy study. *Applied Physics Letters*, *105*, 123904–1.

Yang, B., Yuan, Y., & Huang, J. (2014). Reduced bimolecular charge recombination loss in thermally annealed bilayer heterojunction photovoltaic devices with large external quantum efficiency and fill factor. *Journal of Physical Chemistry C*, *118*(10), 5196–5202. doi:10.1021/jp500547j

Yao, Y., Hou, J., Xu, Z., Li, G., & Yang, Y. (2008). Effects of Solvent Mixtures on the Nanoscale Phase Separation in Polymer Solar Cells. *Advanced Functional Materials*, *18*(12), 1783–1789. doi:10.1002/adfm.200701459

You, J., Dou, L., Yoshimura, K., Kato, T., Ohya, K., Moriarty, T., Yang, Y. (2013). A polymer tandem solar cell with 10.6% power conversion efficiency. *Nature Communications*, *4*, 1446. doi:10.1038/ncomms2411

Yu, G., Gao, J., Hummelen, J. C., Wudl, F., & Heeger, A. J. (1995). Polymer Photovoltaic Cells: Enhanced Efficiencies via a Network of Internal Donor-Acceptor Heterojunctions. *Science*, *270*, 1789–1791. doi:10.1126/science.270.5243.1789

Zuo, L.-J., Hu, X.-L., Ye, T., Andersen, T. R., Li, H.-Y., Shi, M.-M., Chen, H.-Z. (2012). Effect of Solvent-Assisted Nanoscaled Organo-Gels on Morphology and Performance of Organic Solar Cells. *The Journal of Physical Chemistry C*, *116*(32), 16893–16900. doi:10.1021/jp3049444